VNIVERSITAT DE VALÈNCIA

DOCTORAT EN FÍSICA

Departament de Física Atòmica, Molecular i Nuclear
Institut de Física Corpuscular (CSIC-UV)

Searches for cosmic neutrino sources with ANTARES, KM3NeT and IceCube and time calibration of ANTARES

Giulia Illuminati

Supervisors Dr. Juan de Dios Zornoza Gómez
and Dr. Alexis Coleiro

Valencia, January, 2020

Giulia Illuminati
Searches for cosmic neutrino sources with ANTARES, KM3NeT and IceCube and time calibration of ANTARES
January, 2020
Supervisors: Dr. Juan de Dios Zornoza Gómez and Dr. Alexis Coleiro

Universitat de València
Física Experimental d'Astropartícules (GIUV2013-157)
Institut de Física Corpuscular (CSIC-UV)
Departament de Física Atòmica, Molecular i Nuclear

Dr. JUAN DE DIOS ZORNOZA GÓMEZ, profesor contratado doctor al Departamento de Física Atómica, Molecular y Nuclear de la Facultad de Física de la Universidad de Valencia, y Dr. ALEXIS COLEIRO, profesor titular al Departamento de Física de la Universidad de Paris,

CERTIFICAN,

Que la presente memoria, Searches for cosmic neutrino sources with ANTARES, KM3NeT and IceCube and time calibration of ANTARES, ha sido realizada bajo su dirección en el Instituto de Física Corpuscular (Centro Mixto Universidad de Valencia - CSIC) por Giulia Illuminati y constituye su Tesis Doctoral en el Departamento de Física Atómica Molecular y Nuclear de la Universidad de Valencia para optar al grado de Doctor en Física.

Y para que conste, en cumplimiento de la legislación vigente, firman el presente certificado en Paterna, el 13 de enero de 2020.

Dr. Juan de Dios Zornoza Gómez

Dr. Alexis Coleiro

Ai miei genitori

Contents

Preface

More than 100 years after the discovery of cosmic rays, their origin and acceleration mechanisms are yet an unresolved puzzle that neutrinos have the chance to solve. Neutrinos are expected to be produced alongside γ-rays in the interaction of the accelerated high-energy cosmic rays with ambient matter or photon fields in the vicinity of their acceleration sites. However, while γ-rays can also be produced in leptonic mechanisms, neutrinos are the smoking gun signature for hadronic processes and therefore are a unique tracer of cosmic-ray acceleration. Being neutral and weakly-interacting, neutrinos can travel long distances without being deflected by cosmic magnetic fields and can escape dense environments. Since neutrinos allow for precise pointing to their production sites, their detection will make it possible to unequivocally identify the sources of cosmic rays.

While being the perfect cosmic messengers, neutrinos are extremely difficult to detect, requiring the construction of huge telescopes in challenging environments. An established approach to perform high-energy neutrino astronomy is the observation of the Cherenkov radiation induced by the passage in a transparent medium of the charged leptons produced in neutrino interactions. Three-dimentional arrays of photomultiplier tubes deployed deep underwater or in under-ice sites are used to detect the Cherenkov light and reconstruct the parent neutrino energy and direction. Operating high-energy neutrino telescopes like ANTARES, a $\sim$0.01 km^3 volume detector in the Mediterranean Sea, and IceCube, a cubic-kilometer-sized detector located at the South Pole below the surface of the Antarctic ice, and the future largest network of neutrino telescopes, KM3NeT, currently being deployed in the Mediterranean Sea, rely on this detection principle.

IceCube recently reported the first observation of a diffuse flux of high-energy neutrinos of extraterrestrial origin together with the first compelling association of astrophysical neutrinos with an individual cosmic source. These recent discoveries reveal the potential of high-energy neutrino astronomy to explore the high-energy Universe and strongly encourage additional studies.

The search for individual sources of cosmic neutrinos is the main objective of the work realized during this Thesis. Three different analyses of the data recorded by high-energy neutrino telescopes have been performed. The first analysis is an update of the ANTARES standard point-like source search using 11 years of ANTARES data. The second analysis is a search for point-like and extended sources of astrophysical neutrinos in the Southern Sky using the combined data of ANTARES and IceCube. In the third analysis, a search for time and space correlations between ANTARES data and IceCube high-energy astrophysical neutrino candidates is performed. While no significant neutrino source was detected, these analyses put strong constraints on a potential high-energy neutrino emission, especially in the Southern Sky. Moreover, an additional result of this Thesis is the first estimation of the sensitivity to point-like sources of the first construction phase of the future detector dedicated to high-energy astronomy, KM3NeT/ARCA. The method employed to search for individual sources of cosmic neutrinos is described in Chapter 6, while the results of the four analyses are presented in Chapter 7.

A further goal of the work performed within this Thesis is the time calibration of the ANTARES detector performed for two years (2017 and 2018) of the data taking period. The time calibration procedure and the results are described in Chapter 5.

In order to contextualise the results obtained in this Thesis, the first four Chapters give an overview of the field. In particular, Chapter 1 describes the connection between high-energy cosmic rays and neutrinos, lists potential high-energy neutrino sources, and discusses the current status of high-energy neutrino astronomy. The detection principle employed by high-energy neutrino telescopes and a detailed description of the ANTARES, IceCube and KM3NeT detectors are presented in Chapters 2 and 3, respectively, while Chapter 4 describes the official event simulation chains and the event reconstruction algorithms employed in ANTARES and KM3NeT.

1 Neutrino astronomy

Neutrinos, being weakly-interacting and neutral particles, are ideal cosmic messengers: they can escape dense environments and can travel long distances without being deflected by cosmic magnetic fields, allowing precise pointing to their production sites. Because of these unique features, GeV-PeV neutrinos may provide the missing clues to unveil the origin of cosmic rays, which remains largely unresolved more than a hundred years after their discovery. Since identifying the origin of cosmic rays is one of the main motivation for neutrino astronomy, they are discussed first (Section 1.1). The production mechanism of high-energy astrophysical neutrinos is described in Section 1.2, while the possible sources of cosmic rays, which are also believed to produce high-energy neutrinos, are briefly presented in Section 1.3. Finally, Section 1.4 reports on the present status of high-energy neutrino astronomy.

1.1 Cosmic Rays

The cosmic radiation continuously striking the top of the terrestrial atmosphere is mainly made of protons (∼79%) and helium nuclei (∼15%), while the rest are heavier nuclei and electrons [1, 2]. Cosmic rays (CRs) can be detected directly by experiments on board satellites and balloons and indirectly by observing the extensive air showers they cause in the Earth's atmosphere. Figure 1.1 shows the measured *all-particle* energy spectrum of CRs. The spectrum spans over many

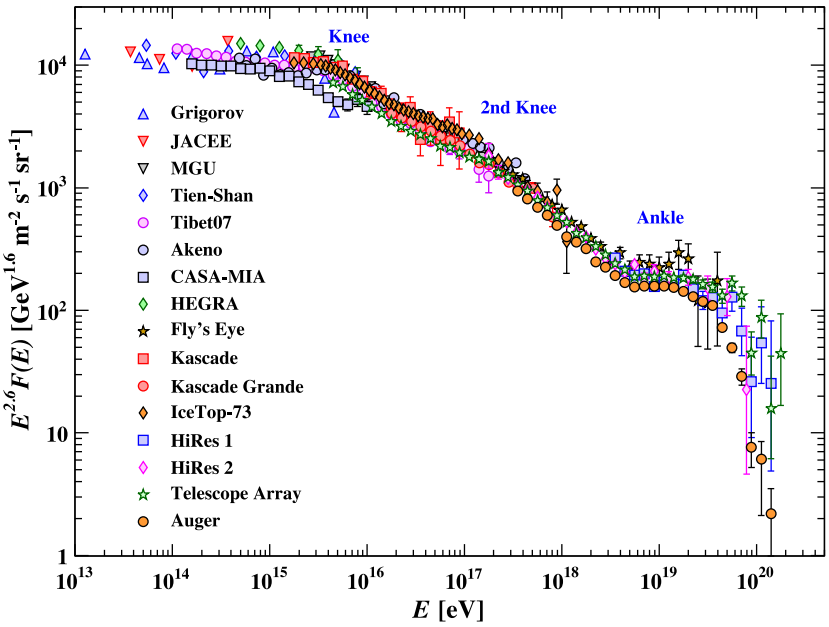

Figure 1.1: All-particle energy spectrum of cosmic rays. Figure taken from [2].

orders of magnitude in flux and in energy, up to above 10^{20} eV, and follows a power-law of the form:

$$F(E) \propto E^{-\gamma}, \tag{1.1}$$

where γ is the spectral index, showing a non-thermal origin. Three main changes in the spectral index are observed: the so-called *knee*, *second knee* and *ankle*. At the knee ($E \sim 3 \times 10^{15}$ eV), the spectral index changes from ∼2.7 to ∼3.1. A further steepening is observed at the second knee ($E \sim 4 \times 10^{17}$ eV) with γ increasing to a value of ∼3.3, while at the ankle energy ($E \sim 10^{19}$ eV) the energy spectrum flattens again to a value of γ∼2.7.

CRs up to the knee are thought to be of Galactic origin, with the supernova remnants being the prime candidates as CRs accelerators [3]. The value of the spectral index in this energy range (γ∼2.7) can be explained as the result of the combined effect of the acceleration mechanism at the source and of the propagation in the Galaxy. The most widely accepted mechanism responsible for the acceleration of charged particles is the first order Fermi mechanism [4, 5].

In this scenario, the particle acceleration is explained by iterative scattering processes of the charged particles in astrophysical shock-waves. The particles are confined to the shock due to in-homogeneities in the magnetic field, and gain energy with each passage through the shock front. The resulting particle energy spectrum at the source follows a power-law close to E^{-2}. The subsequent softening of the energy spectrum to the observed $F(E) \propto E^{-2.7}$ at Earth is a consequence of the energy-dependent CR diffusion out of the Galaxy, as explained by the so-called *leaky box model* [6]. In the leaky box model, the path of charged particles in the Galaxy is bent by the Galactic magnetic field ($B \sim 3\mu$G) and forced to follow a helical trajectory characterised by a Larmor radius $R_L \simeq \frac{E}{eZB}$, where E is the particle energy and eZ is the particle charge. For a given charge, particles with higher energies have a larger probability to escape, leading to an energy-dependent diffusion probability. The energy dependence of this probability, obtained from experimental measurements of the abundance ratio between secondary and primary cosmic rays, follows a power-law of the type $E^{-0.6}$ [7, 8], which, when convoluted with the expectations from the Fermi acceleration mechanism, leads to the spectral index measured at Earth.

The origin of the steepening of the CRs spectrum at the knee and at the second knee is still an open question and different models have been proposed to explain these features [9, 10, 11, 12]. The most popular explanations include a finite maximum energy achievable during the acceleration process in different Galactic sources and leakage from the Galaxy. In both cases, different cut-off energies are expected for different elements. In these scenarios, the knee is expected to be caused by the cut-off of protons, with all other elements following subsequently up to the second knee which may be the result of termination in the acceleration of iron nuclei in Galactic sources.

The flattening of the spectrum in the ankle region is generally associated with the transition from a Galactic to an extragalactic origin of the CRs [7, 13]. Indeed, the Larmor radius of a proton with energy above the ankle, subject to the Galactic magnetic field, exceeds the thickness of the Galaxy disk (300 pc), implying that CRs above the ankle cannot be confined within the Galaxy. The argument of the Larmor radius can be also used to derive a constraint on the maximum energy that a particle of a given charge can reach within a certain accelerator. Indeed, independently of the acceleration mechanism, the acceleration stops once the Larmor radius exceeds the accelerator size, and the cosmic ray escapes. The maximum energy that a charged particle can achieve in an accelerator

with magnetic field B and size R was first derived by Hillas [14] and can be expressed as

$$E_{\max} \simeq 10^{18}\text{eV}\ \beta\, Z \left(\frac{B}{\mu\text{G}}\right)\left(\frac{R}{\text{kpc}}\right)\,, \tag{1.2}$$

with β being the velocity of the shock wave. Figure 1.2 shows the properties of potential CRs accelerators in terms of size and magnetic field strength. CRs with the highest observed energies of up to 10^{20} eV are likely to originate from extragalactic objects.

While the Larmor argument constrains the origin of CRs above the ankle to be extragalactic, a theoretical upper limit on the maximal distance of the sources responsible for the CRs with energies above 5×10^{19} eV is set by the Greisen-Zatsepin-Kuzmin cutoff (GZK) [15, 16]. Indeed, above that energy, cosmic-ray protons begin to interact with cosmic-microwave-background (CMB) photons to produce pions via the Δ resonance:

$$p + \gamma_{\text{CMB}} \rightarrow \Delta^+ \rightarrow p + \pi^0 \tag{1.3}$$

$$\rightarrow n + \pi^+\,. \tag{1.4}$$

Due to the GZK cutoff, protons with energy above 5×10^{19} eV cannot travel distances further than a few tens of Mpc. This suppresses the observable flux of CRs above such energies due to the lack of sources able to accelerate above the GZK cutoff inside our local super-cluster of galaxies. The predicted cut-off energy coincides well with the rapid steepening observed in the spectrum (see Figure 1.1).

1.2 Astrophysical neutrino production

Any astrophysical object able to provide compressive shock fronts and magnetic confinement has the potential to accelerate charged particles by means of the Fermi mechanism. Assuming that a fraction of the CRs interacts with the ambient matter or photon fields at the acceleration sites, also γ-rays and high-energy neutrinos are expected to be emitted. In this scenario, known as *hadronic* scenario, the production of γ-rays and neutrinos is explained via the decay of the pions

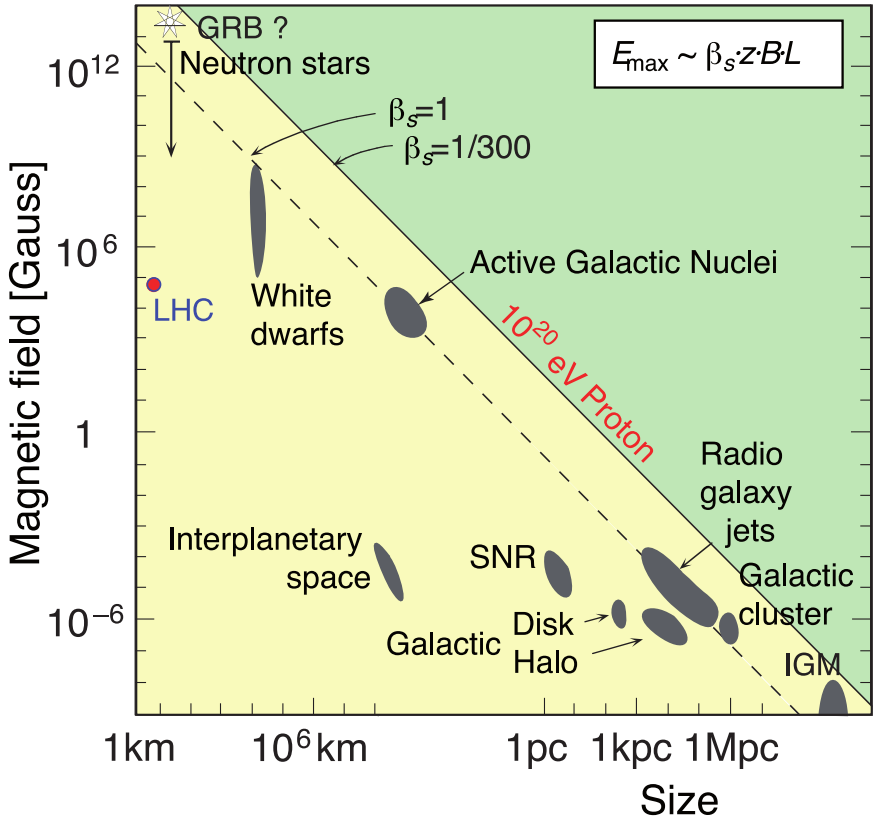

Figure 1.2: Hillas plot showing the relation between the magnetic field strength and the size for candidate accelerators of CRs. Figure taken from [12].

produced in the interaction of the accelerated protons either with the photons via the Delta resonance:

$$p + \gamma \rightarrow \Delta^{+} \rightarrow p + \pi^{0} \tag{1.5}$$

$$\rightarrow n + \pi^{+}\,, \tag{1.6}$$

or with matter:

$$p + p \rightarrow p + p + \pi^0 \tag{1.7}$$
$$\rightarrow p + n + \pi^+ \,, \tag{1.8}$$

$$p + n \rightarrow p + n + \pi^0 \tag{1.9}$$
$$\rightarrow p + p + \pi^+ \,. \tag{1.10}$$

While the neutral pions decay into γ-rays:

$$\pi^0 \rightarrow \gamma + \gamma \,, \tag{1.11}$$

neutrinos are produced in various steps of the decay chain of the charged pions:

$$\begin{aligned} \pi^+ &\rightarrow \nu_\mu + \mu^+ \\ &\qquad \hookrightarrow \mu^+ \rightarrow \bar{\nu}_\mu + \nu_e + e^+ \,, \\ \pi^- &\rightarrow \bar{\nu}_\mu + \mu^- \\ &\qquad \hookrightarrow \mu^- \rightarrow \nu_\mu + \bar{\nu}_e + e^- \,. \end{aligned} \tag{1.12}$$

The resulting expected ratio of the three neutrino flavours (electron, muon, and tau) at the source is thus:

$$\nu_e : \nu_\mu : \nu_\tau = 1 : 2 : 0 \,, \tag{1.13}$$

which translates into a uniform flavour ratio at Earth after oscillations over a long baseline [17]: $\nu_e : \nu_\mu : \nu_\tau = 1 : 1 : 1$. In this framework, the produced neutrinos are expected to follow almost the same energy spectrum of the parent CRs at the source ($\propto E^{-2}$) [1, 18, 19].

Therefore, in the hadronic scenario, candidate sources for the acceleration of CRs are also sources of γ-rays and neutrinos. However, γ-rays can also be the result of *leptonic* processes at the source such as synchrotron emission and inverse-Compton effect [7]. The detection of neutrinos would be an unambiguous signature for CR acceleration sites and would provide insight into the amount of hadronic interactions within a source.

1.3 Neutrino source candidates

The Hillas diagram presented in Figure 1.2 shows a large number of potential CR accelerators. While there are many proposed neutrino source candidates [20, 21, 22, 23, 24, 25], the following section focuses on four particularly promising ones. The objects considered are shell-type supernova remnants (SNRs) and the Galactic Centre (GC) as Galactic sources, and Gamma-Ray Bursts (GRBs) and Active Galactic Nuclei (AGNs) as extragalactic objects. Other possible Galactic sources include pulsar wind nebulae and microquasars, while extragalactic sources include also starburst galaxies and galaxy clusters.

Shell-type supernova remnants. Supernova remnants are the leftover from a supernova explosion. The shell-type remnants are characterised by an emission that originates from an expanding shell of ejected material that interacts with the interstellar medium. The emitted material moves in shock fronts at typical velocities of 10^5 m/s, in a process that can continue up to 10^4-10^5 years before the energy release becomes negligible. A SNR of particular interest is RX J1713.7-3946. Being the brightest SNR in the TeV γ-ray sky, it has often been indicated as a promising candidate for neutrino emission [26, 19, 27].

The Galactic Centre. The centre of the Galaxy is an extremely interesting region for high-energy neutrino astronomy. Not only the GC is characterised by a high density of astrophysical objects including a super-massive black hole (SMBH), Sagittarius A*, but it is also the only known Galactic accelerator of PeV protons [28].

Gamma-Ray bursts. GRBs are the most luminous objects in the Universe, releasing $\sim 10^{51} - 10^{53}$ erg in a few seconds [29]. They are characterised by an extremely bright γ-ray emission followed by an afterglow in X, UV, optical and radio. Recently, a very-high-energy emission (> 100 GeV) was reported from three γ-ray bursts, namely GRB 190114C, detected by MAGIC during the prompt phase [30], and GRB 180720B and GRB 190829A, detected by HESS in the afterglow phase [31, 32]. GRBs are classified according to their duration into long-duration GRBs ($\Delta t > 2$ s) and short-duration GRBs [7]. Long ones are believed to emerge from some of the core-collapse supernovae (CCSN). This is confirmed by observations showing a GRB and then an optical spectrum compatible with a CCSN [33]. Short GRBs are thought to result from the merging of two compact objects. This hypothesis has been recently supported by the association of the short γ-ray burst GRB 170817A and the gravitational wave

event GW170817, originated from a binary neutron star inspiral [34]. In both cases (long and short GRBs), the production of the high-energy emission in GRBs might be explained with the *fireball model*: the prompt γ-rays are originated by expanding shocks in the plasma expelled from a relativistic jet, while the afterglow emission, at lower frequencies, is caused by the time-delayed interaction of the jet with the surrounding medium. While neutrino telescopes have not detected GRB counterpart so far [35, 36, 37, 38, 39], protons could also be shock-accelerated, leading to the production of neutrinos. Possible mechanisms for the production of neutrinos in GRBs include the internal shock model, the dissipative photosphere model, and the Internal Collision-induced MAgnetic Reconnection and Turbulence (ICMART) model [40, 41].

Active galactic nuclei. AGNs are cores of galaxies hosting a SMBH of $\sim 10^6$-10^{10} solar masses with an accretion disk rotating around it. Two relativistic jets, which can extend over several Mpc, may point out from the core perpendicularly to the accretion disk. Due to shock fronts around and within the accretion disk and the jets, particles are accelerated up to the highest measured energies. Depending on the orientation of the jets towards the Earth and other characteristics like the activity and luminosity of the radio and optical emission, AGNs are classified in several types [42]. A particularly interesting class of AGNs are *blazars*, which are those AGNs with one of the jets pointing towards the observer. Blazars represent one of the best chances to detect AGNs as individual point-like neutrino sources. They are generally intense gamma-ray sources, characterised by a spectral energy distribution that can still be explained by hadronic models [43]. The interest in blazars as promising neutrino emitters has recently been further motivated by the first convincing association of astrophysical neutrinos with a known cosmic object, the blazar TXS-0506+056 [44, 45] (see Section 1.4).

1.4 The IceCube signals

Neutrino astronomy has recently entered an exciting period thanks to two important discoveries: 1) the high-energy cosmic neutrino flux, compatible with isotropy, reported by the IceCube Collaboration [46, 47, 48, 49, 50, 51, 52], 2) the first compelling evidence (3σ significance) of neutrino emission from an astrophysical source, the blazar TXS 0506+056 [44, 45].

The first significant evidence of a diffuse flux of extraterrestrial neutrinos in the TeV-PeV range was claimed in 2014 relying on the "High-Energy Starting Events"

(HESE) sample of IceCube [46]. The HESE sample includes only events with interaction vertex contained within the detector volume and with total detected charge of at least 6000 photoelectrons (p.e.). This selection retains only high-energy events ($E_\nu \gtrsim 10$ TeV) and allows to drastically reduce the atmospheric background (both of atmospheric muons and atmospheric neutrinos). Using the HESE sample, the analysis performed on three years (988 days of livetime) of data found 37 neutrino candidate events with an expected background of 8.4 ± 4.2 cosmic-ray muon events and $6.6^{+5.9}_{-1.6}$ atmospheric neutrinos, rejecting a purely atmospheric explanation with a significance of 5.7σ. Subsequent updates of the HESE analysis, using extended livetimes of four [47] and six [48] years, included additional neutrino candidate events (54 and 82, respectively) confirming the excess with an increased significance of over 6σ. A maximum-likelihood method used to look for neutrino point-like sources in the sample did not yield significant evidence of clustering. The sky map with the directions of the 82 events recorded in six years of data taking is shown in Figure 1.3.

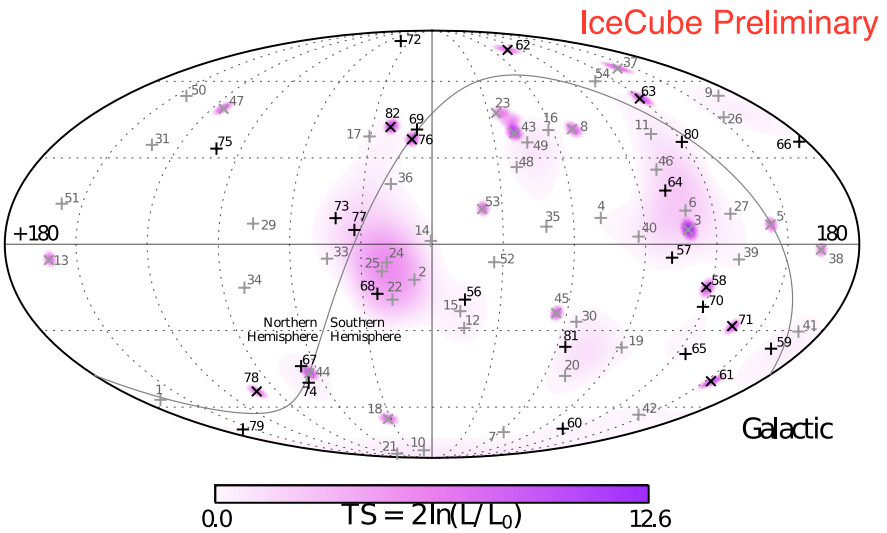

Figure 1.3: Arrival directions in galactic coordinates of the 82 events of the HESE sample recorded in 6 years of data taking of IceCube. Figure taken from [48].

The spectral energy distribution of the HESE events is well fitted with a single power-law of the form

$$\frac{d\Phi}{dE} = \Phi_{\text{astro}} \left(\frac{E_\nu}{100\text{TeV}} \right)^{-\gamma_{\text{astro}}} \times 10^{-18} [\text{GeV}^{-1}\text{cm}^{-2}\text{s}^{-1}\text{sr}^{-1}] \,, \tag{1.14}$$

with two free parameters: the normalization of the flux Φ_{astro} and the spectral index γ_{astro}. The latest HESE analysis performed with 7.5 years of data taking [49]

reported a best-fit astrophysical spectral index $\gamma_{\text{astro}} = 2.89^{+0.2}_{-0.19}$ and a best-fit astrophysical normalization $\Phi_{\text{astro}} = 6.45^{+1.46}_{-0.46}$.

Another significant observation of the cosmic neutrino flux is based on the analysis of the IceCube through-going track-like events from the Northern Hemisphere, hereafter referred to as "the Muon sample". The latest results of this analysis [52], update of [50] and [51], made use of muon neutrinos recorded during almost 10 years of data taking. The data are well described by an isotropic, unbroken power-law flux of the form of Equation 1.14, with a best-fit astrophysical spectral index $\gamma_{\text{astro}} = 2.28^{+0.08}_{-0.09}$ and a best-fit astrophysical normalization $\Phi_{\text{astro}} = 1.44^{+0.25}_{-0.24}$.

An additional measurement of the diffuse flux of high-energy astrophysical neutrinos was obtained using neutrino-induced cascades detected by IceCube in four years of data taking [53]. In this case, the single, unbroken power-law of Equation 1.14 is described by a best-fit spectral index $\gamma_{\text{astro}} = 2.48 \pm 0.08$ and a best-fit astrophysical normalization $\Phi_{\text{astro}} = 1.57^{+0.23}_{-0.22}$.

The three pairs of best-fit Φ_{astro} and γ_{astro} derived from the three different IceCube samples are shown in Figure 1.4 together with the respective confidence regions. While the three measurements appear to be compatible with each other within their 95.4% regions, several hypotheses have been proposed to explain the different best-fit points. The suggested hypothesis that a Galactic neutrino component, mainly observable in the Southern Hemisphere, could be a possible cause of the discrepancy between the HESE and the Muon samples [54] has been severely constrained by both ANTARES and IceCube [55, 56]. Other proposed explanations of the spectral tension include a two-component flux, either due to purely astrophysical sources or also to a beyond Standard Model contribution such as decaying heavy dark matter [57], and a prompt component of the atmospheric neutrino spectrum [58]. Recently, the IceCube Collaboration has considered the hypothesis of a spectral behaviour different than a single power-law by testing both a double power-law spectrum and various models of the astrophysical component available in the literature [49]. However, none of the alternative models could be significantly preferred compared to the single power-law description.

Another major breakthrough in the field of neutrino astronomy happened with the first possible association of a cosmic neutrino with an astrophysical source. On 22 September 2017, the IceCube Collaboration detected a high-energy neutrino-induced muon track, with a probability of 56.5% of being of astrophysical ori-

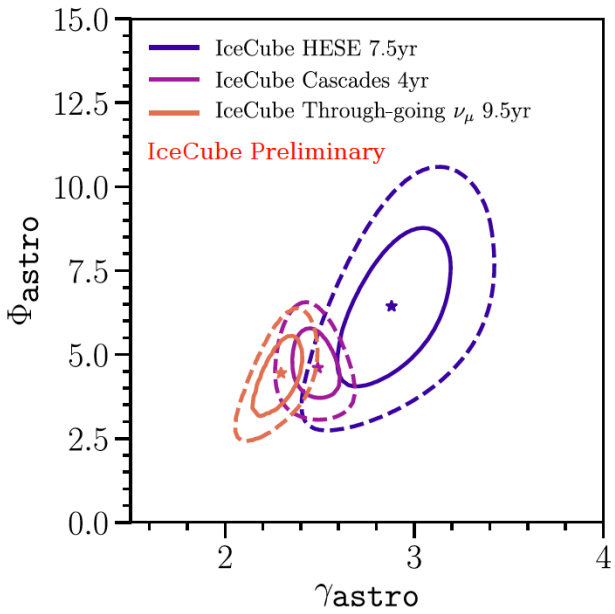

Figure 1.4: Best-fit parameters for the single power-law spectrum obtained using three different IceCube samples. The solid contours represent the 68.3% confidence regions, and the dashed contours the 95.4% confidence regions. Figure taken from [49].

gin [44, 59]. The neutrino-candidate event, IC170922A, was selected by the "Extremely High-Energy Events" (EHE) online event filter and reported through a Gamma-ray Coordinates Network (GCN) Circular [60]. It was soon found that IC170922A was coincident in direction and time with a gamma-ray flare from the blazar TXS 0506+056 detected not only by Fermi but also by MAGIC at higher energy [45]. The significance of this association was estimated to be of 3σ. Furthermore, the source was subsequently observed at other wavelengths including radio, optical, and X-rays [45]. Triggered by this association, the IceCube Collaboration performed a search for time clustering of lower energy neutrino events at the position of TXS 0506+056 assuming two different generic profile shapes: a Gaussian-shaped time window and a box-shaped time window [44]. The analysis yielded a 3.5σ evidence for an excess of 13 ± 5 high-energy neutrino events at the position of the blazar above the expectation from the atmospheric background between September 2014 and March 2015. The results of the time-dependent analysis performed at the coordinates of TXS 0506+056 are shown in Figure 1.5. Intriguingly, no gamma flare was observed from this blazar during the period of this "neutrino flare". The region around TXS 0506+056 was studied also by the ANTARES Collaboration using data collected from 2007 to 2017 [61] (see Section 7.1.3). The standard time-integrated point-source method fits 1.03

signal events at the location of the source, with a p-value of 3.4%.

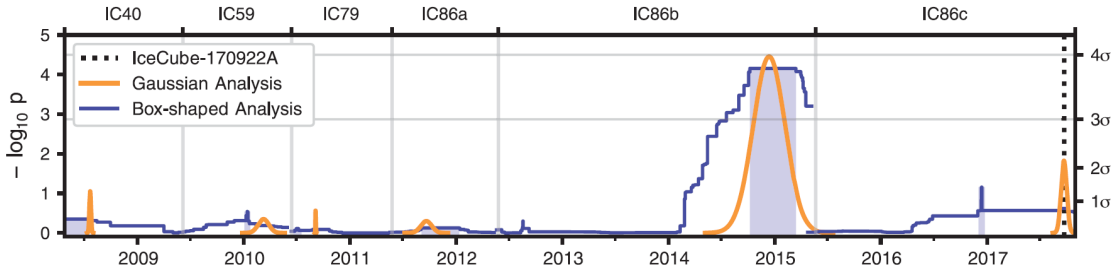

Figure 1.5: Results of the time-dependent analysis performed at the coordinates of TXS 0506+05 by the IceCube Collaboration. The results are presented in terms of observed p-value as a function of time using the Gaussian-shaped time profile (orange curve) and the box-shaped time profile (blue curve). The large blue band centered near 2015 represents the best-fit time window found using the box-shaped time profile. The vertical dotted line indicates the time of the IceCube-170922A event. Figure taken from [44].

These observations represent a major step forward in the field, thus strongly motivate further investigations. Indeed, the origin of most of the observed neutrino flux remains unknown. The neutrino flux of TXS 0506+056 can only account for less than 1% of the total observed astrophysical neutrino flux [44]. Moreover, recent searches for neutrino emission from the directions of blazars from the 2nd Fermi-LAT AGN catalogue performed by the IceCube Collaboration indicated that the blazars contribute less than about 40% - 80% (30%) to the total observed neutrino flux assuming an unbroken power-law spectrum $\Phi(E_\nu) \propto E_\nu^{-\gamma}$ with $\gamma = 2.0$ [44] ($\gamma = 2.5$ [62]). The possible contribution of the blazar population could be larger when accounting not only for Fermi-LAT sources but also for blazars further away and not resolved by Fermi-LAT observations.

Interpreting the neutrinos observed from TXS 0506+056 in the multi-messenger and multi-wavelength context is also challenging. In the single-zone emission picture, in which γ-rays and high-energy neutrinos are produced in a single emission region in the jet of the blazar, a leptonic scenario with a radiatively subdominant hadronic component has been suggested as an explanation for both the electromagnetic and the neutrino emission observed in the 2017 flare [63, 64, 65]. Most of the single-zone scenarios predict a physical luminosity that significantly exceeds the Eddington luminosity during the flare. In order to address this issue, multizone models, in which the photon and neutrino emissions originate from different regions in the jet, have also been proposed [63, 65].

On the other hand, the 2014-15 neutrino flare, being characterised by no significant electromagnetic activity and a relatively large number of observed

neutrinos, is much harder to describe using conventional models. Different types of considered lepton-hadronic scenarios succeed in accommodating only two to five neutrino events during the period of the flare in order for the predicted multi-wavelength emission levels to be compatible with the observations [66]. A reprocessing of the electromagnetic energy emitted with neutrinos into energy ranges not covered by observations during the neutrino flare (in particular sub-eV or MeV) may explain the lack of detected electromagnetic activity during the 2014-15 neutrino flare [65]. Future electromagnetic monitoring of the whole spectrum will be needed to constrain this hypothesis.

2

Neutrino detection

While the very small interaction probability of neutrinos makes them uniquely valuable astronomical messengers, it also makes their detection extremely challenging. Since neutrinos are only affected by the weak interaction, detection must rely on secondary particles produced in neutrino interactions. High-energy neutrino telescopes, whose detection principle was first suggested by M. A. Markov in 1960 [67], are designed to detect the charged leptons produced when a neutrino interacts with material around or inside the detector. The detector, a three-dimensional array of photomultiplier tubes (PMTs) inside a transparent medium like water or ice, collects the Cherenkov radiation induced by the passage of the relativistic charged particles inside or near the instrumented volume. The information provided by the number of Cherenkov photons detected, their location, and their arrival times is used to infer the arrival direction of the parent neutrino and an estimation of its energy. Such detectors are installed at great depths and optimised to detect the light from up-going particles produced by neutrinos which have traversed the Earth in order to limit the background of down-going atmospheric muons. The method used to detect high-energy cosmic neutrinos by neutrino telescopes is described in this Chapter.

2.1 Neutrino interactions

High-energy neutrinos interact in the target material via either charged current (CC) or neutral current (NC) weak interactions,

$$\textbf{CC: } \nu_l + N \xrightarrow{W^{\pm}} l + X \,, \tag{2.1}$$

$$\textbf{NC: } \nu_l + N \xrightarrow{Z^{0}} \nu_l + X \,, \tag{2.2}$$

where ν_l represents an incoming neutrino or antineutrino of a particular flavour (electron, muon, or tau), N the target nucleon, l an outgoing charged antilepton or lepton of the appropriate flavour, and X the hadronic cascade. The CC interaction is mediated by a $W^{\pm}$ boson, while the NC interaction is mediated by the Z^0 boson. The neutrino-nucleon cross section as a function of the neutrino energy is shown in Figure 2.1. The most probable interactions are neutrino CC interactions, with a cross section higher than that of neutrino NC interactions by a factor of three. Below energies of 10^5 GeV, the antineutrino interactions are the least probable ones with a cross section lower than that of neutrinos by a factor of two. High-energy neutrinos can also interact with bound electrons in the target medium. However, the rate of this interaction is mostly negligible due to the electron small mass, except for electron antineutrinos at the Glashow resonance [68] energy (6.3 PeV).

Different types of neutrino interactions with nucleons produce distinct observable signatures in a neutrino telescope. The produced signatures can be described in terms of two main event topologies: *tracks* and *showers*. Track events are originated by relativistic muons that can travel large distances through the medium with the Cherenkov light being constantly emitted along the track. Hadronic and electromagnetic cascades produce shower events characterised by an almost spherically symmetric light emission. All the possible event signatures observable in a neutrino telescope are represented in Figure 2.2 and briefly described below.

CC interactions of muon neutrinos. When a muon neutrino interacts with a nucleon via CC interaction, a hadronic shower and an outgoing muon are produced. Depending on the energy that has been transferred to the lepton, the muon can propagate for a few metres (at $E_\nu \approx 1$ GeV) up to several kilometres (at $E_\nu \gtrsim 1$ TeV), producing a long track event before decaying into an electron. If the muon decay or the neutrino interaction happens inside the detector volume,

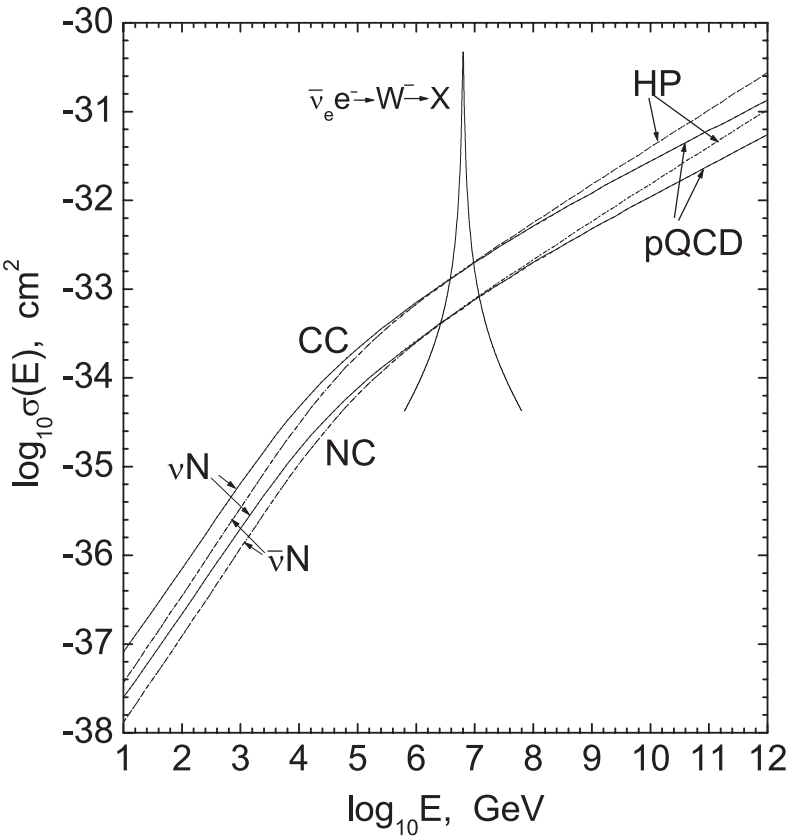

Figure 2.1: Neutrino-nucleon cross sections as a function of the neutrino energy according to the CTEQ5 parton distributions [69]. The cross sections are shown for neutrinos (solid lines) and antineutrinos (dashed lines), and for CC and NC interactions, separately. The cross section of the Glashow resonance (electron antineutrino-electron) is also shown. The HP and pQCD discrepancies are due to the different extrapolation techniques in the model. Figure taken from [70].

one of the two showers is observed, and the event signature is called lollipop or inverted lollipop, respectively. CC interactions of muon neutrinos are especially interesting in a search for cosmic point-like sources of neutrinos in which a good angular resolution is necessary, as the long lever arm of the track topology allows for a good reconstruction of the muon direction, which in turn is an accurate estimation of the parent neutrino direction. The average angle $\langle\theta_{\nu\mu}\rangle$ between the incident neutrino and the outgoing muon can be approximated by [72]

$$\langle\theta_{\nu\mu}\rangle \leq \frac{0.6^\circ}{\sqrt{E_\nu/1\,\mathrm{TeV}}}\,, \tag{2.3}$$

where E_ν is the energy of the incoming neutrino. For energies above 10 TeV, the average angle is smaller than 0.2°. The direction of the muon is also affected by multiple scattering while propagating through matter. However, this effect

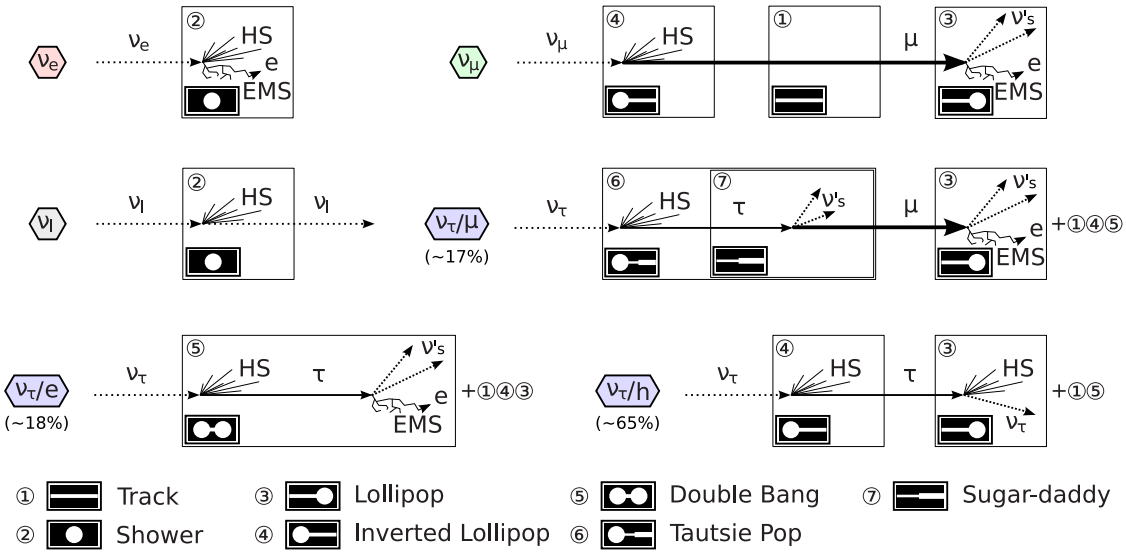

Figure 2.2: Neutrino event topologies that can be distinguished in a neutrino telescope. The signature resulting from CC interactions of electron neutrinos (top-left), muon neutrinos (top-right), tau neutrinos (middle-right, bottom-left and bottom-right), and NC interaction of all-flavour neutrinos (middle-left), are shown. HS denotes hadronic shower and EMS, electromagnetic shower. Figure taken from [71].

is much smaller than $\theta_{\nu\mu}$ at energies and distances interesting for a neutrino telescope and can be neglected. The long track length of the muon allows to increase the effective detector volume as also muons originated far away from the instrumented volume can be detected. As an example, a muon with initial energy of $E_\mu = 10$ TeV can travel in water for ~5 km and reach the detector with more than 1 TeV of residual energy [1]. On the other hand, only a fraction of the muon energy is emitted inside the detector which makes it considerably harder to estimate the total muon energy.

CC interactions of electron neutrinos. In this case, an electron and a hadronic cascade are produced at the neutrino interaction vertex. The high-energy electron radiates photons via bremsstrahlung after few tens of centimeters of water/ice leading to the development of an electromagnetic cascade. Since both cascades are produced in the same interaction vertex, they cannot be distinguished, and a shower event type is observed. The relativistic particles generated within the electromagnetic shower induce Cherenkov radiation themselves. However, the longitudinal extension of the shower is of the order of a few meters, thus the shower appears as a point source of Cherenkov photons emitted almost isotropically along the shower axis. For this reason, the pointing accuracy for showers is much inferior to that achieved in the ν_μ channel. On the other

hand, the concentrated deposit of all the neutrino's energy provides a better estimation of its energy.

CC interactions of tau neutrinos. At the vertex of this interaction a hadronic cascade and a τ lepton are produced. The τ lepton is very short-lived (mean lifetime of $2.9 \cdot 10^{-13}$ s [73]) and, depending on its energy, can travel a few tens of meters before decaying either leptonically into an electron or muon (35% chance) or into hadrons (65% chance). A track event is observed in case the decay product is a muon; a shower is observed otherwise. For energies below $\sim$2 PeV and above $\sim$20 PeV the observed signature is a *lollipop* (shower and track) since either the second cascade cannot be distinguished from the initial one (low energies) or it develops outside the detector as the length of the tau path is larger than the scale of km^3 neutrino telescopes (high energies). For intermediate energies, both cascades can be observed and the signature is called *double-bang*. Double-bang events are particularly interesting since they can only be produced by tau neutrinos which in turn are a proof of cosmic emission.

NC interactions. The NC channel gives the same signature for all neutrino flavours. A hadronic shower and a neutrino are produced at the interaction vertex. Since a part of the energy of the parent neutrino is carried away by the outgoing neutrino, only the rest is deposited in the detector through the hadronic cascade. Therefore, the total energy of the incoming neutrino is much harder to estimate in this case.

2.2 Cherenkov radiation

The charged particles produced in the high-energy neutrino interactions are mainly relativistic, and are thus able to induce Cherenkov radiation [74]. When a charged particle crosses a transparent medium at a speed higher than the speed of light in that medium, it polarises the molecules along its trajectory, producing an overall dipole moment. When the electrons of the atoms restore to equilibrium, Cherenkov photons are emitted in a coherent front. This coherent front forms a cone with an angle with respect to the lepton direction (θ_C) given by

$$\cos\theta_C = \frac{1}{\beta n}\,, \tag{2.4}$$

where β is the velocity of the particle expressed as a fraction of the speed of light in vacuum c, and n is the refractive index of the medium. A schematic view of

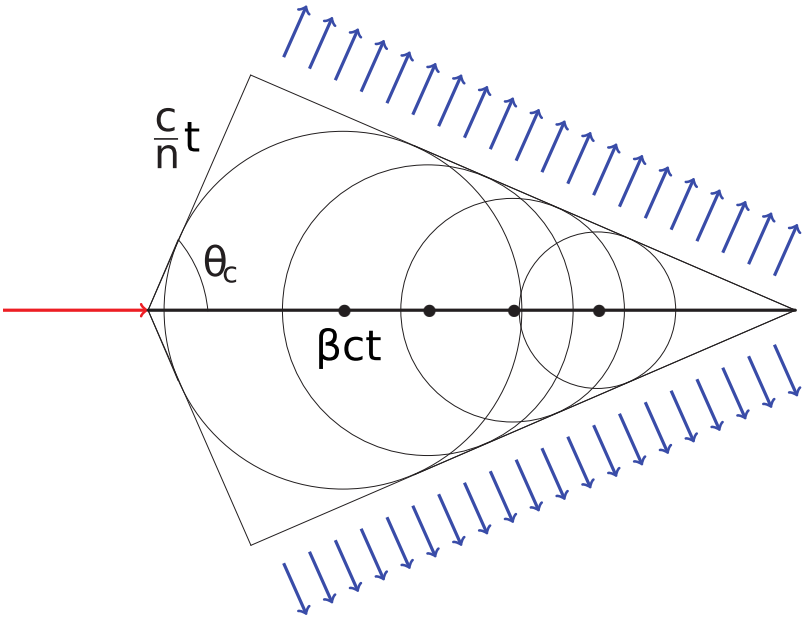

Figure 2.3: Scheme of the wavefront created through Cherenkov radiation. The variables used in Equation 2.5 are shown. Figure taken from [75].

the geometry of the Cherenkov emission is shown in Figure 2.3. For relativistic particles ($\beta = 1$) the Cherenkov angle is about 43° in seawater ($n = 1.36$) and about 41° in ice ($n = 1.32$). The expected amount of photons emitted per unit of length, x, and wavelength, λ, can be expressed as

$$\frac{d^2N}{d\lambda dx} = \frac{2\pi\alpha Z^2}{\lambda^2}\left(1 - \frac{1}{\beta^2 n^2}\right), \tag{2.5}$$

where α is the fine-structure constant and Z is the charge of the particle. From this formula it can be seen that shorter wavelengths (blue and UV range) contribute more significantly to the Cherenkov radiation. Therefore, neutrino telescopes use PMTs which are sensitive to these wavelengths.

2.3 Light propagation

Cherenkov photons travelling in the medium undergo processes of scattering and absorption. These effects significantly affect the capabilities of the telescope to reconstruct the direction of the incoming neutrino. Indeed, scattering changes the direction of propagation of the Cherenkov photons, while absorption reduces

the total amount of light hitting the PMTs. The effects of the medium on the propagation of the light of a given wavelength λ depend on the optical properties of the medium. These can be quantified by the coefficients of absorption $a(\lambda)$, scattering $b(\lambda)$, and attenuation $c(\lambda) = a(\lambda) + b(\lambda)$, or, alternatively, by the absorption, scattering and attenuation lengths ($L_a(\lambda) = a(\lambda)^{-1}$, $L_b(\lambda) = b(\lambda)^{-1}$, $L_c(\lambda) = c(\lambda)^{-1}$), which represent the path after which a beam of initial intensity I_0 at wavelength λ is reduced in intensity by a factor of $1/e$, according to the relation

$$I_i(x, \lambda) = I_0(\lambda) e^{-x/L_i(\lambda)} \, ; i = a, b, c \tag{2.6}$$

where x is the path traversed by the light.

A more precise description of the scattering process takes into account, in addition to the geometric scattering length $L_b(\lambda)$, the scattering angular distribution. This effect is quantified by the effective light scattering length $L_b^{eff}(\lambda)$ which is related to the scattering length $L_b(\lambda)$ and the average cosine of the scattering angle $\langle \cos\theta \rangle$ by the relation

$$L_b^{eff}(\lambda) \simeq L_b(\lambda)/(1 - \langle \cos\theta \rangle) \, . \tag{2.7}$$

As water and ice are characterised by different optical properties, the medium in which the detector is deployed can affect its performances. Ice can count on a larger absorption length $L_a(\lambda)$ with respect to water. As a consequence, the same instrumented volume in ice corresponds to a larger effective volume than in water since Cherenkov photons can travel for longer distances before being absorbed. On the other hand, the effective scattering length $L_b^{eff}(\lambda)$ in ice is smaller than in water, causing a larger degradation of the angular resolution of the neutrino-induced muons traversing the ice. An additional difference that distinguishes seawater from ice is that seawater hosts ^{40}K nuclei and organisms that produce bioluminescence, both sources of optical background. The optical properties of water and ice in specific sites and the optical background will be described in more detail in Chapter 3.

2.4 Physical background

The two main sources of physical background for a neutrino telescope are atmospheric muons and atmospheric neutrinos. Both are produced mainly by

decays of charged pions and kaons originated in hadronic showers produced by cosmic rays interacting with atmospheric nuclei. Despite neutrino telescopes are placed at large depths in order to reduce the background, high-energy muons can penetrate the atmosphere and up to several kilometers of ice/water and represent the bulk of reconstructed events in any large volume neutrino detector. However, the muons cannot traverse the whole diameter of the Earth. Therefore, an effective method to reject this background is to select only events with an upward reconstructed direction. The remaining background due to down-going atmospheric muons wrongly reconstructed as up-going is rejected by means of additional strategies.

The atmospheric neutrinos represent an irreducible source of background since they can cross the Earth without interacting. Different techniques are employed to identify the signal over the background of atmospheric neutrinos depending on the analysis. In searches for point-like and extended sources of cosmic neutrinos, the signal events are expected to cluster in the vicinity of the source and they can be distinguished from atmospheric neutrinos as the latter are distributed almost isotropically over the sky. In searches for diffuse fluxes, where the previous strategy is not valid, the fact that signal and background have different energy spectrum is exploited.

The flux of atmospheric muons and the flux of muons induced by atmospheric neutrinos as a function of the cosine of the zenith angle are shown in Figure 2.4. The flux of atmospheric muons exceeds the flux induced by atmospheric neutrino interactions by many orders of magnitude, decreasing with increasing detector depth and disappearing for upward directions. An enhancement of atmospheric neutrinos at the horizon ($\cos\theta \simeq 0$) is observed. This is due to the fact that the air density decreases with the altitude and therefore horizontal pions travel a larger path without interacting, yielding a larger probability to decay and to produce neutrinos.

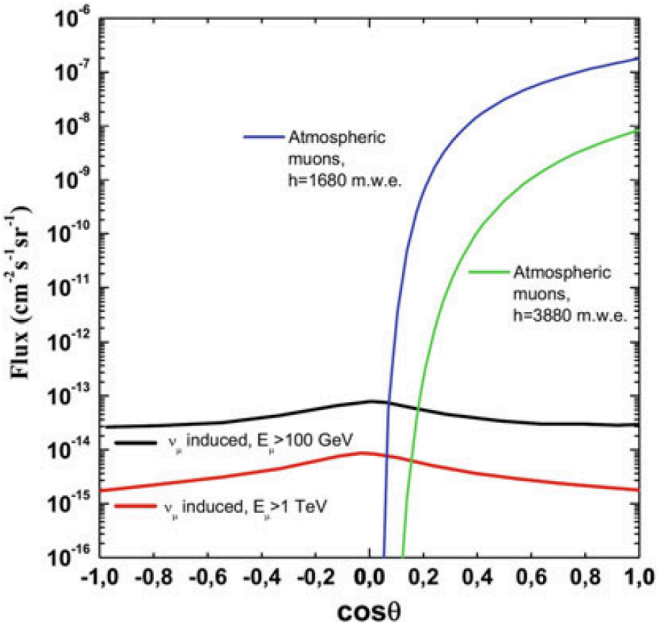

Figure 2.4: Flux as a function of the cosine of the zenith angle of atmospheric muons for two different depths and for muons induced by CC interactions of atmospheric muon neutrinos for two different muon energy thresholds. Up-going (down-going) events have $\cos\theta < 0 (> 0)$. Figure taken from [1].

3

Neutrino telescopes

The history of neutrino telescopes starts in the late 1970s with the DUMAND project [76] which attempted to deploy a detector in the Pacific Ocean, off the shore of the island of Hawaii. Although the project was cancelled in 1995 because of technical and financial problems, the initiative set the basis for subsequent cosmic neutrino telescopes. The DUMAND goal to begin high-energy neutrino astronomy was carried forward with the Baikal telescope [77], located under the surface of the Russian Lake Baikal, and with the AMANDA telescope [78], in the South Pole ice. Baikal has been operating since 1993 and it is being upgraded in the Baikal Gigaton Volume Detector (Baikal-GVD) [79]. AMANDA, whose first string was deployed in 1993, has been the precursor of the current largest neutrino telescope in the world, IceCube [80]. The pioneering DUMAND experience has being continued in the Mediterranean Sea by the ANTARES [81], NEMO [82] and NESTOR [83] collaborations, whose joint effort will lead to the construction of the largest network of neutrino telescopes, KM3NeT [84].

The two neutrinos telescopes used in the search for neutrino sources presented in Chapter 7 (ANTARES and IceCube) will be described in detail in this Chapter together with the forthcoming KM3NeT network, whose point-source sensitivity is studied in Chapter 7 as well.

3.1 ANTARES

ANTARES (Astronomy with a Neutrino Telescope and Abyss environmental RESearch) [81] is an under-water neutrino telescope located 40 km offshore from Toulon, France at $42°48'$ N, $6°10'$ E, anchored about 2500 m below the surface of the Mediterranean Sea. The detector was completed in mid 2008 but the data taking started in early March 2006 when the first line was deployed, making it the first operating under-sea neutrino telescope. The Cherenkov light induced by charged particles produced in neutrino interactions is detected by an array of 885 PMTs distributed along 12 vertical lines and facing $45°$ downward in order to optimise the detection of light from up-going particles. Being in the Northern Hemisphere and at intermediate latitudes, the ANTARES telescope has a privileged view of the Galactic Centre and Galactic Plane, where many neutrino source candidates are expected (see Chapter 1).

3.1.1 Detector layout

Figure 3.1 shows a schematic view of the ANTARES detector. A total of 12, 450 m long, flexible lines are anchored at the sea floor by means of a dead weight and are kept vertical with a buoy on their top, at a horizontal distance of 60-70 m from each other. Starting 100 m above the sea floor, each line holds 25 storeys separated by a distance of 14.5 m and connected by electro-optical mechanical cables. A storey is a titanium structure that hosts the local control module (LCM), i.e. a titanium cylinder containing the offshore electronics, and three optical modules (OMs). The OMs are pressure resistant glass spheres housing 10-inch Hamamatsu PMTs. Since the upper five storeys of line 12 hold acoustic neutrino detection hardware and are not equipped with any OM, the total number of OMs in the detector is 885. A schematic view of the ANTARES OM is shown in Figure 3.2. The OMs are horizontally arranged around the LCM with an equal spacing of $120°$ and face $45°$ downward. The orientation of the OMs not only optimises their acceptance to the light from up-going particles but also reduces the effect of sedimentation and biofouling (see Section 3.1.2). In each OM, the glass sphere is optically coupled to the PMT by means of an optical gel of refractive index 1.4. A hemispherical μ-metal magnetic cage surrounds the bulb of the PMT in order to shield it from the effects of the Earth's magnetic field. The PMT has a photocathode area of 500 cm^2 and is sensitive to photons with wavelengths between 300 nm and 600 nm, thus matching the frequency

range of the Cherenkov radiation.

The 12 lines are arranged in an octagonal configuration and are all connected to a Junction Box (JB). A String Control Module (SCM) at the bottom of each line contains the electronics for the data transfer between the string and the JB. The JB is linked to the shore station via an electro-optical cable (the Main Electro-Optical Cable, MEOC), through which the detector is powered, the data are collected and a clock signal, responsible for the synchronisation of the different detector elements, is distributed.

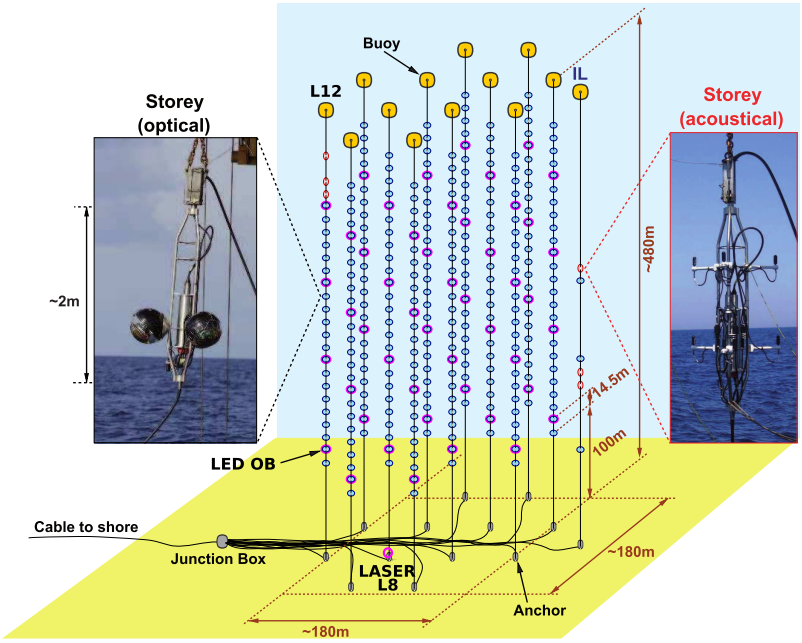

Figure 3.1: Schematic view of the ANTARES detector. Figure taken from [71].

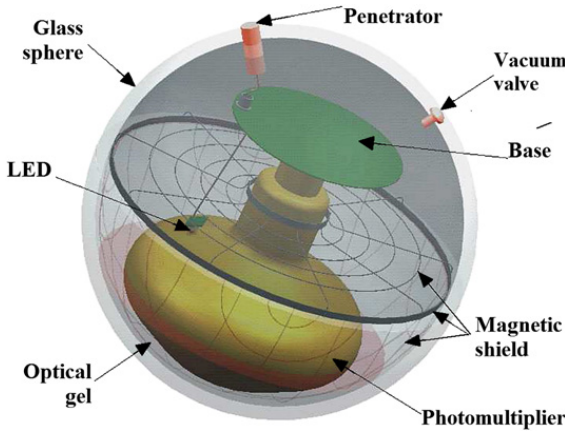

Figure 3.2: Schematic view of the ANTARES optical module. Figure taken from [85].

3.1.2 Site characteristics

Prior to the deployment of the ANTARES detector, the suitability of the site was evaluated by measuring those environmental parameters that can significantly affect the detector performance.

Water properties. Dedicated studies of the water properties at the ANTARES site were conducted by means of a measuring system mounted on an autonomous line [86]. The measurements of the absorption and effective scattering lengths ($L_a(\lambda)$ and $L_b^{eff}(\lambda)$ defined in Section 2.3) consisted in analysing the time-of-flight distributions of photons emitted from a pulsed isotropic light source of UV and blue wavelengths and detected by a PMT at different distances from the source. Three sets of measurements were performed over a period of about two years. The values of the measured absorption and effective scattering lengths for blue (UV) light are $L_a(\lambda) \simeq 60(26)$ m and $L_b^{eff}(\lambda) \simeq 265(122)$ m, with significant ($\sim$15%) time variability. Uncertainties in the knowledge of the water properties are estimated to induce a 10% and 5% uncertainty in the angular resolution and effective volume of the detector, respectively [86]. The results of the measurements are shown in Figure 3.3. More recent measurements of the water properties were taken during the ANTARES operations [87], providing values of the absorption length and the scattering length for a wavelength $\lambda = 470$ nm of $L_a = 48 \pm 8$ m and $L_b = 57 \pm 8$ m, respectively.

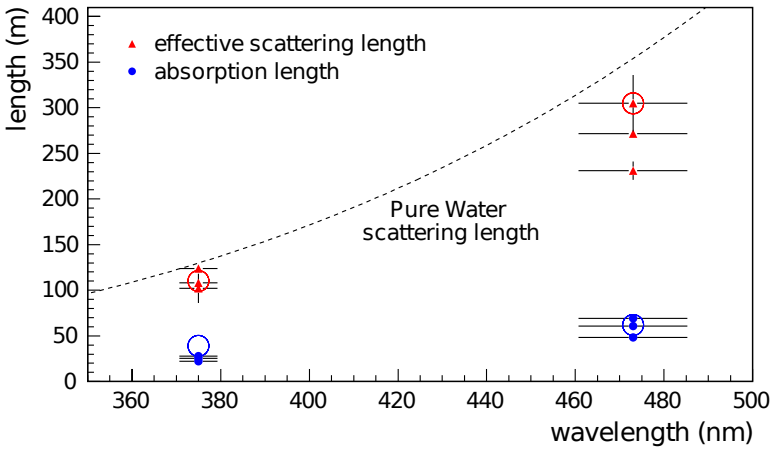

Figure 3.3: Water properties at the ANTARES site. The red (blue) symbols represent the effective scattering (absorption) length measured at different epochs. Values were measured at two different wavelengths. The large circles show, for comparison, the estimations of the absorption and effective scattering lengths in pure seawater. The dashed line is the scattering length in pure water, which represents the upper limit for the effective scattering length in seawater. Figure taken from [86].

Biofouling and sedimentation. A series of in-situ measurements were performed in order to study the effect of the accumulation of small particles (sedimentation) and the adhesion of bacteria (biofouling) to the external surface of the OMs [88]. The measurements consisted in illuminating a pressure-resistant glass sphere (similar to those used for the OMs), containing five photo-detectors with two blue light LEDs, over a period of eight months. In order to study the dependency of the effects on the inclination of the surface, the five photo-detectors were glued to the inner surface of the sphere at different zenith angles. The studies showed that, for surfaces facing downward as the ANTARES PMTs, the loss of transmissivity due to the fouling is negligible.

Optical background. The decay of radioactive elements present in seawater and the light produced by living organisms, the so-called *bioluminescence*, represent unavoidable sources of optical background for ANTARES [72]. The former is mainly due to ^{40}K, the most dominant of all radioactive isotopes present in natural seawater. The two most probable ^{40}K decay channels are:

$$^{40}\mathrm{K} \rightarrow ^{40}\mathrm{Ca} + e^- + \bar{\nu}_e \quad (\mathrm{BR} = 89.3\%)\,, \tag{3.1}$$

$$^{40}\mathrm{K} + e^- \rightarrow ^{40}\mathrm{Ar} + \nu_e + \gamma \quad (\mathrm{BR} = 10.7\%)\,. \tag{3.2}$$

Both can lead to the production of optical noise. The electron produced in the first decay is likely above the threshold for Cherenkov light production. The photon originating in the second process has an energy of 1.46 MeV and can therefore lead to electrons above the Cherenkov threshold through Compton scattering. The intensity of the optical background due to ^{40}K depends on its concentration in water. As the salinity in the Mediterranean Sea does not suffer from large variations due to location and time, ^{40}K produces an almost constant baseline in the counting rates of all PMTs.

On the other hand, the optical background due to bioluminescence depends on the concentration of the luminescent organisms, which varies with location, depth, and time. A decrease in abundance with increasing depth is observed. Moreover, seasonal effects are present in bioluminescence, with the maximal intensity reached during spring [89]. The intensity of this optical background can exceed by several orders of magnitude the one due to ^{40}K, inducing high bursts in the counting rates of PMTs.

Overall, ^{40}K and bioluminescence together produce an almost constant baseline rate of $\sim$60 kHz, with peaks due to the seasonal effects of bioluminescence. The

baseline rate measured in ANTARES over a period of more than ten years is shown in Figure 3.4.

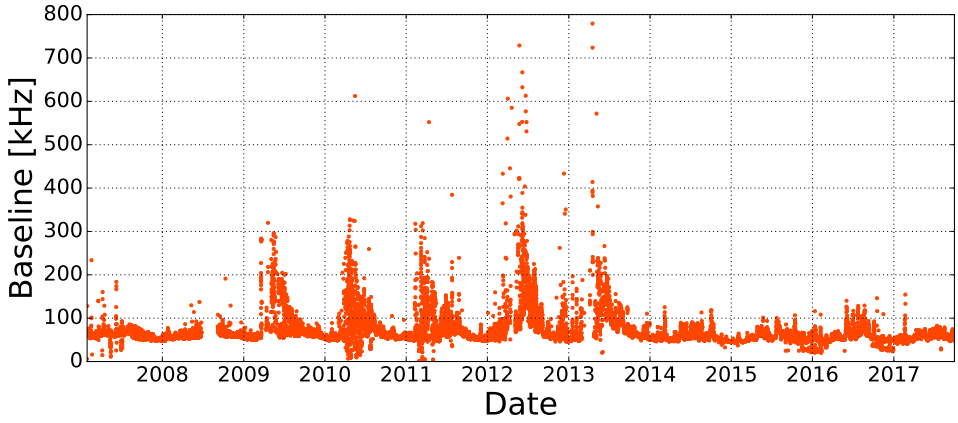

Figure 3.4: Baseline rate measured in ANTARES as a function of time. Higher rates during Spring are visible from 2009 to 2013. Figure taken from [90].

3.1.3 Data acquisition and triggers

The analogue signals registered by the PMTs need to be transformed into a format suitable for the purpose of physics analyses. This is achieved through a chain of steps handled by the ANTARES Data AcQuisition system (DAQ) [85]. The DAQ process is based on an "all-data-to-shore" strategy, i.e. all the information recorded by the PMTs, digitalised offshore, is transported to shore where it is filtered and stored. The single piece of information recorded by the PMTs, the so-called *hit*, consists in the time and integrated charge of the signal recorded during an integration time of 35 ns. The DAQ begins with the digitalisation of the hits by means of two Analogue Ring Sampler (ARS) chips located in the LCM of each OM. A threshold of 0.3 p.e. (L0 threshold) is applied on the integrated charge in order to reduce the dark current noise of the PMTs. A local clock and two time-to-voltage converters (TVCs) in each LCM are used to timestamp every hit above threshold. The ARS chips work in a token-ring configuration in order to reduce the impact of the dead time of 200 ns which follows the integration time.

The signal collected by the LCMs is transferred to the JB and then sent to the shore station using a Dense Wavelength Division Multiplexing (DWDM). In the shore station, a farm of computers is used to filter and store the data.

Because of the high optical background, which results in high photon detection rates of the PMTs, the onshore handling of all raw data is the main challenge of the

ANTARES DAQ system. The optical background determines a data output rate of the detector between 0.3 GB/s and 1 GB/s. A data filtering process is performed by the DataFilter programs which applies various algorithms (triggers) [91] to look for interesting hit patterns. A summary of the most relevant triggers follows.

L1 trigger. This trigger requires that two or more hits on one storey occur within 20 ns or that a single hit surpasses a threshold of 3 photoelectrons. The aim of the L1 trigger is to reduce the optical background since hits from bioluminescence or ^{40}K are usually uncorrelated in time and of low intensity.

3N trigger. The 3N trigger [92] intends to find muon tracks. It exploits the fact that the Cherenkov photons induced by a muon are correlated in space and time through the relation

$$|t_i - t_j| \leq r_{ij}\frac{n}{c}\,, \tag{3.3}$$

where t_i and t_j are the registered time of the two hits at the PMTs i and j, r_{ij} is the distance between the PMTs, n is the refraction index in water, and c is the speed of light in vacuum. If at least five pairs of L1 triggers fulfil this requirement, a further criterion is applied. A scan of 210 isotropically distributed directions in the sky is performed looking for clusters of hits in a time window compatible with the Cherenkov emission. If five or more L1 triggers fulfil at least one of the considered directions, the event is recorded with this trigger.

T3 and 2T3 triggers. The T3 trigger [93] requires two L1 triggers to happen in three consecutive storeys within a specific time window. This time window is 100 ns in case that the two storeys are adjacent and 200 ns for next-to-adjacent storeys. The 2T3 trigger requires two T3 triggers to happen within 2.2 μs with at least three L1 triggers in the same line, or four in the whole detector.

For the point-like and extended source analyses with the ANTARES data presented in Chapter 7, only ANTARES events recorded with the 3N and the 2T3 triggers are considered.

3.1.4 Detector calibration

In order to achieve a good quality in the reconstruction of the events, the position, charge and time of each hit recorded by the OM needs to be determined precisely. To this scope, regular calibration procedures are performed.

Position calibration. Due to the flexibility of the detection lines, the top storeys can be dragged by up to 15 m under the effect of deep-sea currents [94]. This effect needs to be constantly monitored as, in order to ensure a good angular accuracy in the reconstruction, it is necessary to know the position of the OMs with a precision of 10 cm. This is achieved by means of a calibration system based on acoustic devices, a tiltmeter and a compass. The acoustic devices consist of a system of acoustic transceivers and detecting hydrophones. Storeys 1, 8, 14, 20 and 25 of each line are equipped with a hydrophone which measures high-frequency acoustic signals (40-60 kHz) emitted every two minutes by transceivers placed at the anchor of each line. An additional emitter is located at a distance of 145 m from the detector. Using the travel time of the acoustic signals, it is possible to determine the position of each of the hydrophones by triangulation. A polynomial fit of these positions is then performed to reconstruct the shape of the whole line. Moreover, a Tiltmeter-Compass System which consists of a set of bi-axial tiltmeters and compasses installed in the LCM of each storey is used to determine the orientation of the OM by measuring its pitch, roll and heading angles.

Charge calibration. The working principle of the PMTs is based on the amplification by secondary emission of the number of electrons generated by photoelectric effect (photoelectrons) when a photon strikes the photo-cathode surface. The charge of the signal generated by the photoelectrons is digitised by an Analog-to-Voltage Converter into a value, hereafter called AVC, related to the number of photoelectrons, Q_{pe}, that caused the signal through the equation:

$$Q_{pe} = \frac{\mathrm{AVC} - \mathrm{AVC_{0pe}}}{\mathrm{AVC_{1pe}} - \mathrm{AVC_{0pe}}}\,, \tag{3.4}$$

where $\mathrm{AVC_{0pe}}$ is the value of AVC corresponding to zero photoelectrons (pedestal value) and $\mathrm{AVC_{1pe}}$ corresponds to the single photoelectron peak. Regular charge calibration runs are performed to determine these two values. The pedestal value is obtained by digitising the output signal of the PMT at random times, while the single photoelectron peak is determined exploiting the optical background which produces primarily single photons at the photocathode level. The measured values degrade over time, making it necessary to tune the high-voltage supply of the PMT (high-voltage tuning) necessary in order to maintain the 0.3 p.e. threshold.

Time calibration. The aim of the time calibration performed within ANTARES is to monitor the absolute timing of the events with respect to the universal time and the relative calibration among PMTs. A detailed description of the time

calibration methods is given in Chapter 5.

3.2 KM3NeT

KM3NeT (KM3-scale Neutrino Telescope) [84] is a research infrastructure housing the future network of under-water neutrino telescopes currently being deployed in the Mediterranean Sea. It will comprise two neutrino detectors with different granularity of optical modules in order to target different neutrino energies: KM3NeT/ARCA (Astroparticle Research with Cosmics in the Abyss), a bigger detector with a sparser configuration aiming at detecting high-energy cosmic neutrino sources, and KM3NeT/ORCA (Oscillation Research with Cosmics in the Abyss), a smaller and denser detector dedicated to the study of neutrino mass hierarchy. The construction process will consist of a multiple stages implementation with increasing volume from about 0.1 km^3 in the first construction phase to a volume of several km^3 in the final phase, as described in the following section.

3.2.1 Detector layout

The layout of the KM3NeT detectors is based on a modular design made of building blocks of 115 detection strings called detection units (DUs). Each DU comprises 18 Digital Optical Modules (DOMs), each one housing 31 PMTs. When completed, the KM3NeT telescope will consist of seven building blocks distributed on three sites in the Mediterranean Sea as shown in Figure 3.5:

- KM3NeT-Fr: located at $42^\circ\ 41'$ N, $6^\circ\ 02'$ E at a depth of 2475 m, about 40 km offshore from Toulon, and 10 km west of the site of the ANTARES telescope;
- KM3NeT-It: located at $36^\circ\ 16'$ N, $16^\circ\ 06'$ E at a depth of 3500 m, about 100 km offshore from Porto Palo di Capo Passero, Sicily, Italy;
- KM3NeT-Gr: located in the open sea south-west of Pylos, Greece. Various locations are under investigation.

The first construction stage, Phase 1, comprises 24 DUs of ARCA located at the KM3NeT-It site and 6 DUs of ORCA, located at the KM3NeT-Fr site, corresponding in total to about 0.2 building blocks. The Phase 2 construction stage will comprise a total of three building blocks: two ARCA blocks and one ORCA block.

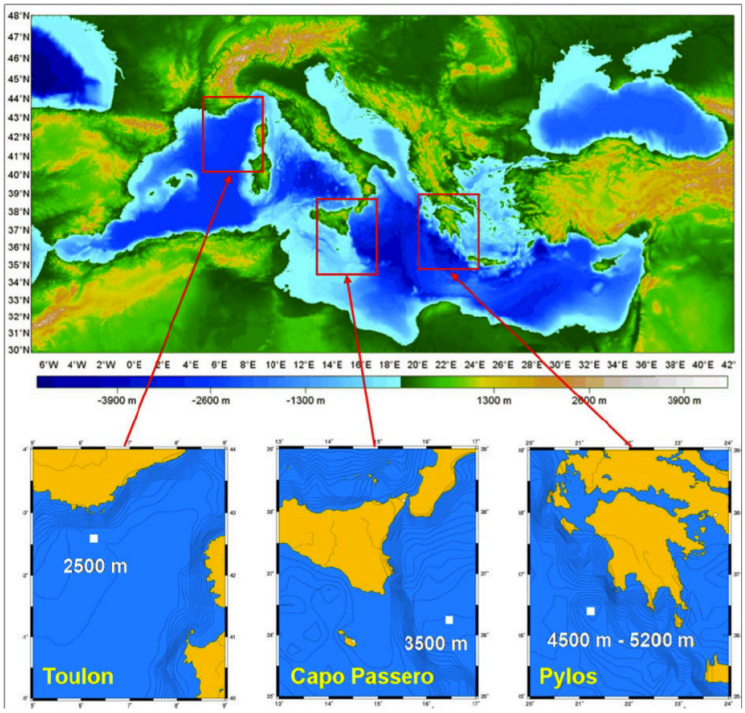

Figure 3.5: Location of KM3NeT's three installation sites. Figure taken from [95].

Their layout is shown in Figure 3.6. To date, one ARCA string and four ORCA strings have been deployed and are successfully taking data. As ARCA and ORCA target different neutrino energies, the spacing between lines/DOMs is optimised accordingly. For ARCA, the strings are about 700 m high, separated by 95 m on average, with DOMs spaced 36 m apart in the vertical direction, starting about 80 m from the sea floor, instrumenting a total volume of about 1 km^3. For ORCA, the DUs are 200 m high, horizontally separated by about 20 m, with DOMs spaced 9 m apart in the vertical direction, starting about 40 m from the sea floor, for a total volume about 125 times smaller than that of ARCA.

The KM3NeT DUs are flexible strings made of two thin (4 mm diameter) parallel Dyneema^{TM} ropes fixed to the sea floor and held close to vertical by a submerged buoy. A schematic view of a KM3NeT DU is shown in Figure 3.7-left. The DOMs are attached to the ropes via a titanium collar. Moreover, a vertical electro-optical cable runs along the string. It consists of a plastic tube containing two copper wires for the power transmission and 18 optical fibres for the data transmission.

The KM3NeT DOM is a transparent 17-inch diameter glass sphere comprising two separate hemispheres and housing 31, 3-inch diameter, photomultiplier tubes and their associated readout electronics. A photograph of a KM3NeT DOM is shown in Figure 3.7-right. The advantages of multiple small PMTs over the

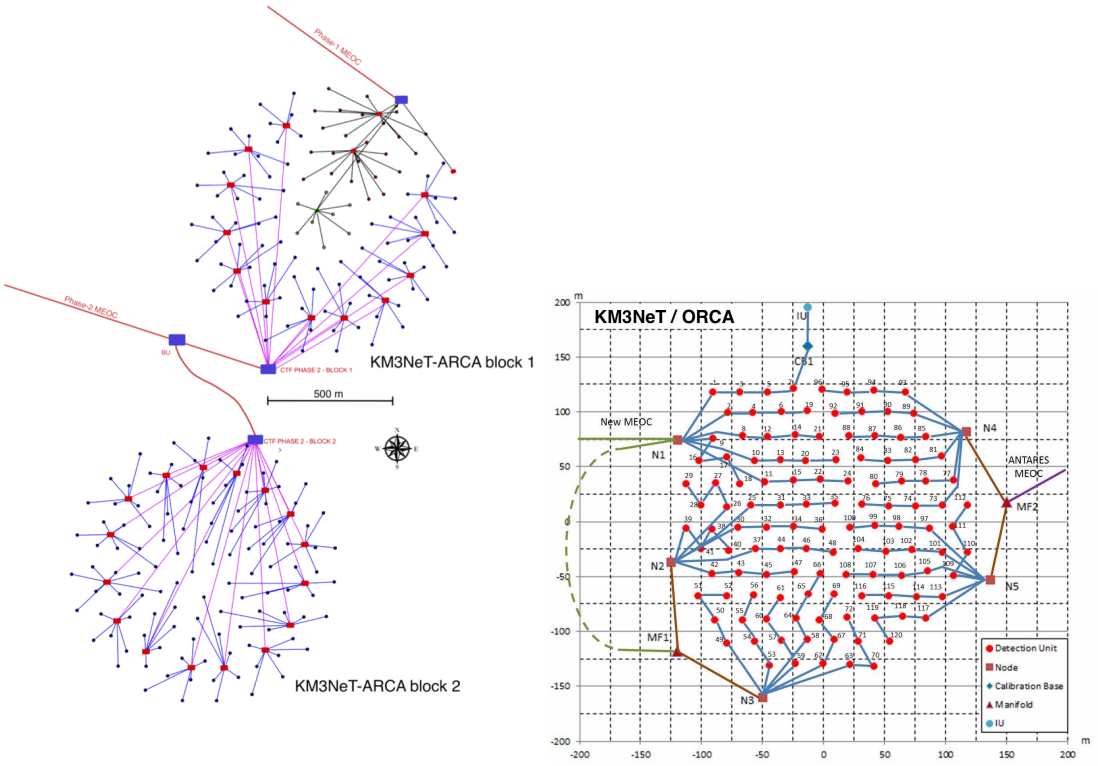

Figure 3.6: Left: layout of the two KM3NeT/ARCA building blocks in Phase 2. The 24 DUs of Phase 1 are represented as red dots. Right: layout of the KM3NeT/ORCA building block in Phase 2. Figures taken from [84].

traditional optical modules using single large PMTs are several: the photocatode area increases by a factor 3 to 4, it provides an almost uniform angular coverage, and it allows for a better rejection of the optical background. Indeed, as the photo-cathode is segmented, more than one photon arriving at the DOM can be identified. The PMTs are distributed on the DOM surface in five rings of six PMTs plus a single PMT at the bottom pointing vertically downwards. A distance of $30°$ in zenith separates successive rings, while PMTs on the same ring are arranged $60°$ apart in azimuth. As in ANTARES, an optical gel assures optical contact between the PMTs and the glass sphere. Apart from the PMTs, the DOM also contains an LED, a compass/tiltmeter, and an acoustic piezo sensor for time, orientation, and position calibration, respectively.

3.2.2 Data acquisition and triggers

The same "all-data-to-shore" data taking approach used in ANTARES is employed in KM3NeT: all analogue signals from the PMTs above a threshold of

Figure 3.7: Left: schematic view of the KM3NeT detection string with the DOMs attached. The actual number of DOMs per string is 18. Right: photograph of a KM3NeT Digital Optical Module. Figures taken from [84].

0.3 p.e. (*hits*) are digitised and sent to shore where they are processed by a farm of computers. For each hit, the information of the arrival time and of the Time over Threshold (ToT), i.e. the time the signal is above the 0.3 p.e. threshold, is stored in 6 bytes of data. Overall, a total data rate of 25 Gb/s is sent by each building block, which makes it necessary to filter and reduce the data before storing it on disk. In addition to physics data, the information of the singles rates of all PMTs is also recorded. This data provides information on the status of the optical background which is used in the simulation and reconstruction processes. Furthermore, a considerable amount of data volume sent to shore is represented by the data from the acoustics positioning system.

The 0.3 p.e. condition (L0 trigger) is the only filter applied offshore. The most basic trigger performed onshore is the L1 filter. It requires a coincidence of two (or more) L0 hits from different PMTs in the same optical module within a time window of 10 ns. Most of the L1 rate per optical module, estimated to be about 1000 Hz, arises from ^{40}K decays ($\sim$60%), while the remaining part is due

to random coincidences. These can be reduced by a factor of two by applying the L2 filter which exploits the information of the orientations of the PMTs. In parallel to this basic filtering process, dedicated triggers optimised for different event topologies like muon tracks or showers can be applied.

3.3 IceCube

IceCube [80, 96] is a neutrino detector located at the geographic South Pole, at the permanent Amudsen-Scott Pole Station, between 1450 and 2450 m below the surface of the Antarctic ice. Its construction was completed in December 2010 after six years of deployment during which partial configurations of the detector were already taking data. It consists of over 5000 PMTs spread among 86 vertical strings. With an instrumented volume of one cubic kilometer, IceCube is currently the largest neutrino detector in the world.

3.3.1 Detector layout

A schematic view of the IceCube layout is shown in Figure 3.8. The 86 vertical strings are 1 km high and hold 60 DOMs each. 78 of these strings form the primary in-ice array. They are arranged on a hexagonal grid with 125 m horizontal spacing with the DOMs separated vertically by about 17 m. The remaining eight strings, located at the centre, are arranged in a more compact configuration, with a horizontal separation of about 70 m and a vertical DOM spacing of 7 m. These eight strings form the DeepCore subdetector, which targets lower neutrino energies ($E_\nu \gtrsim 10$ GeV). On the ice surface, the IceTop array [97] detects extended particle showers induced by cosmic rays in the energy range from ∼100 TeV to 1 EeV. It consists of 81 stations arranged approximately on the same grid on which the strings of the in-ice array are located. The eight stations in the centre corresponding to the DeepCore location are placed in a denser configuration. Each station has two ice-filled tanks, separated by 10 m and equipped with downward facing DOMs. Each tank has a diameter of 1.8 m and a depth of 50 cm. While the main purpose of IceTop is to study the mass composition of primary cosmic rays, it is also used as a partial veto against the atmospheric muon background in the IceCube cosmic neutrino searches and for direction calibration.

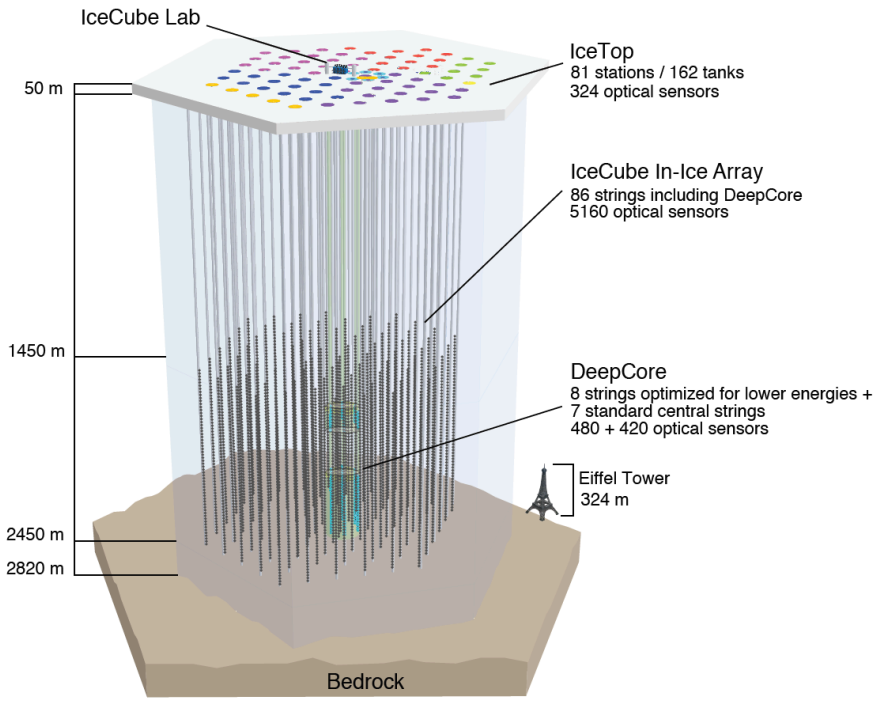

Figure 3.8: Schematic view of the IceCube detector. Figure taken from [96].

3.3.2 Ice properties

The Antarctica ice has been formed over the past 10^5 years through a process of accumulation of snow with the presence of varying amounts of particulate impurities, including ash deposited by volcanic eruptions [98]. As a result, the optical properties of the ice strongly vary with the depth. Dedicated measurements were performed to determine the properties of light propagation in the ice at the IceCube site by means of a system of LEDs located at different depths [99]. The results of the measurements in terms of values of the effective scattering and absorption coefficients as a function of the depth are shown in Figure 3.9 for a wavelength of 400 nm. While ice is more transparent than seawater at most depths, i.e. its absorption length is larger allowing for a better energy reconstruction, it suffers from stronger scattering mainly due to dust trapped into the ice. The small scattering length in ice results in a worse angular reconstruction accuracy when compared to under-water experiments. A strong layer of dust located at 2000 m under the ice surface largely increases the scattering and the absorption at this depth. Overall, the ice properties improve with increasing depth.

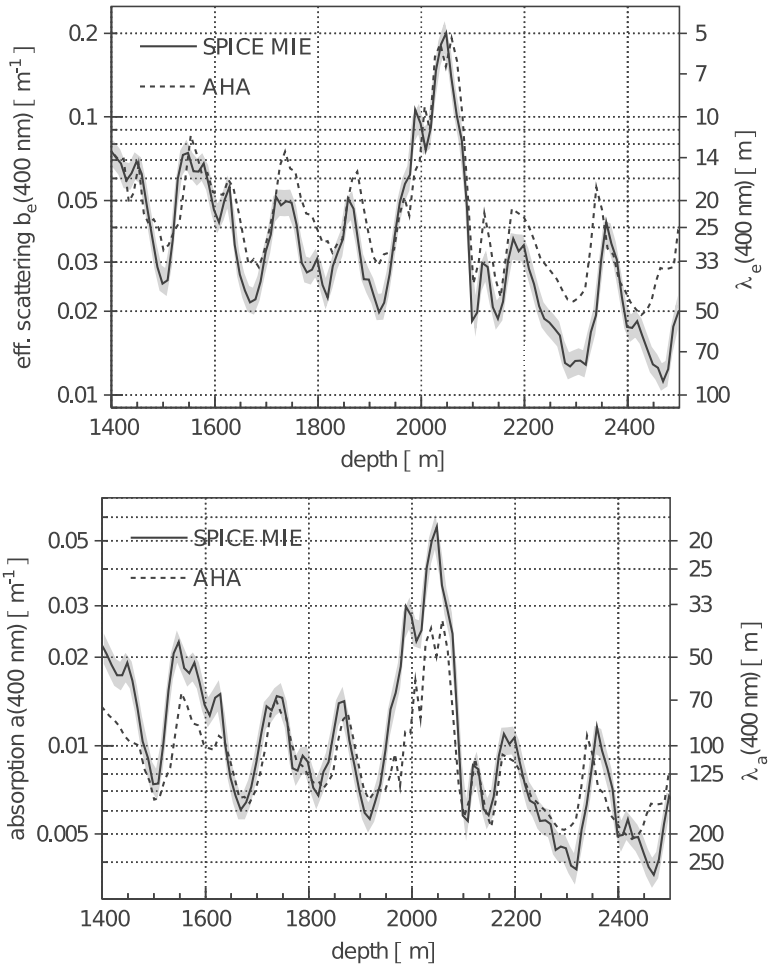

Figure 3.9: Effective scattering (top) and absorption (bottom) coefficients as a function of the depth at the IceCube location for a wavelength of 400 nm for two models of light propagation in ice (SPICE MIE and AHA). Figure taken from [99].

4

Monte Carlo simulations and event reconstruction

Monte Carlo simulations are required not only to study the performances of the neutrino telescope and check the correct functioning of the apparatus, but they are also necessary in physics analyses to optimise the selection cuts for the rejection of background events, to build the probability density functions of the relevant parameters, and to derive the detector sensitivity to a range of signal hypotheses. The output of the Monte Carlo simulations is used as an input for the event reconstruction algorithms, whose aim is to reconstruct the energy and direction of the incoming neutrino using the information of the observed light at different positions and times in the detector. By comparing the simulated quantities to the reconstructed ones, the capacity of the algorithm to reconstruct real data events is evaluated. In this Chapter, the Monte Carlo simulation chain (Section 4.1) together with the reconstruction algorithms (Section 4.2) employed in ANTARES and KM3NeT will be discussed.

4.1 Monte Carlo simulations

The Monte Carlo (MC) simulation chain in a large volume neutrino telescope can be subdivided into three main steps [100]. First, all the particles that can induce an observable signature in the telescope are generated. Second, the particle interactions with the medium are simulated and the resulting particles together with

the Cherenkov light are propagated until they reach the instrumented volume. Third, the response of the detector is determined. The Monte Carlo simulation chain together with the programs employed by ANTARES and KM3NeT in each step of the simulation are described in the following and summarised in Table 4.1.

4.1.1 Event generation

In the event generation, the instrumented detector is treated as a cylinder containing all the PMTs [101]. The geometry of the detector used in the event generation is shown in Figure 4.1. A larger cylinder, called the *can*, surrounds the first one. The distance between the surfaces of the two cylinders is of 200 m, which is about three times the longest absorption length in water. This ensures that the can contains the volume within which the vast majority of the Cherenkov light detected by the experiment is generated. Outside the can, electrically charged particles are tracked and propagated to the edge of the can. No Cherenkov light is generated and only particle energy losses are considered until they cross the boundary of the can. Inside the can, a full simulation, including the generation of Cherenkov light, is performed.

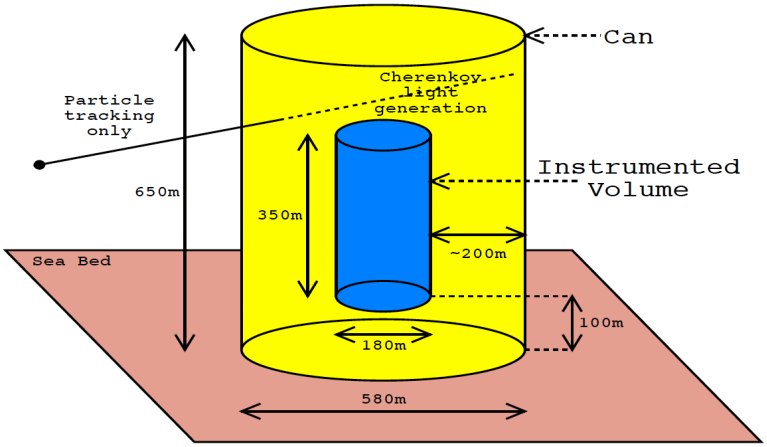

Figure 4.1: Definition of the detector geometry used in the event generation in ANTARES. A similar approach is employed in KM3NeT. Figure taken from [101].

Neutrino generation

The simulation of neutrinos of all flavours, both for CC and NC interactions, is performed using the GENHEN package [101]. The neutrino directions are generated isotropically, while the generated neutrino energy spectrum follows an $E^{-1.4}$ power-law in the $10-10^8$ GeV energy range in ANTARES and 10^2-10^8 GeV

energy range in ARCA. Neutrino interactions are only simulated inside a generation volume defined by the maximum range that a muon with the maximum generated energy can travel. The CTEQ6-D parton distribution functions [102] are used for the calculation of the cross section of the neutrino-nucleon interactions within the generation volume. For up-going neutrinos, the absorption in the Earth needs to be taken into account. The probability for a neutrino to traverse the Earth without interacting (transmission probability) depends on its energy E_ν and direction (zenith angle θ_ν). It is defined as

$$P_{\text{Earth}}(E_\nu, \theta_\nu) = e^{-N_A \sigma_\nu(E_\nu) \rho(\theta_\nu)}, \tag{4.1}$$

where $\sigma_\nu(E_\nu)$ is the interaction cross section with matter, $\rho(\theta_\nu)$ is the effective density, i.e. the mass density integrated along the neutrino trajectory, and N_A is the Avogadro number. Up-going neutrinos with higher energies and coming from more vertical directions have a smaller chance to reach the detector. A representation of the transmission probability is shown in Figure 4.2.

The same set of generated neutrino events is used for the cosmic signal and the atmospheric background. This is possible as each generated neutrino event has an associated generation weight which allows to properly re-weight the event in order to simulate neutrino fluxes with different energy spectra. The generation weight is defined as [103]

$$W_{gen} = V_{gen} \cdot t_{gen} \cdot I_\theta \cdot I_E \cdot E^\gamma \cdot \sigma(E_\nu) \cdot \rho \cdot N_A \cdot P_{\text{Earth}}, \tag{4.2}$$

where:

- V_{gen} is the generation volume;
- t_{gen} is the equivalent time of the simulation;
- I_θ, defined as $I_\theta = 2\pi(\cos\theta_{\text{max}} - \cos\theta_{\text{min}})$, where θ_{max} and θ_{min} are the maximum and minimum generated zenith angles, accounts for the fact that the simulation is performed only for part of the sky;
- I_E, defined as $I_E = \int_{E_{\text{min}}}^{E_{\text{max}}} E^\gamma dE$, where E_{min} and E_{max} are the minimum and maximum generated energies, takes into account that the simulation is performed only for limited energy ranges;

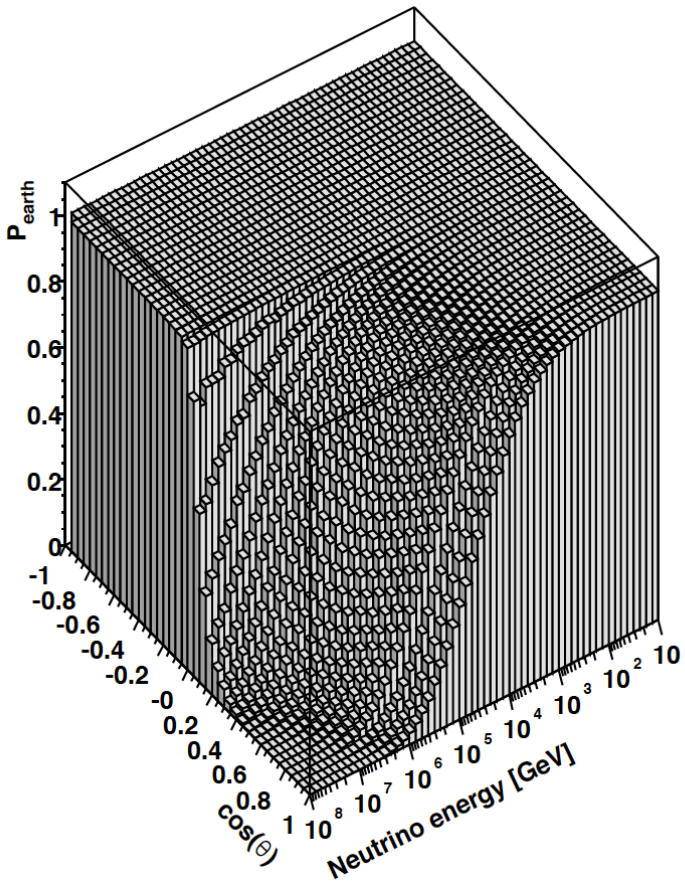

Figure 4.2: Neutrino transmission probability through the Earth as a function of the energy and zenith angle. In this plot, events with a value of $\cos\theta = 1$ are vertical up-going events. Figure taken from [101].

- γ is the spectral index of the generated neutrinos;
- $\sigma(E_\nu)$ is the neutrino-nucleon interaction cross section;
- $\rho \cdot N_A$ is total number of target nucleons per unit volume (ρ is the target density and N_A is the Avogadro number);
- P_{Earth} is the neutrino transmission probability through the Earth.

Any given neutrino flux Φ_ν can be simulated by weighting the neutrino events by the factor $W_{gen} \cdot \Phi_\nu$. For the atmospheric neutrinos, the Bartol flux [104]

is employed in ANTARES, while in KM3NeT the HONDA flux [105] with the prompt component described in [106] is used. For cosmic neutrinos, an energy spectrum proportional to E_ν^{-2} is traditionally used to account for the value predicted by the Fermi acceleration mechanism [4, 5, 107], but other energy spectra can be considered as well (see Chapter 7).

Atmospheric muon generation

A full MC simulation of the atmospheric muons, from their production in the atmosphere to their propagation down to the sea level, can be performed by means of the CORSIKA program [108]. However, while it allows for an accurate reproduction of the main features of muons at the detector level, it requires a large amount of CPU time. In ANTARES and KM3NeT, atmospheric muons are simulated using the MUPAGE [109] package. MUPAGE relies on parametric formulas which describe the flux, the angular distribution and the energy spectrum of under-water muon bundles. These formulas were obtained using as input the results of complete simulations of atmospheric muons together with the data collected by the MACRO experiment. MUPAGE simulations are valid for depths between 1.5 and 5 km water equivalent and for zenith angles between $0°$ and $85°$.

4.1.2 Particles and light propagation

Muons produced in neutrino interactions as well as atmospheric muons are propagated with the MUSIC [110] code. The propagation of the Cherenkov light induced by all the charged particles inside the can is handled by the KM3 [111] package, based on the GEANT [112] software. KM3 includes a modified version of MUSIC to propagate the muons inside the can and derive the starting points for the light propagation. All the relevant physical processes such as energy losses, multiple scattering, radiative processes and hadronic interactions are considered. Cherenkov photons are not tracked from the production site to the PMTs as it would be computationally too expensive. Instead, KM3 uses so-called photon tables, obtained in advance by fully simulating photons with GEANT, and containing the distributions of the number and arrival time of PMT hits for different distances, positions and orientations of the PMTs with respect to the track or electromagnetic shower. Light absorption and scattering are taken into account.

Table 4.1: Summary of the programs used in the various steps of the Monte Carlo simulation chain in ANTARES and KM3NeT.

	Program	
Simulation step	ANTARES	KM3NeT
Neutrino generation	GENHEN	GENHEN
Atmospheric muon generation	MUPAGE	MUPAGE
Particle propagation	MUSIC	MUSIC
Cherenkov light propagation	KM3	KM3
Detector response	TriggerEfficiency	JTriggerEfficiency

4.1.3 Detector response

In ANTARES and KM3NeT, the detector response to the photons provided by KM3 is simulated with the TriggerEfficiency [113] and JTriggerEfficiency [114] programs, respectively, which also add the optical background hits and simulate the electronics and the trigger algorithms. In ANTARES, the hits due to optical background are generated according to a Poisson probability distribution based on measured rates in the detector in order to properly reproduce the actual data taking conditions.

The electronics response is simulated by summing the number of photons detected during the integration time of the ARS chip ($\sim$35 ns). In the simulation, two ARS chips for every PMT and the ARS dead time of 250 ns are considered. The time resolution for single photoelectron signals, dominated by the Transit Time Spread (TTS) of the PMTs, is 1.3 ns for ANTARES and decreases in case of multiple photoelecrons. To simulate this effect, the hit times are smeared using a Gaussian function with a width of $\sigma = 1.3\ \mathrm{ns}/\sqrt{\mathrm{N}_\gamma}$, where N_γ is the number of photons detected simultaneously. The uncertainty on the charge reconstruction is simulated by smearing the number of arriving photons with a Gaussian with a width of 0.3 p.e. At this point, the triggers described in Chapter 3 are implemented in the simulation.

Finally, TriggerEfficiency and JTriggerEfficiency produce event files that can be used as an input for the reconstruction algorithms as a last step of the simulation chain.

4.2 Event reconstruction

Several event reconstruction algorithms have been developed within the ANTARES and KM3NeT experiments. Those used in the point-like and extended source searches presented in Chapter 7 are described in this section. In ANTARES, tracks and showers are reconstructed using the algorithms that achieve the best angular resolution: the AAFit [115] and the TANTRA [116, 117] algorithms, respectively. Some parameters provided by an alternative shower reconstruction algorithm, Dusj [118, 119, 120], originally developed for diffuse searches and characterised by a worse angular resolution compared to TANTRA, are also employed in the event selection chain. As for KM3NeT tracks, the most recent track reconstruction algorithm developed within KM3NeT, JGandalf [121], is employed.

4.2.1 Tracks in ANTARES: AAFit

Fully describing a muon track means determining the position and the direction of the muon at a given time. The AAFit algorithm fits the muon trajectory using the information of the arrival times and the amplitudes of the hits detected by the OMs. A schematic representation of a muon track is shown in Figure 4.3. For a given muon position and direction at an arbitrary time t_0, the expected arrival time t^{th} of a Cherenkov photon to an OM is given by

$$t^{th} = t_0 + \frac{1}{c}\left(l - \frac{k}{\tan\theta_c}\right) + \frac{1}{v_g}\left(\frac{k}{\sin\theta_c}\right), \tag{4.3}$$

where v_g is the group velocity of light, θ_c is the Cherenkov angle, and k is the shortest distance between the track and the OM. The difference between t^{th} and the measured arrival time of the photon is called time residual.

AAFit reconstructs the muon track in four distinct steps given by three consecutive pre-fits (linear pre-fit, M-estimator pre-fit and maximum-likelihood pre-fit) and a final maximum-likelihood fit. The objective of the three pre-fits is to provide a good approximation of the final best-fit parameters in order to ensure the optimal reconstruction performances of the final maximum-likelihood fit.

The reconstruction chain starts by pre-selecting those hits fulfilling a similar requirement as the L1 trigger (described in Chapter 3) and satisfying the condition $|\Delta t| \leq \frac{d}{v_g} + 100$ ns, where Δt is the time difference between a hit and the hit with

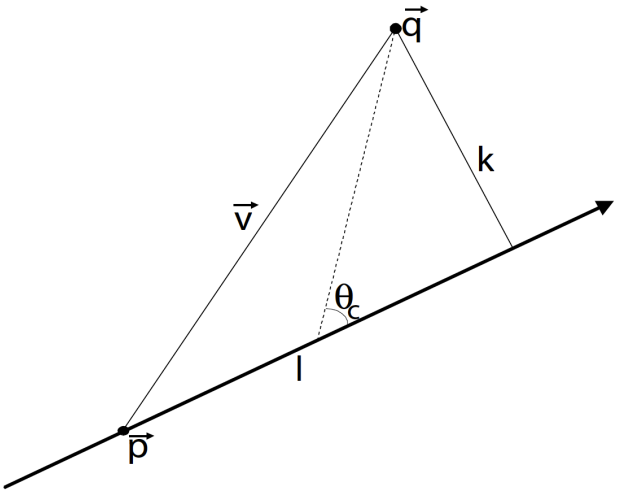

Figure 4.3: Schematic view of a muon track. The parameters used in the AAfit reconstruction are shown. The Cherenkov light is emitted along the track at an angle θ_c with respect to the muon trajectory (represented by the arrow) and is detected by an OM at the position $\vec{q}$, at a distance k from the track. Figure taken from [115].

the largest amplitude of the sample, and d is the distance between the two OMs which detected the two hits. The linear pre-fit is performed assuming that the muon track passes through the positions of the selected hits. The best track parameters are derived by means of a χ^2 minimisation.

The following step makes use of the result of the linear pre-fit as input for the M-estimator fit. Only hits closer than 100 m to the track and whose time residuals lie within a 150 ns time window, or alternatively, hits with an amplitude above 2.3 p.e. are selected for this step. The M-estimator is defined as

$$M = \sum_i k(-2\sqrt{1 + A_i t_{\mathrm{res},i}^2/2}) - (1-k) f_{\mathrm{ang}}(a_i), \tag{4.4}$$

with A_i, the charge of the $i-$th hit, being used as weight for the time residual $t_{\mathrm{res},i}$, and $f_{\mathrm{ang}}(a_i)$ being a term which contains the angular response of the OM, function of the cosine of the incident angle of the photon a_i. The relative weights of the two terms are determined by the constant k, whose value, set to 0.05, was optimised using simulations.

After the M-estimator, a maximum-likelihood pre-fit is performed using only hits with amplitude above 2.5 p.e. or a time residual within $[-R/2, R]$, with R being the root-mean-square of the hit time residuals of all hits used in the

M-estimator fit. In this step, the likelihood makes use only of the probability density functions (PDFs) of the time residuals derived from simulations. The M-estimator pre-fit and the maximum-likelihood pre-fit are repeated nine times using different starting directions.

The last step is a maximum-likelihood fit with improved likelihood PDFs which also take into account the hit charges and the background contribution. For this step, all hits with a time residual between -250 and +250 ns and with a charge larger than 2.5 p.e. , or in local coincidences, i.e. two or more hits on one floor within 25 ns, are selected.

The goodness of the reconstruction is given by the Λ quality parameter,

$$\Lambda = \frac{\log L^{\max}}{N_{\text{dof}}} + 0.1(N_{\text{comp}} - 1), \tag{4.5}$$

where $L^{\max}$ is the maximum value of the likelihood, N_{dof} is the number of degrees of freedom of the fit given by $N_{\text{dof}} = N_{\text{hits}} - 5$, with N_{hits} being the number oh hits used in the reconstruction, and N_{comp} is the number of repetitions of the M-estimator and the maximum-likelihood pre-fits which provided a track direction within 1° from the best-fit one.

The track angular error estimate, β, can be calculated from the error matrix of the final fit, which yields the errors on the zenith angle β_θ, and on the azimuth angle β_ϕ, as

$$\beta = \sqrt{\beta_\theta^2 + \sin^2\theta\beta_\phi^2}. \tag{4.6}$$

The information of the selected hits used in the last step of the track reconstruction is employed by the dEdX energy reconstruction method [122, 123]. The method provides a proxy for the muon energy based on an energy estimator ρ which computes the muon energy deposition per unit path length,

$$\rho = \frac{\sum_i^{N_{\text{hits}}} Q_i}{\epsilon(\vec{x})} \frac{1}{L_\mu}, \tag{4.7}$$

where Q_i is the measured charge of the i-th hit, $\epsilon(\vec{x})$ is the light detection efficiency of the OMs that were active at the time the event was recorded, and L_μ is the

length of the reconstructed muon within a volume given by the cylinder of the ANTARES instrumented volume extended by twice the light attenuation length.

Figure 4.5-top-left shows the AAFit median angular resolution for events coming from ν_μCC interactions and selected with the track selection cuts described in Chapter 7. A median angular resolution better than 0.4° is achieved for energies above 10 TeV. Figure 4.5-top-right shows the correlation between the ρ energy estimator and the original neutrino energy for the same events.

4.2.2 Showers in ANTARES: TANTRA and Dusj

TANTRA. The TANTRA algorithm reconstructs the shower vertex position and the shower direction in two steps. In order to derive the shower position, a pre-selection is applied to remove those hits induced by optical background. Pairs of hits compatible with being caused by a common source are selected by applying the causality criterion,

$$|\vec{r_i} - \vec{r_j}| \geq c_w \cdot |t_i - t_j|, \tag{4.8}$$

where $\vec{r_i}$ is the position of the PMT that recorded the hit i, t_i is the time of the hit i and c_w is the speed of light in water. A first estimation of the shower position $\vec{r}_{\text{shower}}$ and the time t_{shower} can be determined by performing a least square fit to solve the following system of quadratic equations:

$$(\vec{r_i} - \vec{r}_{\text{shower}})^2 = c_w^2 \cdot (t_i - t_{\text{shower}})^2 \,, \tag{4.9}$$

where i is the index of any of the selected hits which are assumed to come from the same interaction vertex. Subsequently, these pre-fit values are used as input to determine the final parameters of the shower by means of an M-estimator defined as

$$M_{\text{est}} = \sum_{i=1}^{N} (q_i \cdot \sqrt{1 + t_{\text{res},i}^2/2}) \,, \tag{4.10}$$

with q_i being the charge of the hit i and $t_{\text{res},i} = t_i - t_{\text{shower}} - |\vec{r_i} - \vec{r}_{\text{shower}}|/c_w$ the time residual of hit i.

A second hit selection is applied to determine the shower direction. For this step, all the hits on a given PMT in a time residual window of $-200 < t_{res}/\text{ns} < 500$ with respect to the position fitted in the previous step are considered. The sum of the charges of all the selected hits and the time of the first hit are taken as the charge and the time, respectively, of the combined hit. The shower direction is determined by performing a maximum-likelihood fit. Figure 4.4 shows a schematic view of the variables used in the fit.

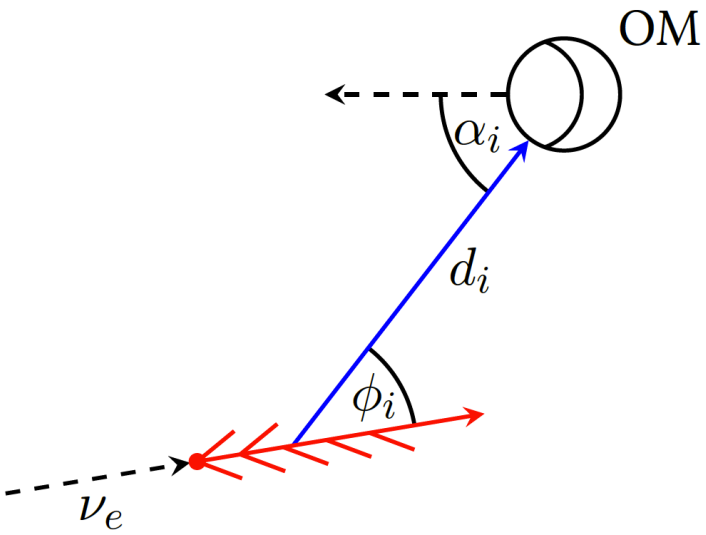

Figure 4.4: Schematic view of the variables used in the likelihood fit of the shower TANTRA reconstruction algorithm. Figure taken from [116].

The likelihood is defined as

$$L = \sum_{i=1}^{N_{\text{selected hits}}} \log\{P_{q>0}(q_i|E_\nu, d_i, \phi_i, \alpha_i) + P_{\text{bg}}(q_i)\} + \\ + \sum_{i=1}^{N_{\text{unhit PMTs}}} \log\{P_{q=0}(E_\nu, d_i, \phi_i, \alpha_i)\}\,, \tag{4.11}$$

where $P_{q>0}(q_i|E_\nu, d_i, \phi_i, \alpha_i)$ is the probability that the charge q_i measured by the PMT is produced by a photon coming from a distance d_i, emitted at an angle ϕ_i from the shower direction, striking the PMT with an incident angle α_i, and that the incoming neutrino energy is E_ν. The likelihood also takes into account the probability that the charge q_i is caused by a background event, $P_{\text{bg}}(q_i)$, and the probability of not detecting the charge, $P_{q=0}$.

The TANTRA median angular resolution for events coming from ν_eCC interactions and selected with the shower selection cuts described in Chapter 7 is

shown in Figure 4.5-bottom. A median angular resolution between 2° and 4° is obtained for energies between 10^3 and 10^6 GeV. The localised distribution of light close to the neutrino interaction point for the showers allows for a good median energy resolution (better than 10% [117]).

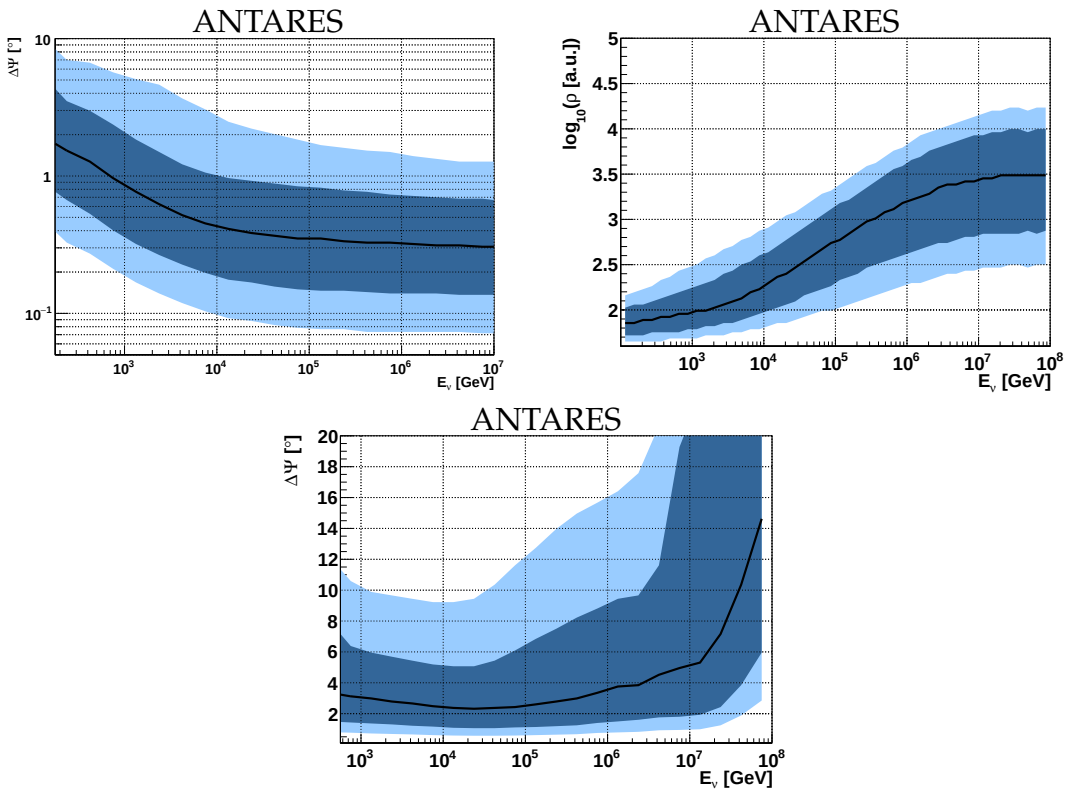

Figure 4.5: Top left: AAFit median angular resolution for events coming from ν_μCC interactions. Top right: correlation between the energy estimator ρ and the original neutrino energy for events coming from ν_μCC interactions. In both cases the track selection cuts described in Chapter 7 are applied. Bottom: TANTRA median angular resolution for events coming from ν_eCC interactions. The shower selection cuts described in Chapter 7 are applied. In all figures the coloured bands represent the 68% and 90% quantiles. Figures taken from [90].

Dusj. The reconstruction of the shower is performed in Dusj through various steps including a hit selection, a χ^2 fit and a maximum-likelihood fit. The algorithm also provides a set of quality parameters, some of which are used as input features for the training of a random decision forest (RDF) in ANTARES.

As the PDF tables used in the likelihood fit were build from a Monte Carlo simulation which does not take into account photon scattering, the first step of the reconstruction method consists in selecting hits that are caused by direct photons in order to ensure the reliability of the algorithm. Therefore, only hits registered by the first active ARS in each OM are kept. A further selection rejects

hits from optical background by keeping only coincident hits (detected within a time window of 20 ns) with a charge higher than 1.2 p.e. Subsequently, a pre-fit of the interaction time and vertex position is performed. This pre-fit is based on the minimisation of a reduced χ^2, defined as

$$\chi^2_{\text{reduced}} = \frac{\sum_{i=1}^{N_{\text{hits}}} t^2_{\text{res},i}}{N_{\text{hits}} - 4}, \tag{4.12}$$

where $t_{\text{res},i}$ is the time residual for a given hit and $N_{\text{hits}} - 4$ is the degrees of freedom of the fit. The subset of hits which are best compatible with being originated from a shower described by the best-fit interaction time and vertex position (*shower hits*) are kept for the next step of the reconstruction.

Starting from the results of the pre-fit, the parameters of the shower are determined with two consecutive maximum-likelihood fits. The first fit provides the position and the time of the shower. The second fit determines the direction and the energy of the incoming neutrino by fixing the start time and position of the shower to the values provided by the first fit. In both fits, the likelihood for the selected shower hits to come from a certain shower hypothesis is calculated as $LH = \prod_{i=1}^{N_{\text{hits}}} p_i$, with p_i being the probability for the single hit to come from such a shower, estimated using PDF tables generated in advance from Monte Carlo simulations. The value of the reduced log-likelihood, i.e. the value of the final log-likelihood divided by the degrees of freedom, $LLH_{\text{red}} = \frac{\log LH}{N_{\text{dof}}}$, gives a measure of the quality of the fit.

A subset of five quality parameters provided by the Dusj reconstruction chain is used as input in a RDF classification employed to suppress the atmospheric muon background in ANTARES analyses. The five parameters are:

- the χ^2_{reduced} defined in Equation 4.12;
- the reduced log-likelihood value of the first maximum-likelihood fit;
- the reduced log-likelihood value of the second maximum-likelihood fit;
- the χ^2 of time residuals of the shower hits with respect to the final vertex reconstruction result, defined as $\chi^2 = \frac{1}{N_{\text{hits}}} \sum_{i=1}^{N_{\text{hits}}} t^2_{\text{res},i}$;
- the quadrupole moment of the shower, that is a measure of the spatial distribution of the hits with respect to the fitted direction.

4.2.3 Tracks in KM3NeT: JGandalf

As in AAFit, the JGandalf reconstruction chain starts with a linear pre-fit based on a χ^2 minimisation. Causally related hits are first selected in order to remove the optical background contribution. A subset of the selected hits is used in the linear pre-fit which is applied on all permutations of the hits in the subset. This procedure is repeated for all the possible track directions with a scanning angle of 1° and provides a set of 12 best-fit track directions, where the goodness of the fit is given by the parameter Q defined as

$$Q = NDF - 0.25 \times \frac{\chi^2}{NDF}\,, \tag{4.13}$$

with NDF representing the degrees of freedom of the fit. The 12 best-fit directions are used as starting points for the muon trajectory fit based on a likelihood maximisation in which all the parameters of the track are fitted simultaneously. The likelihood function makes use of PDFs which describe the response of the PMTs as a function of the minimum distance of the muon to the PMT, ρ, the orientation of the PMT, θ and ϕ, and the time residual of the hit, t_{res}, and is defined as

$$L = \prod_{\mathrm{hits}} \left[\frac{\partial P}{\partial t}(\rho_i, \theta_i, \phi_i, t_{\mathrm{res}}) \right] . \tag{4.14}$$

These PDFs are derived semi-analytically from simulations, account for unscattered and single-scattered photons both from Cherenkov effect and from muon energy losses, and include the optical background, the dispersion of light and the characteristics of the PMTs.

A median angular resolution better than 0.1° for track-like events reconstructed with JGandalf is achieved for energies above 100 TeV, as shown in Figure 4.6.

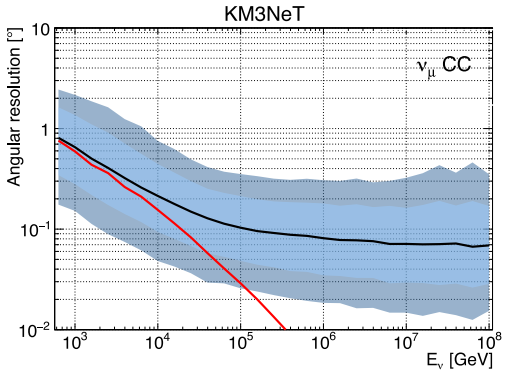

Figure 4.6: JGandalf median angular resolution for track events coming from ν_μCC interactions. The coloured bands represent the 68% and 90% quantiles. The red line depicts the median angle between the true neutrino and muon directions. Figure taken from [121].

5 Time calibration in ANTARES

The reconstruction of the ANTARES events is based on the measurement of the arrival times of the Cherenkov photons at the PMTs (see Chapter 4). The accuracy in the determination of the arrival times is closely linked to the best achievable angular resolution, which in turn is the key factor for the identification of point-like sources of cosmic neutrinos. In this Chapter, the various time calibration methods employed in ANTARES are described. In particular, the time calibration with ^{40}K and atmospheric muons performed within this thesis is presented in Section 5.3.

5.1 Time calibration methods

An angular resolution better than 0.3° is achieved in ANTARES for track-like events with energies above 10 TeV. This good pointing capability requires an accuracy in the relative time calibration among PMTs of $\sim$1 ns. Two main unavoidable sources of uncertainty limit the accuracy in the relative time calibration: the transit time spread (TTS) of the signal in the PMTs and the optical properties of the seawater such as light scattering and chromatic dispersion. The first effect contributes with an uncertainty of $\sigma_{\mathrm{TTS}} \approx 1.3$ ns [124]. The latter induces an uncertainty of $\sigma_{\mathrm{water}} \approx 1.5$ ns for Cherenkov photons produced at a distance of 40 m from the PMT [101]. An additional source of uncertainty, σ_e, comes from the electronic jitter and can be estimated with the time calibration methods

presented in this Section. Overall, the global uncertainty in the relative time calibration can be expressed as [125]

$$\sigma^2 = \frac{\sigma^2_{\mathrm{TTS}}}{N_{\mathrm{pe}}} + \frac{\sigma^2_{\mathrm{water}}}{N_\gamma} + \sigma^2_e \,, \tag{5.1}$$

where N_{pe} is the number of photoelectrons produced in the PMT and N_γ is the number of detected Cherenkov photons. Assuming both N_{pe} and N_γ to be $\gg 1$, the electronics is required to contribute less than 0.5 ns to the overall timing uncertainty in order to obtain the desired angular resolution. Various procedures and systems are employed for the calibration of the relative timing (time-offset calibration) among ANTARES elements (ARS/storey/line). Before the deployment of the lines, an onshore calibration is performed in a dedicated dark-room (Section 5.1.2). Once in the sea, the calibration is performed using an echo-based clock calibration system to synchronise all the electronics boards (Section 5.1.1), and other in-situ calibration methods to synchronise the signal travel time between the front-end electronics and the PMT photo-cathode. (Section 5.1.3).

Apart from the calibration of the relative timing, an absolute time calibration, i.e. the detector's time synchronization with the Coordinated Universal Time (UTC), is necessary. The absolute timing is relevant for determining possible correlations of the ANTARES events with astrophysical sources. The absolute time stamping is performed by interfacing the clock system with a dedicated electronic board to the GPS timing system (Section 5.1.1).

5.1.1 The clock system

The time synchronization of the ANTARES OMs among each other and with respect to the UTC is achieved by means of the clock system [125]. The layout of the ANTARES clock system is shown in Figure 5.1. The relative time synchronization is performed by means of an echo-based time calibration. The master clock on shore sends infrared signals of 1534 nm wavelength at a frequency of 20 MHz to the SCM of each line, which in turn sends infrared signals of 1550 nm wavelength to the LCMs of the same line. Each LCMs sends back a 1320 nm signal to the SCM of the corresponding line and a 1549 nm signal is then sent to shore. Half of the round-trip time gives the propagation time through the electronic path needed to reach each LCM. In order to account for this delay, measurements of the round-trip times are taken every hour and corrections are applied accordingly.

Figures 5.2 and 5.3 show the measurements of the shore-to-SCM round-trip time and of the SCM-to-LCM round-trip time taken over a period of about three months. The main variation in the time delays is of the order of a few hundreds of picoseconds and is observed in the shore-to-SCM round-trip.

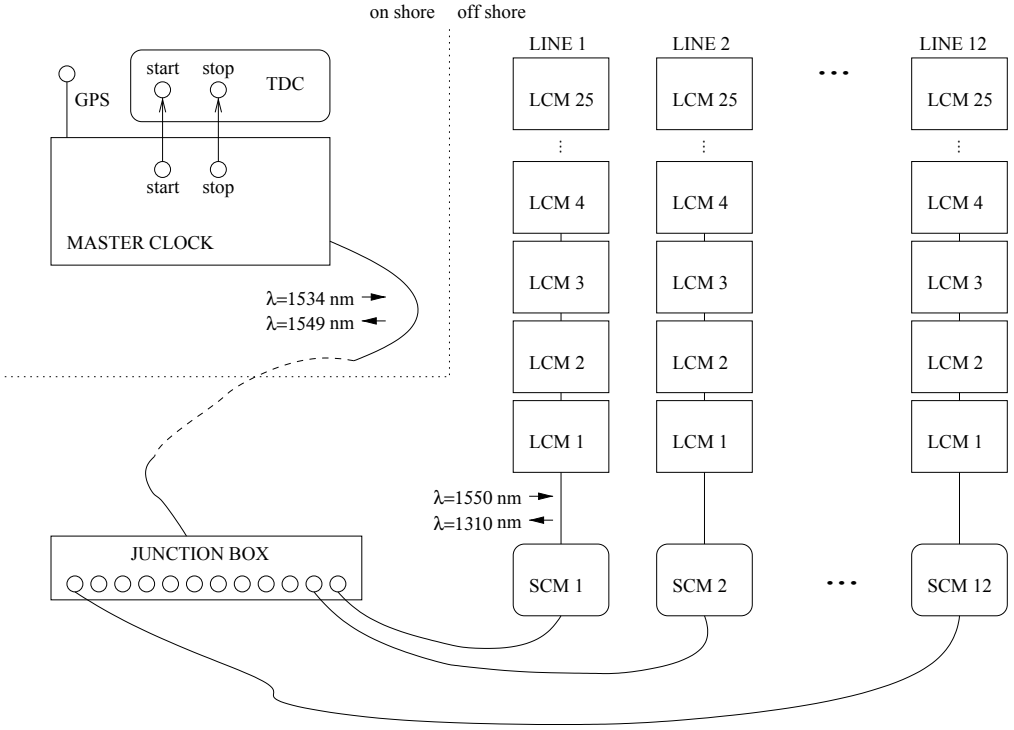

Figure 5.1: Schematic view of the ANTARES clock system. Figure taken from [125].

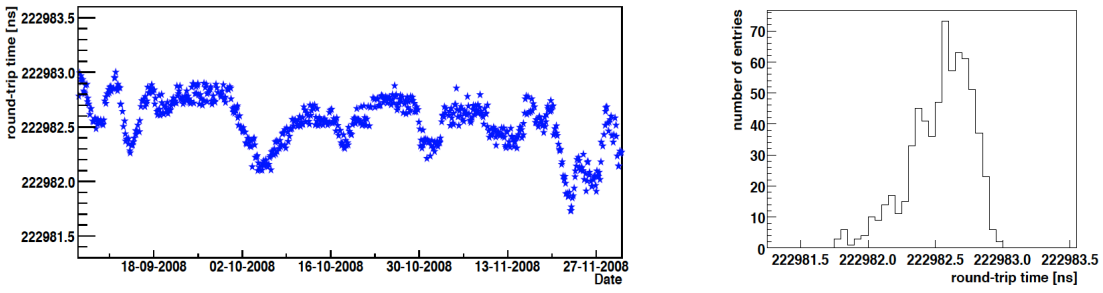

Figure 5.2: Left: Measurements of the round-trip time of a clock signal from the onshore station to an SCM over a period of about three months. Right: Corresponding distribution of the round-trip times for the same period. Figures taken from [125].

As already mentioned, an additional task of the clock system is the absolute time calibration. As shown in Figure 5.1, the master clock is connected to a GPS timing system responsible for the absolute time stamping of the signal. The procedure allows to achieve a time synchronization with the UTC at the level of ∼100 ns. This accuracy is well within the requirements for neutrino

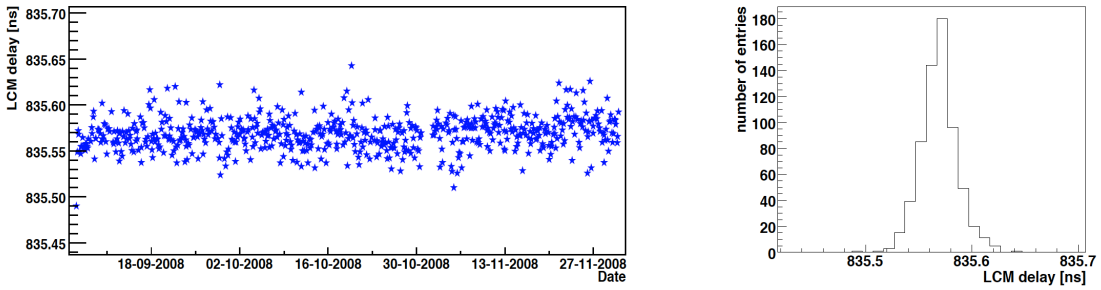

Figure 5.3: Left: Measurements of the round-trip time of a clock signal from an SCM to an LCM on the same line over a period of about three months. Right: Corresponding distribution of the round-trip times for the same period. Figures taken from [125].

astronomy. Indeed, a precision of the order of seconds (milliseconds) is sufficient to correlate the reconstructed neutrino directions with steady point sources (transient astrophysical events).

5.1.2 Onshore time-offset calibration

Prior to the deployment of each line, a full time-offset calibration was performed onshore [125]. The setup used for the calibration is presented in Figure 5.4. The procedure consisted in simultaneously illuminating groups of OMs by means of a Nd-YAG laser emitting green light ($\lambda = 532$ nm) in short (FWHM $\simeq 0.8$ ns) and intense ($E = 1$ μJ) pulses at a frequency of 1 kHz. The calibration was performed in a dark room for bunches of five storeys. The light from the laser was directed to the 15 OMs through optical fibres after being split by means of a beam splitter. The arrival time of the light to the ARSs was used to measure the relative time offsets among ARSs.

5.1.3 In-situ time-offset calibration

The onshore time-offset calibration (Section 5.1.2) only allows to determine the time offsets among ARSs in the same line (intra-line calibration). In order to derive the time offsets among different lines (inter-line calibration), other calibration methods, described in the following, need to be carried out once the line has been deployed. The in-situ calibration is also necessary after the re-tuning of the HV applied to the PMTs or after new lines are connected since they are likely to cause a miscalibration of the detector elements. An overview of the in-situ time-offset calibration methods employed in ANTARES follows.

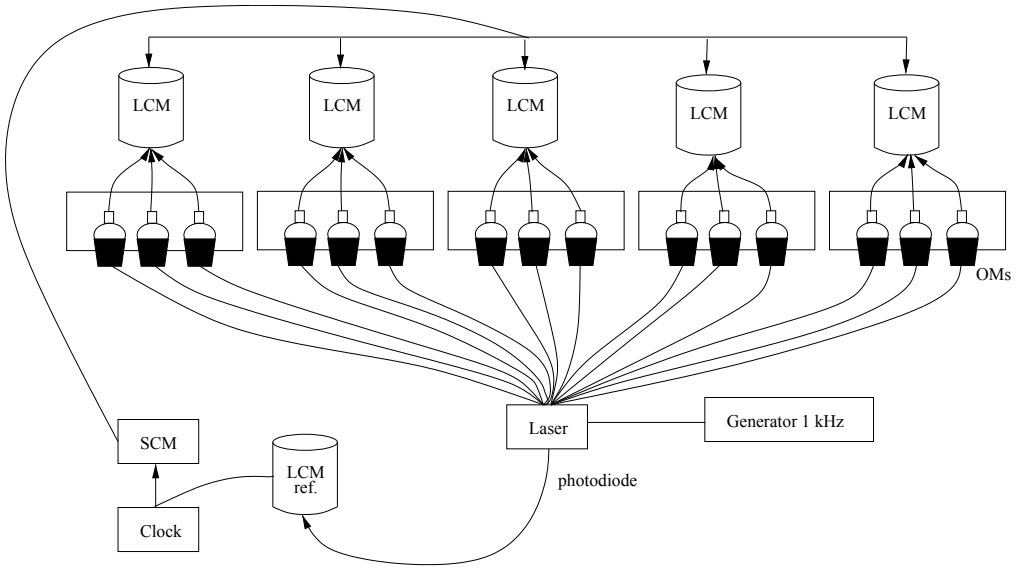

Figure 5.4: Schematic view of the experimental setup used for the onshore time-offset calibration. Figure taken from [125].

LED and laser optical beacon calibration

Analogously to the onshore time-offset calibration, the optical beacon calibration method consists in illuminating the OMs with pulsed light [126]. The optical beacon system comprises two kinds of complementary light emitters: LED and laser optical beacons. The LED optical beacons (OB) are employed for the intra-line calibration. Each OB comprises 36 LEDs emitting blue light ($\lambda = 470$ nm), of intensity 160 pJ in pulses of 4 ns width (FWHM). Each ANTARES line is equipped with four LED OBs, located in storeys 2, 9, 15 and 21 (counting from bottom to top), since each LED OB can illuminate distances up to eight floors above. The storey placed right above the OB cannot be calibrated due to light saturation. Moreover, this calibration cannot be used for the first three storeys of each line as they lie below or right above the lowest LED OB. For these storeys, the calibration with laser optical beacons (LOBs) is employed. Two of the ANTARES lines are equipped with a LOB containing a Nd-YAG laser which emits green light ($\lambda = 532$ nm), in high intensity ($\sim$1 μJ) and short (< 1 ns) pulses. Being much more powerful than the LED OBs, the LOBs can illuminate all detector lines and are used for the inter-line calibration. Both the LED and the laser OB calibrations require dedicated runs which interrupt the physics data-taking. Currently, one 5-10 minutes-long run per week is taken for the LOB calibration, and a 5-10 minutes run per line every two months for the LED OB calibration.

^{40}K calibration

The radioactive decay of ^{40}K present in seawater is used to estimate the time offsets among OMs (ARSs) in the same storey (intra-storey calibration) [127, 128]. If the β-decay of ^{40}K occurs within a few meters from a storey, the Cherenkov light induced by the electron emitted in the decay can illuminate two OMs of the storey in coincidence. An example of distribution of the measured time differences between coincidence hits, i.e. hits detected within 50 ns, in two OMs of the same storey is shown in Figure 5.5. The distribution is characterised by a Gaussian peak in the center due to photons produced in the same ^{40}K decay, on top of a flat background due to non-correlated ^{40}K events. Although the ^{40}K method can only be employed for the intra-storey calibration, it presents two main advantages: it is model-independent and does not require dedicated runs, allowing for a continuous data-taking.

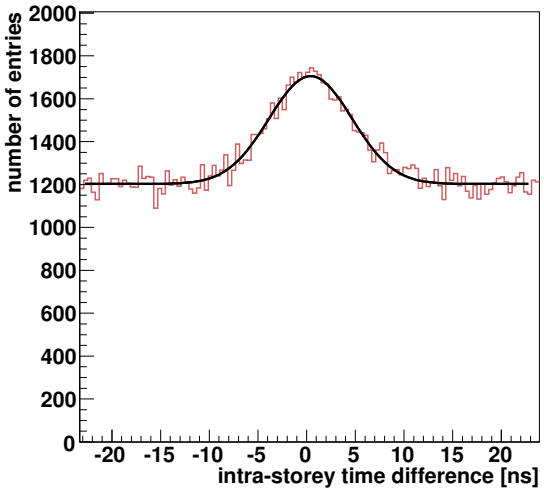

Figure 5.5: Distribution of time differences between hits recorded by two OMs in the same storey with 50 ns. Figure taken from [125].

Atmospheric-muon calibration

The rate of triggered atmospheric muons in ANTARES ranges between 1 and 10 Hz. The time-offset calibration with atmospheric muons consists in reconstructing the muon track using all the recorded hits except those detected by the element (ARS/storey/line) that is being calibrated. The time difference between the expected hit times derived from the reconstruction and the actual ones is used to calculate the time offsets. Further details on this procedure are given in Section 5.3. The main advantage of this method is that it can be used to calibrate

all the detector elements, including the sectors that cannot be calibrated with the LED OBs, and that no interruption of the data-taking is needed. On the other hand, it requires a large statistics (at least one week of data), making it necessary to use the OB method for immediate recalibration of the detector in case of high-voltage tuning or line deployments.

5.2 Effects of the front-end electronics

Limitations of the electronics used to process the analogue signals in ANTARES influence the hit time measurements. A description of the most relevant effects is given in this Section.

Walk effect

The 0.3 p.e. threshold imposed on the recorded PMT signal leads to the so-called *walk effect* [125]: hits with higher detected charge cross the threshold earlier than hits with lower charge. A schematic view of the walk effect is shown in Figure 5.6-left, while Figure 5.6-right presents the magnitude of the walk effect as a function of the pulse amplitude. The time delay between hits with different amplitudes can be of the order of a few nanoseconds.

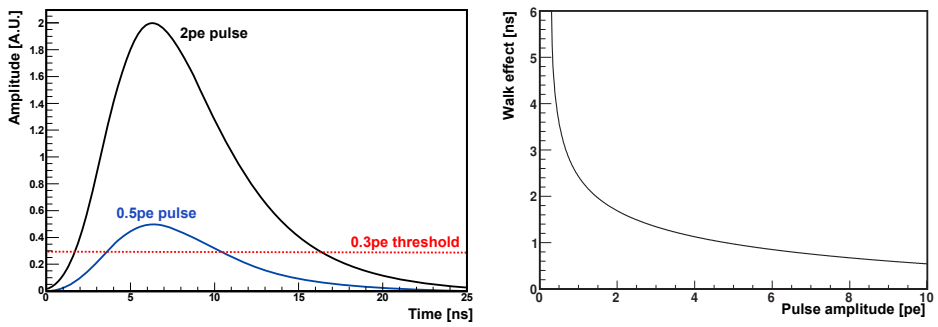

Figure 5.6: Left: Schematic view of the walk effect. Right: Magnitude of the walk effect as a function of the pulse amplitude. Figures taken from [71].

Early-photon effect

The *early-photon effect* [125] is a consequence of the inability of the PMTs to resolve multiple photons arriving very close in time. This effect becomes relevant

during the LED OB calibration when short and high intensity light flashes are emitted and only the time of the first photons is recorded. The early-photon effect, which is further emphasized by the walk effect, has a linear dependence with the distance between the light source and the illuminated PMT [125]. PMTs closer to the OB, which detect a higher amount of photons, tend to be triggered by photons emitted earlier in the flash, while for the PMTs further away from the light source the probability distribution of the measured time of the signal is determined by the pulse width.

Token-ring effect

As mentioned in Section 3.1.3, every pair of ARSs associated to a PMT works in a token-ring configuration. After the PMT receives a hit, one of the two ARSs collects the hit charge for 40 ns. When the integration time of the first ARS finishes, the second ARS becomes active with a delay of 10 to 20 ns and waits for the next hit from the PMT. In case there is still a signal present after the first integration, the second ARS continues the signal integration and the tail of the signal is processed as a new hit. This results in a second peak in the time-delay distribution 40 ns after the primary peak.

DNL effect

The TVCs (introduced in Section 3.1.3) that record the incident time of the hits contain 256 channels each. As the channels are not equally large, a uniform time signal does not produce a uniform response in the TVCs, as it is shown in Figure 5.7-left. This effect is known as the *Differential-non-linearities* (DNL) effect. It leads to an error in the TVC measurement of $\sim$0.3 ns which can be reduced to 0.09 ns by means of corrections. As shown in Figure 5.7-right, the DNL effect produces multiple peaks in the time distributions of the hits used for the calibration. Each peak corresponds to one of the comparably wide channels of the TVC in question.

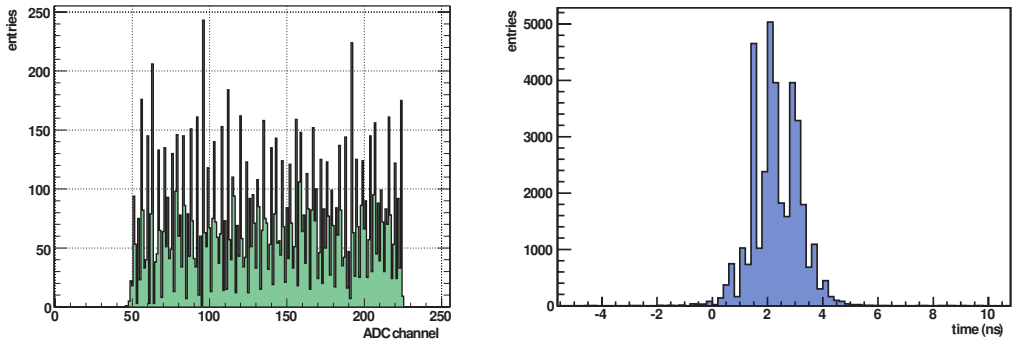

Figure 5.7: Left: Response of the 256 channels of a TVC to a uniform signal. Right: Example of the multiple peaks produced by the DNL effect observed in a time distribution of the hits recorded by an ARS. Figures taken from [71].

5.3 Time-offset calibration with ^{40}K and atmospheric muons

The time-offset calibration with ^{40}K and atmospheric muons is a novel method recently developed within ANTARES [90]. It allows to obtain an increase in the number of well-reconstructed events with respect to the previously employed calibration method. The new procedure combines two of the calibration procedures described in Section 5.1.3 and is divided in three steps:

- Inter-line calibration with atmospheric muons: the time offsets among lines are calculated using the atmospheric-muon calibration method;
- Intra-storey calibration with ^{40}K events: the time offsets among ARSs in the same storey are derived using the ^{40}K calibration method;
- Inter-storey calibration with atmospheric muons: the time offsets among storeys are obtained by means of the atmospheric-muon calibration method, using as input the output of the previous two steps.

The values of the time offsets are calculated in steps of one month. However, since right after a high-voltage tuning or the connection of a line, new calibrations are needed, the length of some of the calibration periods may vary according to current requirements. An amount of data runs in each calibration period is selected so that the sum of their livetimes corresponds to about one week. The run selection is based on the same quality criteria as in physics analyses. A detailed description of the three steps follows.

5.3.1 Inter-line calibration with atmospheric muons

From the selected runs, only events with a value of the AAFit quality parameter $\Lambda > -6.0$ are employed in the inter-line calibration with atmospheric muons. For each event, the hits recorded by a random line are excluded, and the event is reconstructed using only the hits detected by the other lines, providing the values of the expected hit times. The time differences between the detected and the expected hit times give the time residuals for the considered line. As an example, Figure 5.8-left shows the distribution of the time residuals for line 7 using runs recorded in July 2017. As shown in the same Figure, a Gaussian fit is performed around the peak of the distribution, and the mean value for each line l, $t_{l,\text{fit}}$, is stored. The correction for each line is then defined as $t_{l,\text{corr}} = t_{l,\text{fit}} - \bar{t}_{\text{fit}}$, with $\bar{t}_{\text{fit}}$ being the average of the mean values. This procedure is repeated for several iterations until a convergence is reached. In each iteration, the corrections derived in the previous one are applied. At each iteration i, the convergence is evaluated on the basis of the following variables:

- the average time correction for a given line using all the iterations performed before the iteration i, $t_{l,i,\text{avg}}$;
- the standard deviation of the difference between $t_{l,i,\text{avg}}$ and $t_{l,\text{corr}}$, $\sigma_{\Delta T}$.

The process stops when a value of $\sigma_{\Delta T} \leq 0.4$ ns is reached, and the corrections derived in the last iterations are stored and will be used in the third step of the calibration procedure (see Section 5.3.3). As an example, Figure 5.8-right shows the evolution of $\sigma_{\Delta T}$ as a function of the iteration for the runs of July 2017 and Figure 5.9 shows the time-offsets evolution for each line in the same period. The results of the inter-line time offsets calculated for each active line between the beginning of 2017 and the end of 2018 are shown in Figures 5.10, 5.11, and 5.12. Each point corresponds to the time offset obtained in the last iteration. The horizontal dashed line shows the mean value of the time offsets averaged over a year. The variation in the mean value that can be observed at the beginning of 2018 for some of the lines is due to the reconnection of Line 6.

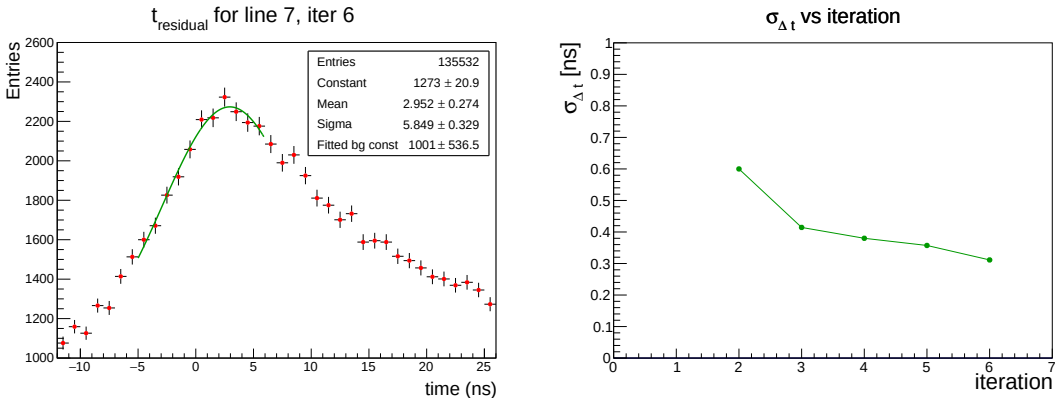

Figure 5.8: Left: Distribution of the time residuals and Gaussian fit for line 7 using runs recorded in July 2017. Right: Evolution of $\sigma_{\Delta T}$ as a function of the iteration, for the same period.

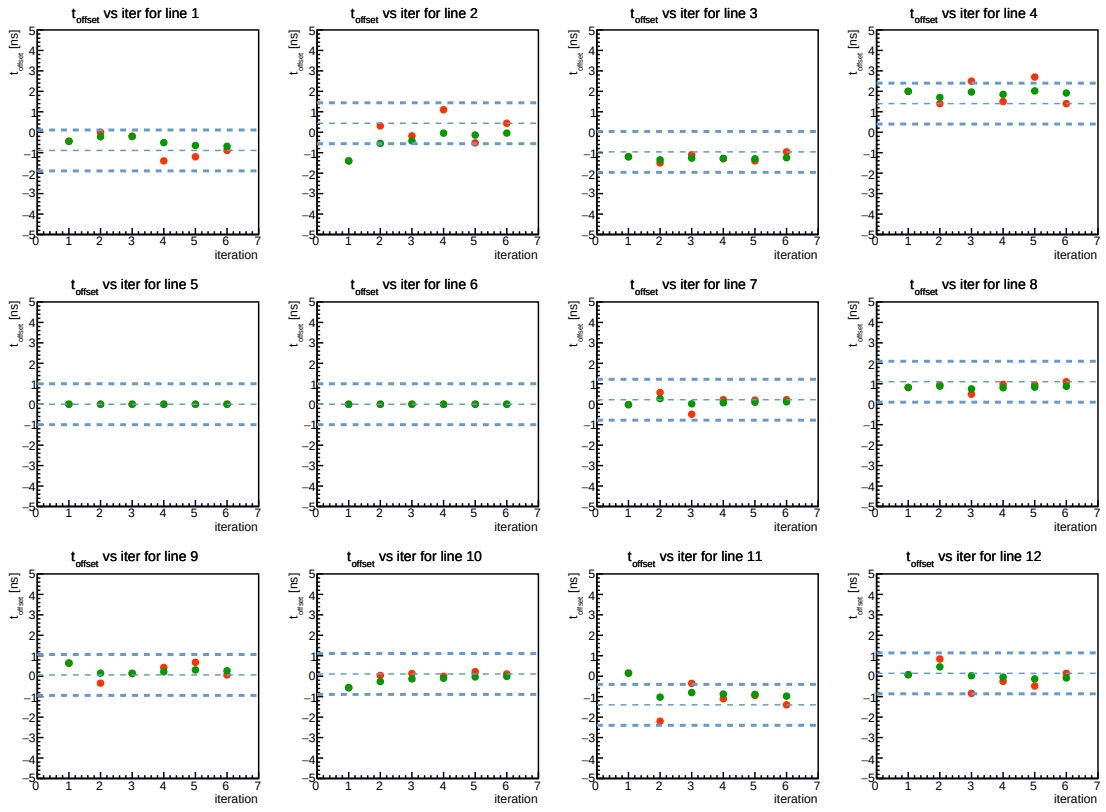

Figure 5.9: Inter-line time offsets calculated using data of July 2017. Lines 5 and 6 were not operative at that time. For each iteration, the value of the correction introduced in the following iteration is shown as a red dot, while the average value until the given iteration is shown as a green dot.

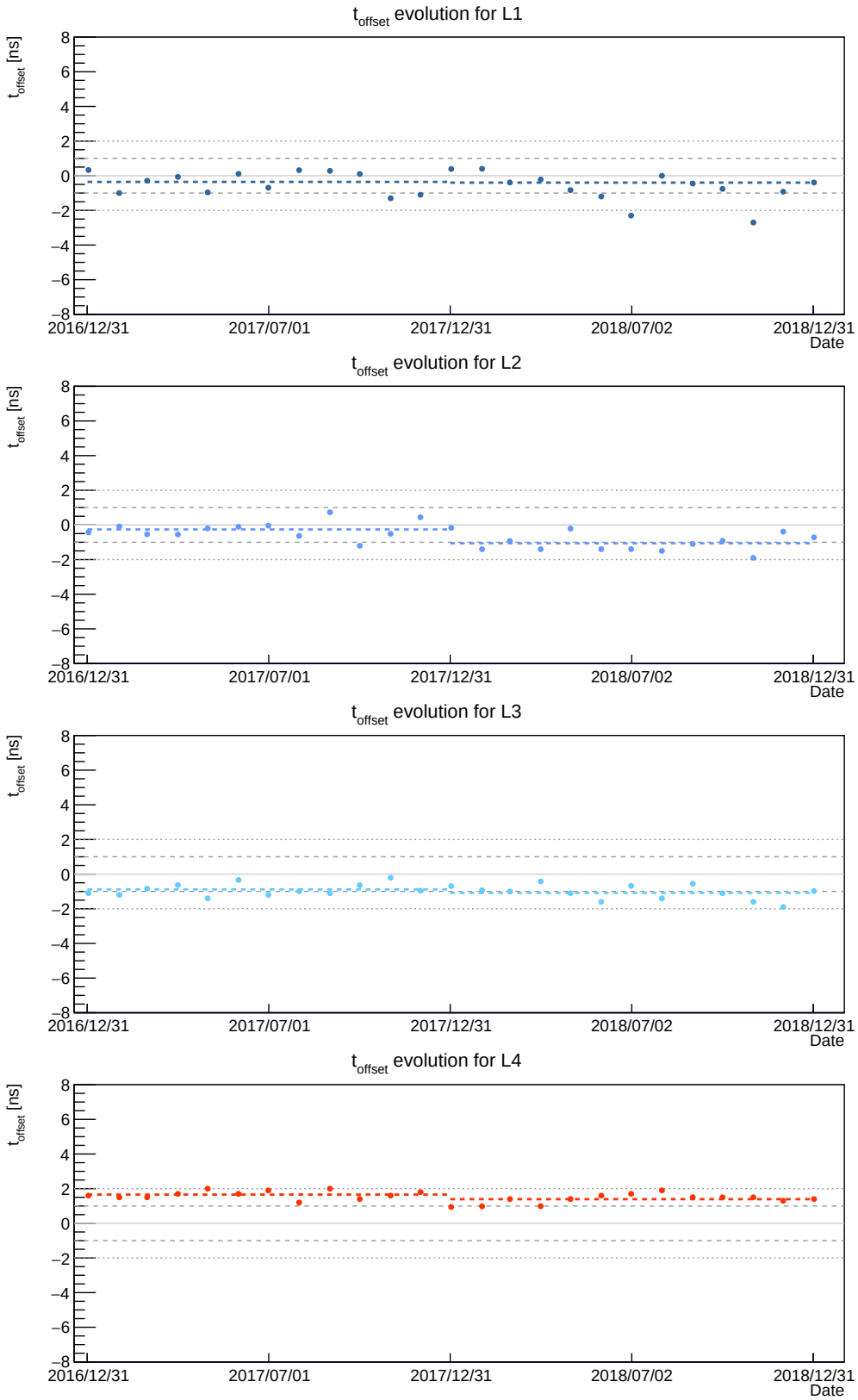

Figure 5.10: Final inter-line time offsets for Lines 1, 2, 3 and 4 calculated for the period from the beginning of 2017 to the end of 2018. The horizontal dashed line represents the mean value of the time offsets averaged over a year.

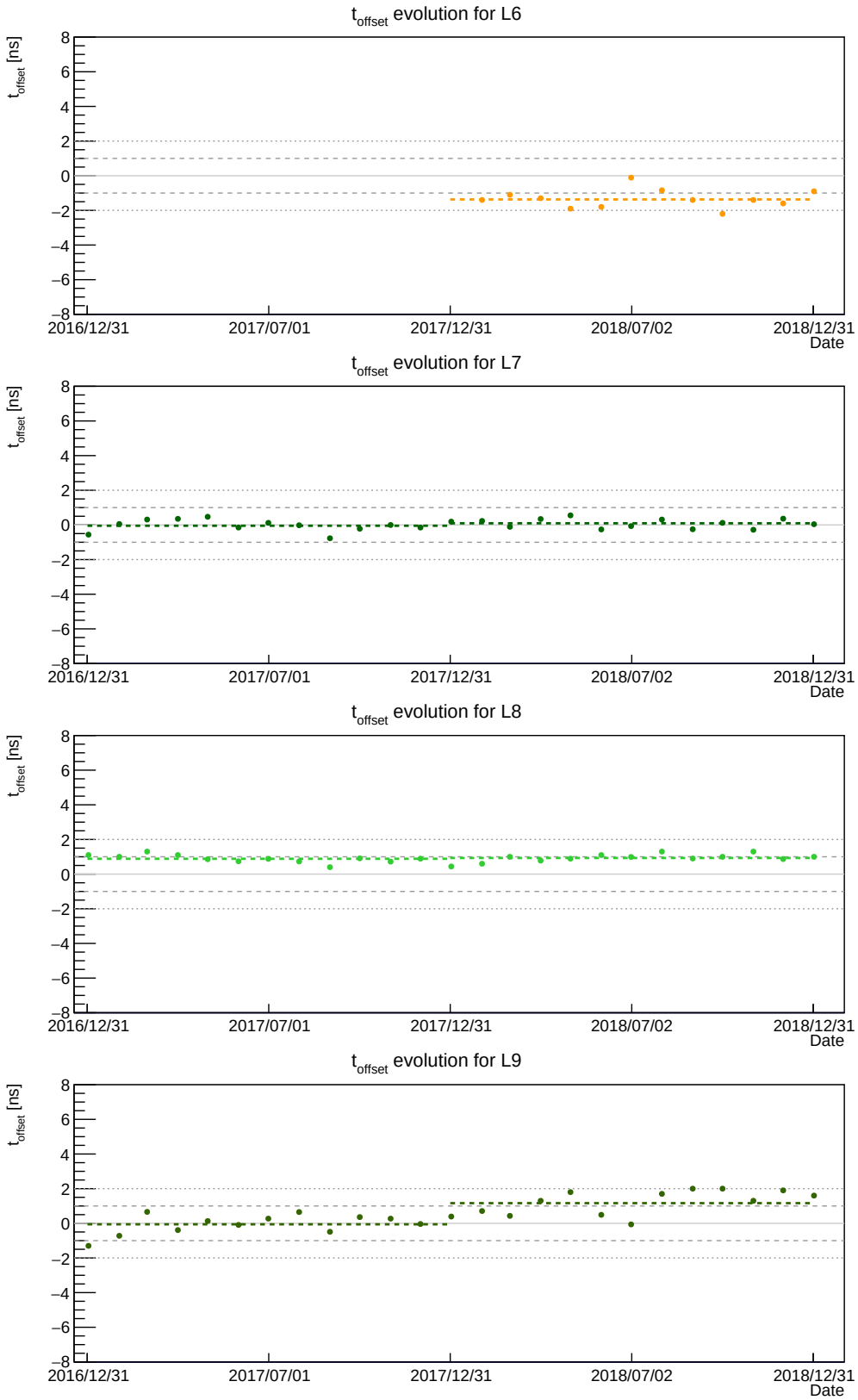

Figure 5.11: Final inter-line time offsets for Lines 6, 7, 8 and 9 calculated for the period from the beginning of 2017 to the end of 2018. The horizontal dashed line represents the mean value of the time offsets averaged over a year.

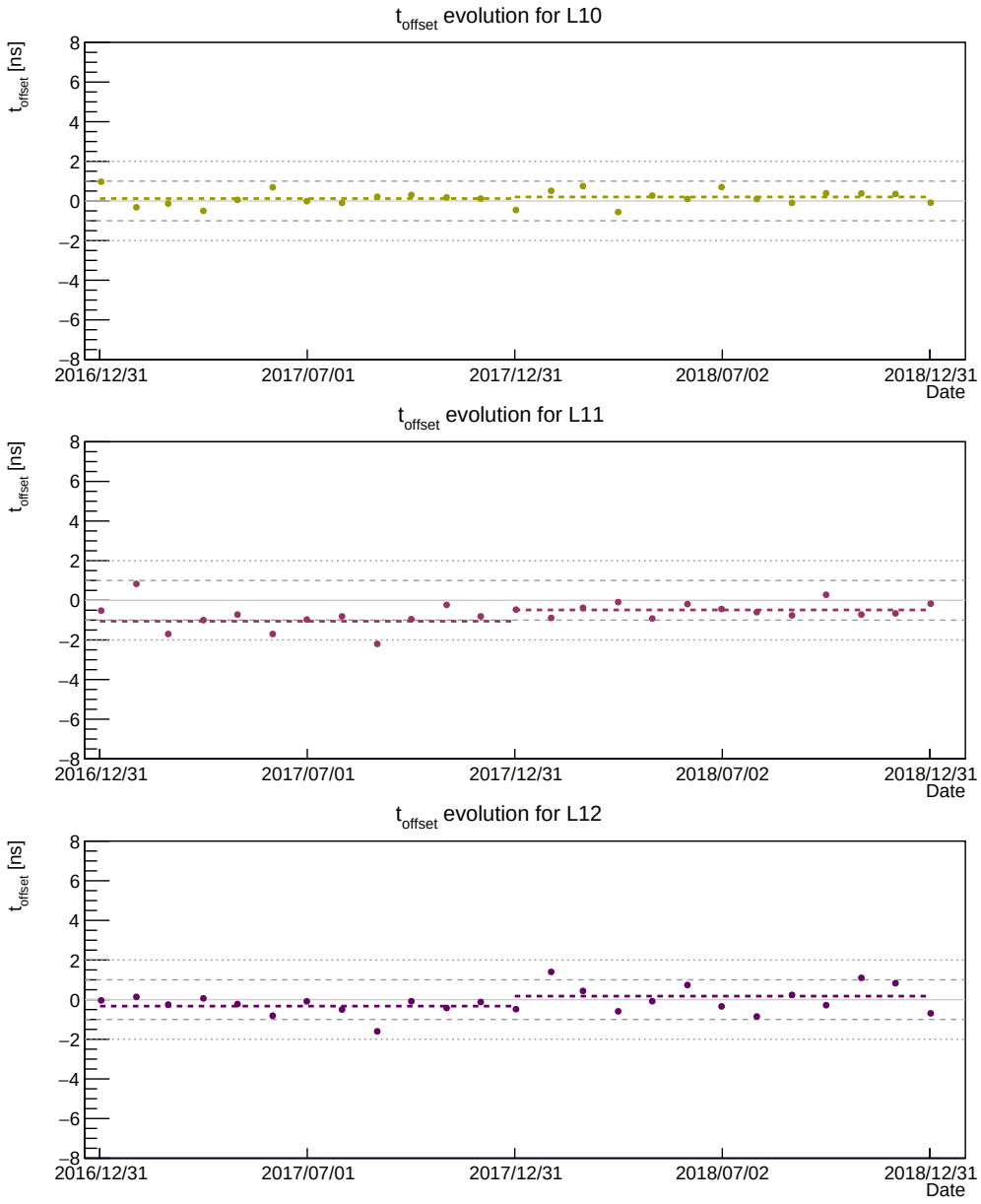

Figure 5.12: Final inter-line time offsets for Lines 10, 11, and 12 calculated for the period from the beginning of 2017 to the end of 2018. The horizontal dashed line represents the mean value of the time offsets averaged over a year.

5.3.2 Intra-storey calibration with ^{40}K events

The ^{40}K events are used to derive the time offsets among ARSs of the same storey. A subset of 20 runs randomly chosen from the list of runs used in the inter-line calibration with atmospheric muons (Section 5.3.1) is employed in this calibration. For each pair of ARSs, the distribution of the time differences between hits detected within a time window of 50 ns is obtained, and fitted with a Gaussian. For each storey, one of the ARS is taken as reference r and the time offset between the reference ARS and any other ARS j in the same storey, Δt_{rj}, is computed. Since the two ARSs in the same OM never operate simultaneously, the time offset between the reference ARS and the ARS k in the same OM is computed as $\Delta t_{rk} = \Delta t_{rj} - \Delta t_{jk}$, with j being another ARS of the same storey used as auxiliary ARS. For each storey, the ARS chosen as reference is the one with the largest number of successful Gaussian fits of the time difference distributions with the other ARSs. The intra-storey corrections derived with this method are employed in the third step of the calibration procedure (see Section 5.3.3).

5.3.3 Inter-storey calibration with atmospheric muons

The inter-storey calibration with atmospheric muons is the last step of the calibration procedure. As in the case of the inter-line calibration, a series of iterations is performed until a convergence in the result is reached. The first iteration makes use of the corrections derived with the two previous steps of the procedure. Only events with a value of the AAFit quality parameter $\Lambda > -6.5$ are employed in this case. Using a similar procedure as in the inter-line calibration with atmospheric muons (Section 5.3.1), the distribution of time residuals for each storey is obtained, and a Gaussian fit is performed around the peak region. The average value of the distribution of the mean values obtained in the Gaussian fits is used to compute the correction for each storey, defined as the difference between the average value and the mean value of the given storey. When the standard deviation of the mean values reaches a value ≤ 0.35 ns, the procedure is stopped. As an example, Figure 5.13 shows the distribution of the mean values together with the Gaussian fit calculated for the period of July 2017 after the first and last iteration.

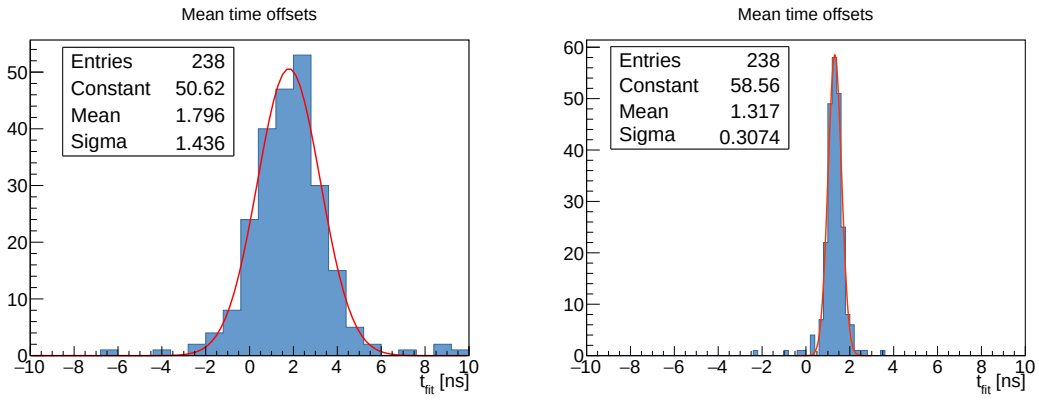

Figure 5.13: Distribution of the mean values obtained for July 2017 together with the Gaussian fit after the first iteration (left) and last iteration (right).

6

Search methods for point-like and extended sources of astrophysical neutrinos

The challenge in high-energy neutrino astronomy is the identification of excesses of events from single sources above the random background fluctuations. In order to spot these clusters of signal events, an unbinned likelihood method is applied. The likelihood describes the data in terms of probability density functions and makes use of distinguishing features that help to separate signal from background. The unbinned likelihood method is described in Section 6.1. In order to determine the response of the likelihood to the potential signal, a large number of so-called pseudo-experiments, in which the likelihood method is applied on simulated pseudo-data sets, is performed. The procedure of pseudo-experiment generation is described in Section 6.2. Pseudo-experiments are also used to obtain the distribution of the test statistic for different signal hypotheses, necessary to determine the statistical significance of a cluster of events, to estimate the expected performance of the method, and to set upper limits on the neutrino flux from a source, as explained in Section 6.3.

6.1 Unbinned likelihood method

The data recorded by a high-energy neutrino telescope consist of a set of events distributed over the sky, each with a reconstructed direction, energy and time. At any given direction in the sky, two hypotheses can be formulated:

- H_0: the data consist solely of background;
- H_S: the data contain also astrophysical neutrino events coming from a source with some given features. The characteristic features of the source (model parameters), such as energy spectrum, extension, duration of the flaring emission, included in the definition of H_S, can either be fixed values in case a particular source model is assumed, or can be free parameters.

The probabilities, i.e. the likelihood, of obtaining the observed data given each of the two hypotheses, $\mathcal{L}(Data|H_0)$ and $\mathcal{L}(Data|H_S)$, can be determined, and their ratio is used to define a Test Statistic (TS) as [129]:

$$TS = -2 \cdot \log \left[\frac{\mathcal{L}(Data|H_0)}{\mathcal{L}(Data|H_S)} \right] , \tag{6.1}$$

where larger values of TS indicate data less compatible with being produced by pure background. The likelihood makes use of signal and background probability density functions (PDFs) to describe the data and is a function of the free model parameters. By maximising $\mathcal{L}(Data|H_S)$ with respect to the free parameters, the best estimation of these can be found.

6.1.1 Likelihood and test statistic definition

Given a set of observed events, the maximum likelihood method allows to estimate the value of a set of model parameters by finding those parameters that maximize the probability of getting the observed data. First, the likelihood function needs to be defined. If $\mathbf{x} = \{x_1 \ \cdots \ x_{\mathcal{N}}\}$ is the set of $\mathcal{N}$ independent observations, $\boldsymbol{\theta} = \{\theta_1 \ \cdots \ \theta_m\}$ the set of m unknown parameters, and $p(x; \boldsymbol{\theta})$ the PDF for x, then the likelihood of observing $\mathbf{x}$ is given by the product of the PDFs over all the observed events [129]

$$\mathcal{L}(\boldsymbol{\theta}) = \prod_{i=1}^{\mathcal{N}} p(x_i; \boldsymbol{\theta}) \,. \tag{6.2}$$

In the standard maximum likelihood (ML) definition, the integral of each PDF over the range of allowed values for x is normalised to unity,

$$\int p(x; \boldsymbol{\theta})\, dx = 1 \,. \tag{6.3}$$

The standard version of the likelihood used in the point-like and extended source searches can be written as

$$\mathcal{L}^{\mathrm{ML}}(n_s, \boldsymbol{\theta}') = \prod_{i=1}^{\mathcal{N}} \left(\frac{n_s}{\mathcal{N}} \mathcal{S}_i(\boldsymbol{\theta}') + \frac{\mathcal{N} - n_s}{\mathcal{N}} \mathcal{B}_i \right) , \tag{6.4}$$

or in its logarithmic form as

$$\log \mathcal{L}^{\mathrm{ML}}(n_s, \boldsymbol{\theta}') = \sum_{i=1}^{\mathcal{N}} \log \left(\frac{n_s}{\mathcal{N}} \mathcal{S}_i(\boldsymbol{\theta}') + \frac{\mathcal{N} - n_s}{\mathcal{N}} \mathcal{B}_i \right) . \tag{6.5}$$

In Equations 6.4 and 6.5, the arguments of the likelihood function are the free model parameters: n_s is the number of detected signal events (signal strength), which is always fitted in the likelihood maximization, and $\boldsymbol{\theta}'$ is a set of additional model parameters – such as source extension, spectral index, flare duration – which may be also left free depending on the specific kind of search (see Chapter 7). $\mathcal{S}_i$ and $\mathcal{B}_i$ represent the signal and the background PDFs, respectively, and will be described in Section 6.1.2.

In the searches for cosmic neutrinos described in Chapter 7, an alternative definition of the maximum likelihood, the extended maximum likelihood (EML) [130], is also used. In this case, the PDFs, $P(x; \boldsymbol{\theta})$, are normalised to the total number of expected events over the whole range of observations, N, which can depend on the unknown parameters $\boldsymbol{\theta}$:

$$\int P(x; \boldsymbol{\theta}) dx = N(\boldsymbol{\theta}) \,. \tag{6.6}$$

In order to avoid a large normalization in the maximisation process which may occur due to the replacement of $p(x;\boldsymbol{\theta})$ with $P(x;\boldsymbol{\theta})$, a further change in the likelihood definition is required. In particular, the likelihood must incorporate not only the information that the events were observed at x, but also that they were not observed anywhere else, as explained in [130]. The range of x is divided into bins of length Δx small enough so that the probability that one bin contains more than one event is negligible. The probabilities to detect no event and one event in a bin are given, respectively, by

$$P_0(x) = e^{-\Delta x P(x)}, \tag{6.7}$$

$$P_1(x) = \Delta x P(x) e^{-\Delta x P(x)}, \tag{6.8}$$

which leads to the combined extended likelihood for the complete data sample,

$$\mathcal{L} = \prod_j \Delta x P(x_j) \prod_k e^{-\Delta x P(x_k)}, \tag{6.9}$$

where the first product is over all bins containing only one event, and the second one is over all bins. In the limit of $\Delta x \to dx$ the second term becomes $\prod_k e^{-\Delta x P(x_k)} \to e^{-\sum_k \Delta x P(x_k)} \to e^{-\int P(x) dx} \to e^{-N}$ and the extended likelihood and its logarithmic form, respectively, simplify in

$$\mathcal{L} = \left[\prod_{i=1}^{\mathcal{N}} P(x_i)\right] e^{-N}, \tag{6.10}$$

$$\log \mathcal{L} = \sum_{i=1}^{\mathcal{N}} \log P(x_i) - N. \tag{6.11}$$

The expected number of events N is given by the sum of the signal and background events. As the signal contribution in the data sample is expected to be small, the full data sample can be treated as background. Therefore, the extended likelihood used in point-like and extended source searches can be written as

$$\log \mathcal{L}^{\mathrm{EML}}(n_s, \boldsymbol{\theta}') = \sum_{i=1}^{\mathcal{N}} \log \left[n_s \mathcal{S}_i(\boldsymbol{\theta}') + \mathcal{N}\mathcal{B}_i\right] - \mathcal{N} - n_s, \tag{6.12}$$

where the same definitions of the variables given for the standard maximum likelihood (Equations 6.4 and 6.5) apply.

Whether the standard or the extended definition is used, the likelihood is then maximized with respect to n_s and $\boldsymbol{\theta}'$ giving the best-fit values $\hat{n}_s$ and $\hat{\boldsymbol{\theta}}'$. The case of $n_s = 0$ represents the pure background hypothesis. The test statistic defined in Equation 6.1 can be then rewritten as

$$TS = -2 \cdot \log \left[\frac{\mathcal{L}(Data|H_0)}{\mathcal{L}(Data|H_S)} \right] = -2 \cdot \log \left[\frac{\mathcal{L}(n_s = 0)}{\mathcal{L}(\hat{n}_s, \hat{\boldsymbol{\theta}}')} \right] . \tag{6.13}$$

6.1.2 Likelihood PDFs

Signal events from a point-like or extended source are expected to cluster around the direction of the source with a spread which depends on the detector angular resolution. Moreover, the energy spectrum of astrophysical neutrinos is significantly harder than that of atmospheric neutrinos, which approximately behaves as a power-law asymptotically steeper than the primary cosmic ray flux by one power of the energy [7]. This makes the angular and the energy distributions of the events powerful features to distinguish signal from background. For this reason, in searches for steady emission of cosmic neutrinos from point-like and extended sources (time-integrated searches) the signal and background PDFs, $\mathcal{S}_i$ and $\mathcal{B}_i$ (Equations 6.4, 6.5, 6.12), are obtained as the product of a space and an energy term:

$$\mathcal{S}^{\text{steady}} = \mathcal{S}^{\text{space}} \cdot \mathcal{S}^{\text{energy}} , \tag{6.14}$$

$$\mathcal{B}^{\text{steady}} = \mathcal{B}^{\text{space}} \cdot \mathcal{B}^{\text{energy}} . \tag{6.15}$$

In case of searches for point-like sources emitting a non-steady neutrino flux, the information of the neutrino arrival times becomes an additional distinguishing feature. Indeed, when dealing with transient emissions, the background of atmospheric neutrinos can be significantly reduced by limiting the search to a small time window around the source flare. A time-dependent term is therefore included in the definition of the signal and background PDFs:

$$\mathcal{S}^{\text{transient}} = \mathcal{S}^{\text{space}} \cdot \mathcal{S}^{\text{energy}} \cdot \mathcal{S}^{\text{time}} , \tag{6.16}$$

$$\mathcal{B}^{\text{transient}} = \mathcal{B}^{\text{space}} \cdot \mathcal{B}^{\text{energy}} \cdot \mathcal{B}^{\text{time}} . \tag{6.17}$$

A description of the space, energy and time PDFs for signal and background follows.

Space signal PDF: $\mathcal{S}^{\text{space}}$ describes the probability density of reconstructing a signal event at a certain angular distance from the direction of the source and depends on the angular resolution of the detector. In ANTARES, a parameterisation of the Point Spread Function (PSF) is usually employed as space signal PDF. The shape of the PSF is determined from Monte Carlo simulations of cosmic neutrinos for the assumed signal energy spectrum. In case of testing for extended sources, the PSF is built assuming that the original direction of the events is distributed according to the assumed emission profile around the source location. As an example, the ANTARES cumulative distribution of the angular resolution for tracks and showers used in the 11-year ANTARES point-like source search (see Section 7.1) for an $E_\nu^{-2.0}$ spectrum is shown in Figure 6.1.

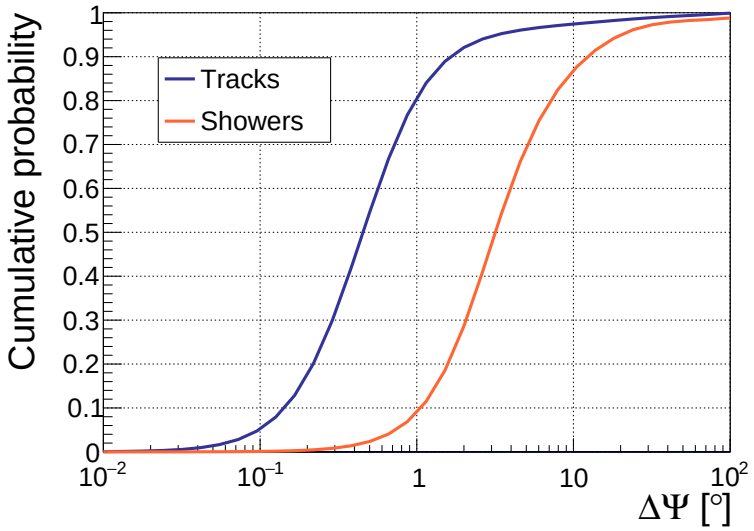

Figure 6.1: Cumulative angular resolution distribution for an $E_\nu^{-2.0}$ spectrum for the track (blue) and the shower (orange) samples selected for the 11-year ANTARES point-like source search (see Section 7.1).

Space background PDF: the probability of reconstructing a background event at a certain declination is employed as $\mathcal{B}^{\text{space}}$. Given the small expected contribution of signal events in the data set, this PDF can be directly derived from the observed data. As an example, the declination distribution of the ANTARES events selected in the 11-year point-like source search (see Section 7.1) is shown in Figure 6.2.

Energy signal PDF: $\mathcal{S}^{\text{energy}}$ describes the probability of obtaining a signal event with a certain value of the energy estimator. This PDF is built from Monte

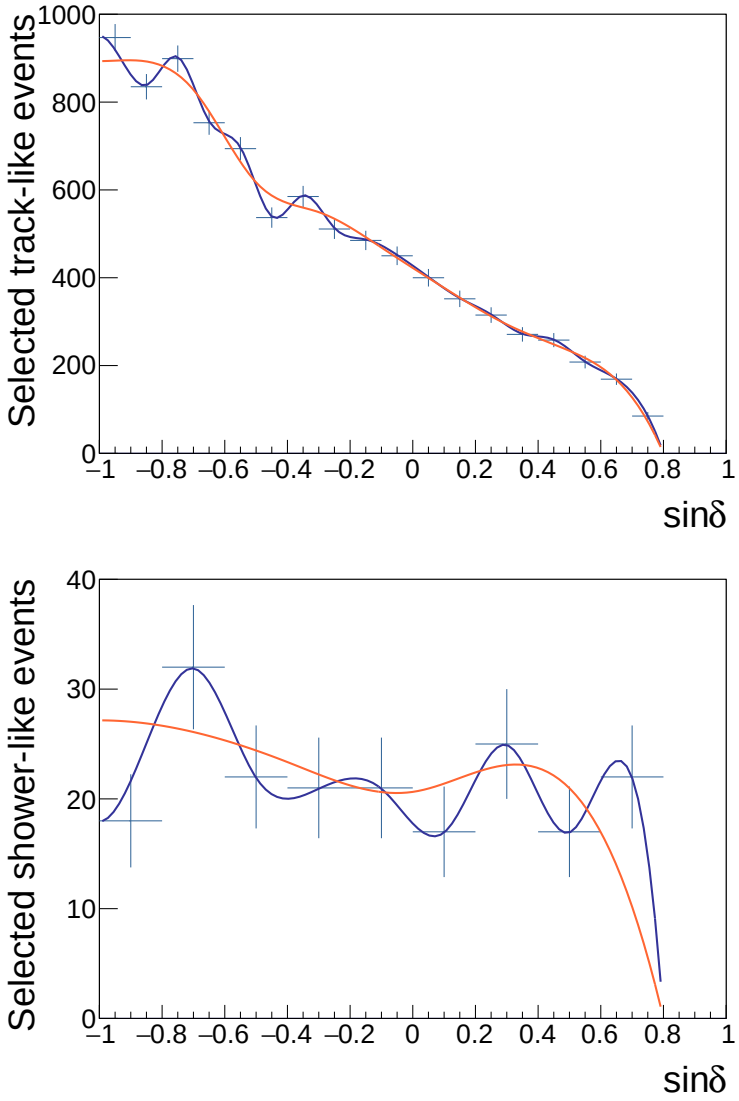

Figure 6.2: Number of selected track-like events (top) and shower-like events (bottom) as a function of the reconstructed declination for the 11-year ANTARES point-like source search (see Section 7.1). The solid lines are two different parameterisations used in the simulation (see Section 7.1.4).

Carlo simulations of cosmic neutrinos for the assumed signal energy spectrum. Typically, a source spectrum proportional to $E_\nu^{-2.0}$ is used to account for the prediction of the Fermi acceleration mechanism (see Chapter 1). However, in view of the recent best-fit spectral indices of the isotropic flux of high-energy cosmic neutrinos measured by the IceCube Collaboration ($\gamma = 2.28$ [52], $\gamma = 2.92$ [48]), softer spectral indices are also considered. Alternatively, a generic $E_\nu^{-\gamma}$ spectrum can be assumed, being a free parameter in the likelihood maximisation. As an example, the energy signal PDFs for an $E_\nu^{-2.0}$ spectrum used in the 11-year

point-like source search (see Section 7.1) are shown in Figure 6.3.

Energy background PDF: $\mathcal{B}^{\text{energy}}$ describes the probability of obtaining a background event with a certain value of the energy estimator. It is derived from Monte Carlo simulations of atmospheric neutrinos. The energy background PDFs used in the 11-year point-like source search (see Section 7.1) are shown in Figure 6.3.

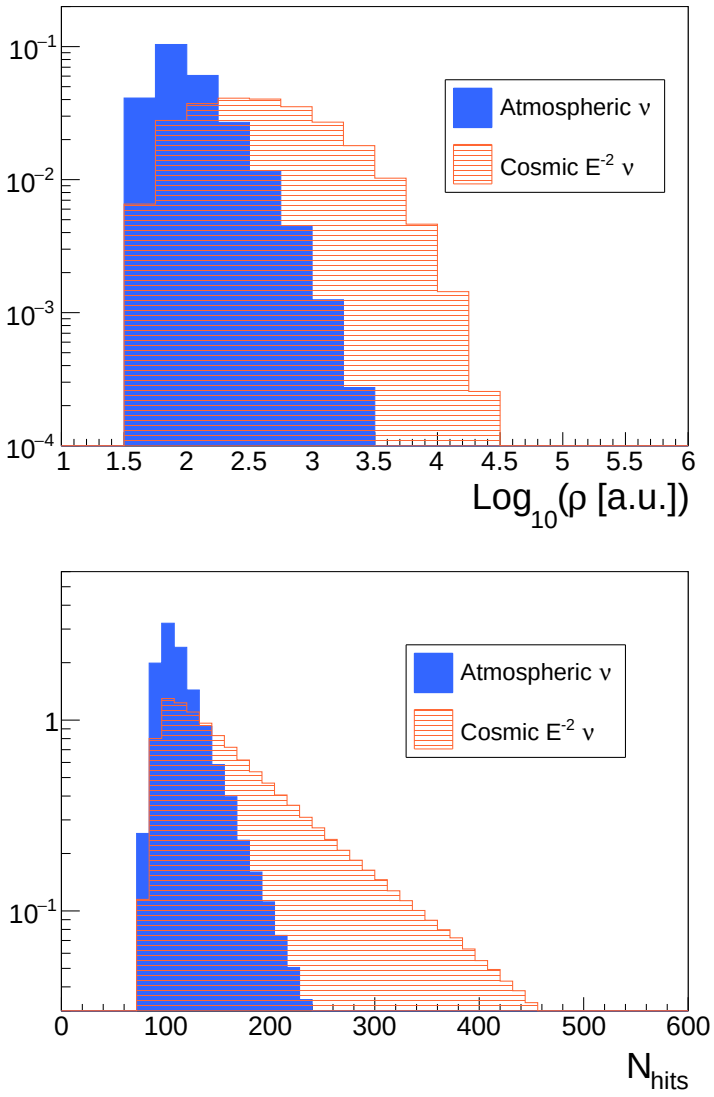

Figure 6.3: Energy background (blue) and signal (orange) PDFs for the track-like (top) and the shower-like (bottom) events used in the 11-year ANTARES point-like source search (see Section 7.1). The energy estimators are ρ for tracks and the number of hits used by the reconstruction algorithm, N^{hits}, for showers.

Time signal PDF: $\mathcal{S}^{\text{time}}$ describes the probability of detecting a signal event at a certain time. In case of searches for neutrinos from known $\gamma-$rays sources

with measured lightcurves, the emission time distribution from photon observations can be used to shape this PDF assuming that neutrinos follow the same emission time profile as $\gamma-$rays. When the emission time distribution is not known a priori, generic shapes, such as Gaussian-shaped or box-shaped profiles, may be assumed.

Time background PDF: $\mathcal{B}^{\text{time}}$ describes the probability to observe a background event at a given time. Periods with no data taking due to detector maintenance or with low quality data, caused for instance by high bioluminescence, affect the shape of this PDF. Given the small expected contribution of a cosmic signal in the overall data set, $\mathcal{B}^{\text{time}}$ is built using the time distribution of data events, ensuring a time profile proportional to the measured data.

6.2 Pseudo-experiments

Pseudo-experiments (PEs) are performed in order to obtain the TS distributions for different signal hypotheses, necessary for determining the significance of a cluster of events, estimating the expected performances of the search in terms of discovery power and sensitivity, and setting upper limits. In each PE, the search method is applied on a pseudo-data set made of events randomised in right ascension to eliminate any possible clustering in space and time due to potential sources present in the data. In each PE, a randomised sky map containing a certain number of signal events and as many background events as events selected in the data are simulated. In addition to the equatorial coordinates that identify the location of the event on the sky map, one value for each of the other variables that enter the likelihood PDFs – such as the energy estimator, the angular error estimate, and the observation time (in case of time-dependent searches)– is assigned to each simulated event. Details on the PEs generation process follows.

Signal generation. Prior to the simulation of the signal events, multi-dimensional histograms containing the correlated information of the angular resolution, i.e. the angular distance between the original and the reconstructed neutrino direction, the energy estimator and the angular error estimate, i.e. the error estimate on the fitted direction provided by the reconstruction algorithm (see Equation 4.6), are produced using Monte Carlo simulations of cosmic neutrinos. Since the performance of the reconstruction depends on the declination of the events, the sky is divided into multiple declination bands with a step of 0.2 in $\sin\delta$ and for each band a different histogram is produced. An example of multi-dimensional

histogram used in the simulation of signal events is shown in Figure 6.4. For each simulated signal event, a triplet given by angular resolution, energy estimator and angular error estimate is randomly drawn from the histogram corresponding to the declination of the source. The information of the angular resolution is used to generate the angular distance between the reconstructed and the true direction of the signal event. For point-like sources, the true direction is given by the direction of the source, while for extended sources, the true direction is drawn from the assumed space emission profile. As for time-dependent searches, a random time drawn from the assumed time emission shape is assigned to each signal event.

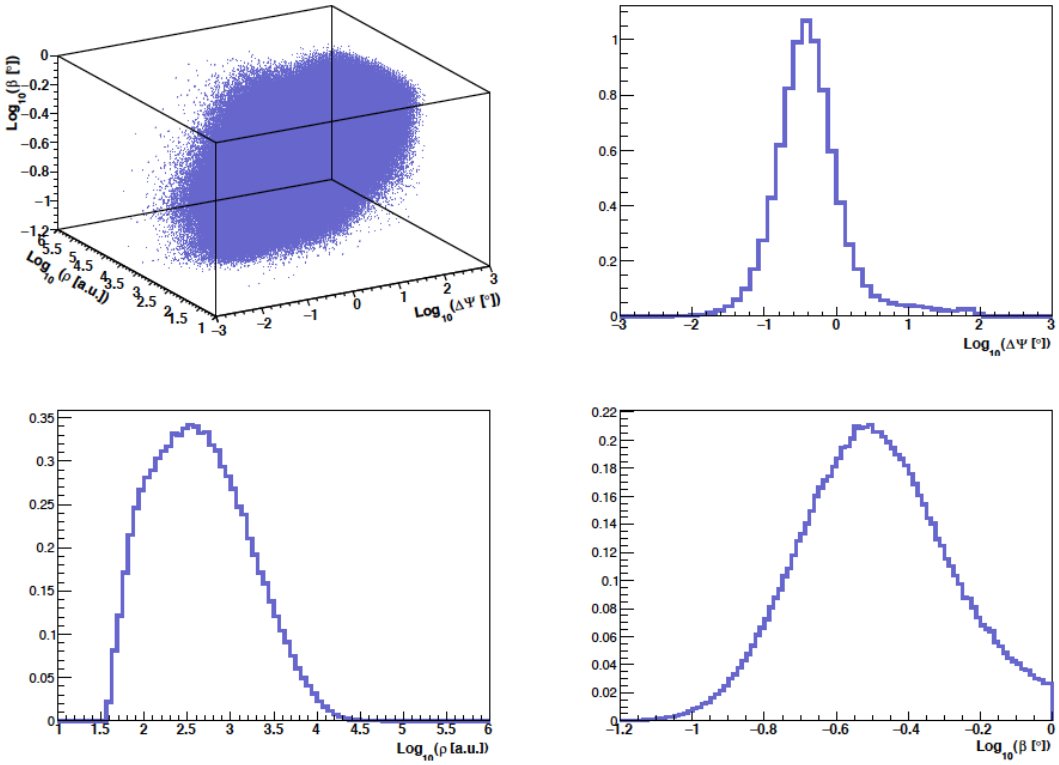

Figure 6.4: Top left: example of multi-dimensional histogram containing the information of the angular resolution $\Delta\Psi$, energy estimator ρ, and angular error estimate β, used in the generation of signal events from a source at a declination $-0.8 \leq \sin\delta \leq -0.6$ in ANTARES analyses. See Chapter 7 for more details on the variables. Top right, bottom left and bottom right: projections of the multi-dimensional histogram along each of the three axes.

Background generation. A number of background events equal to the number of selected events in data is injected in each sky map. In case of time-integrated searches, the background events are distributed in declination according to the distribution of $\sin\delta$ of the data events, and uniformly in right ascension. As for the time-dependent search, the directions and times of the background events

are randomly drawn from the distributions of the local coordinates ($\cos\theta$ and ϕ) and time obtained from the actual data and then converted into equatorial coordinates in order to ensure that the generated position in the sky is actually visible at the time of the event. Moreover, the energy estimator and the angular error estimate are randomly extracted from 2D histograms obtained from the observed data and produced in steps of 0.2 in $\sin\delta$.

The output of the process of PE generation consists of a set of TS distributions, $\mathcal{D}(TS)$, one for each integer number of simulated detected signal events, μ_s,

$$\mathcal{D}(TS \mid \mu_s) \quad , \quad \mu_s \in \{0, 1, 2, \dots, N^{\max}\} \,, \tag{6.18}$$

with $N^{\max}$ being the maximum number of simulated signal events. For point-like source searches with ANTARES, $N^{\max}$ is typically 30.

Since the amount of detected signal events is expected to undergo fluctuations, TS distributions for the fixed number μ_s is replaced with TS distributions for a Poisson mean number of detected events $\bar{\mu}_s$. The new TS distributions are calculated as

$$\mathcal{D}(TS \mid \bar{\mu}_s) = \sum_{\mu_s=0}^{N^{\max}} \mathcal{D}(TS \mid \mu_s)\, \mathcal{P}(\mu_s \mid \bar{\mu}_s) \,, \tag{6.19}$$

where $\mathcal{P}(\mu_s \mid \bar{\mu}_s)$ is the Poisson probability to detect μ_s events given a mean of $\bar{\mu}_s$ events.

A further modification of the TS distributions is needed in order to account for the systematic uncertainty on the number of detected events. Because of this, the true value of $\bar{\mu}_s$ is unknown. Therefore, TS distributions for an estimation of $\bar{\mu}_s$, $\hat{\mu}_s$, are obtained, assuming that the probability for the true $\bar{\mu}_s$ is described by a Gaussian $\mathcal{G}$ with standard deviation $\sigma_{\hat{\mu}_s}$,

$$\mathcal{D}(TS \mid \hat{\mu}_s) = \sum_{\mu_s=0}^{N^{\max}} \mathcal{D}(TS \mid \mu_s) \int \mathcal{P}(\mu_s \mid \bar{\mu}_s)\, \mathcal{G}(\bar{\mu}_s \mid \hat{\mu}_s, \sigma_{\hat{\mu}_s})\, d\bar{\mu}_s \,. \tag{6.20}$$

A value of 15% is used for $\sigma_{\hat{\mu}_s}$, estimated by performing comparisons between the atmospheric neutrino data and MC simulations with reduced efficiency of the OMs [131]. The TS distributions defined in Equation 6.20 are used for the calculation of relevant quantities, as explained in Section 6.3.

6.3 Significance, upper limits, discovery potential, and sensitivity

In order to test for the presence of cosmic neutrino sources, the likelihood method is applied on the real data looking at a given direction in the sky. At the tested direction, a value of the test statistic, TS^{obs}, is calculated. Whether TS^{obs} is large enough to claim a significant discovery depends on how likely it is that the background alone produces an equal or larger value of TS. This is estimated by comparing TS^{obs} to the distribution of TS obtained in background-only PEs, i.e. PEs where only background events are simulated, in which the given direction is tested. The significance, or *p-value*, of the observation is given by the fraction of background-only simulations in which a TS equal or higher than TS^{obs} is obtained,

$$\text{p-value} = \int_{TS^{\text{obs}}}^{\infty} \mathcal{D}(TS \mid \mu_s = 0)\, dTS\,. \tag{6.21}$$

Lower p-values indicate smaller chances for the pure background to have produced the observed TS. When many directions in the sky are investigated, a trial correction has to be applied when estimating the significance of the observation. To this purpose, the obtained p-value (in this case called pre-trial p-value), p-value$^{\text{obs}}$, is compared to the distribution of pre-trial p-values obtained when performing the same analysis on many background-only PEs. The fraction of PEs in which a value of the pre-trial p-value lower than p-value$^{\text{obs}}$ is obtained gives the trial-corrected significance (post-trial p-value) of the observation. Significances are often expressed in number of corresponding standard deviations σ of a Gaussian normal distribution, e.g. 3σ and 5σ significances correspond to a p-value of $\sim 2.7 \cdot 10^{-3}$ and $\sim 5.7 \cdot 10^{-7}$ (in the two-sided sigma convention), respectively. In high-energy physics, a significance of 5σ is the typical threshold that must be crossed to claim a discovery.

If the threshold is not crossed, an upper limit on the mean number of detected signal events $\hat{\mu}_s$ (defined in Equation 6.20) can be set, so that values of $\hat{\mu}_s$ higher than the upper limit are excluded at a given confidence level (CL). In the analyses presented in Chapter 7, upper limits at 90% CL, derived using the Neyman approach [132], are provided. The upper limit is defined as the value of $\hat{\mu}_s$, $\hat{\mu}_s^{90\%\text{CL}}$, for which the probability to get a value of TS equal or larger than TS^{obs} is 90%:

$$\int_{TS^{\text{obs}}}^{\infty} \mathcal{D}(TS \mid \hat{\mu}_s^{90\%\text{CL}})\, dTS \equiv 90\% \,. \tag{6.22}$$

Before applying the search method to the real data, the performances of the analysis are estimated in terms of two quantities: 5σ discovery potential and sensitivity. The 5σ discovery potential is defined as the mean number of detected signal events, $\hat{\mu}_s^{5\sigma}$, that yields a 5σ discovery in 50% of the trials,

$$\int_{TS^{5\sigma}}^{\infty} \mathcal{D}(TS \mid \hat{\mu}_s^{5\sigma})\, dTS \equiv 50\% \,. \tag{6.23}$$

In Equation 6.23, $TS^{5\sigma}$ is the value of TS that, if observed in the measured data, would correspond to a significance of 5σ, i.e. a p-value of $\sim 5.7 \cdot 10^{-7}$ (see Equation 6.21), and is estimated from background-only PEs. Since simulating enough PEs in order to properly calculate $TS^{5\sigma}$ is computationally too expensive, $TS^{5\sigma}$ is estimated by fitting the background TS distribution as it is expected to follow a χ^2 distribution with a number of degrees of freedom equal to the number of parameters left free in the likelihood maximization, as stated by the Wilk's theorem [133]. In order to maximise the chances of a significant discovery, the selection criteria are chosen as those that minimise the 5σ discovery potential.

Another relevant quantity in the estimation of the analysis performances is the sensitivity. It is defined as the median upper limit, i.e. the upper limit that would be obtained if the observed TS corresponded to the median value of the background TS distribution, TS^{med}. With reference to Equation 6.22, the sensitivity $\hat{\mu}_s^{90\%\text{CL}}$ is obtained by replacing TS^{obs} with TS^{med}. In order to ensure a proper calculation of TS^{med} from background-only PEs, it is important to carefully choose the lower boundary for the number of detected signal events in the likelihood maximization, n_s^{min}, as explained in [90]. Indeed, if n_s^{min} is set to $n_s^{\text{min}} = 0$, a test statistic $TS = 0$ is obtained in more than 50% of the PEs, leading to an over-estimation of the sensitivity. By setting n_s^{min} slightly above 0, e.g. $n_s^{\text{min}} = 10^{-3}$, the test statistic TS gets negative values for under-fluctuations of the signal. This makes it possible to properly calculate the median of the background TS-distribution. Furthermore, in order to facilitate the calculation of the median, the following transformation is performed to obtain the TS-distributions:

$$TS_{\text{new}} = \log_{10}(TS + K) \,, \tag{6.24}$$

where K is a constant with a value close to $n_s^{\min}$. In the searches presented in Chapter 7, values of $n_s^{\min} = 10^{-3}$ and of $K = 1.5 \times 10^{-3}$ are used. Previous studies have showed that no significant changes in the sensitivity are observed when using slightly different values for $n_s^{\min}$ and K [90] .

The upper limits, discovery potential and sensitivity expressed as mean number of detected signal events describe the detector response and need to be translated into a quantity related to the cosmic source which allows to compare results of different experiments: the source differential astrophysical neutrino flux measured at Earth. Unless otherwise stated, in the analyses presented in Chapter 7 this differential neutrino flux in energy is parameterised with an unbroken power-law,

$$\frac{d\Phi_{1\mathscr{F}}}{dE_\nu} \left(\mathrm{GeV}^{-1}\ \mathrm{cm}^{-2}\mathrm{s}^{-1}\right) = \Phi_0 \left(\frac{E_\nu}{E_0 = 1\ \mathrm{GeV}}\right)^{-\gamma}, \tag{6.25}$$

with Φ_0 being the neutrino flux normalization. In Equation 6.25 the subscript $1\mathscr{F}$ stands for the fact that limits are set on the one-flavour neutrino flux normalization assuming equipartition at Earth of the three neutrino flavours. For a given flux from a source at a given declination δ, the expected mean number of detected signal events is given by

$$\begin{aligned} \hat{\mu}_s(\delta, \gamma) &= \sum_{f \in \{\mu, e, \tau\}} \int\int \frac{d\Phi_{1\mathscr{F}}}{dE_\nu} A_{\mathrm{eff}}^{\nu_f + \bar{\nu}_f}(\delta, E_\nu)\, dE_\nu\, dt \\ &= \Phi_0 \sum_{f \in \{\mu, e, \tau\}} \int\int \left(\frac{E_\nu}{E_0}\right)^{-\gamma} A_{\mathrm{eff}}^{\nu_f + \bar{\nu}_f}(\delta, E_\nu)\, dE_\nu\, dt\,, \end{aligned} \tag{6.26}$$

where $A_{\mathrm{eff}}(\delta, E_\nu)$ is the effective area of the detector, i.e. the equivalent area of a detector with 100% efficiency, and the sum extends over the three neutrino flavours. The *acceptance* A, defined as

$$A(\delta, \gamma) = \sum_{f \in \{\mu, e, \tau\}} \int\int \left(\frac{E_\nu}{E_0}\right)^{-\gamma} A_{\mathrm{eff}}^{\nu_f + \bar{\nu}_f}(\delta, E_\nu)\, dE_\nu\, dt\,, \tag{6.27}$$

is the magnitude that allows to convert the expected mean number of detected signal events, $\hat{\mu}_s(\delta, \gamma)$, into a flux normalization, Φ_0:

$$\Phi_0 = \frac{\hat{\mu}_s(\delta, \gamma)}{A(\delta, \gamma)}\,. \tag{6.28}$$

As an example, the ANTARES acceptance for tracks and showers used in the 11-year ANTARES point-like source search (see Section 7.1) as a function of the source declination for an $E_\nu^{-2.0}$ spectrum is shown in Figure 6.5.

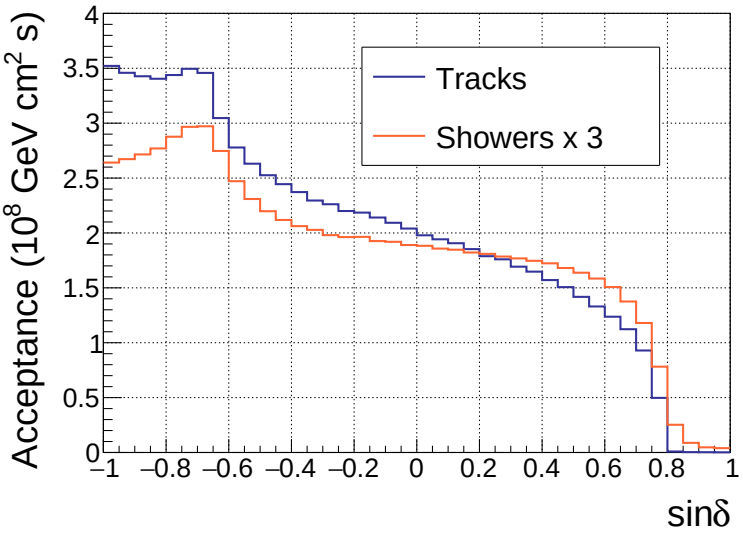

Figure 6.5: Acceptance as a function of the source declination for an $E_\nu^{-2.0}$ spectrum with a flux normalization $\Phi_0 = 10^{-8}\text{GeV}^{-1}\ \text{cm}^{-2}\text{s}^{-1}$ for the track (blue) and the shower (orange) samples selected for the 11-year ANTARES point-like source search (see Section 7.1). A scaling factor of 3 is applied to the shower acceptance for a better visibility.

When dealing with transient emissions, upper limits can be set on another magnitude, the one-flavour neutrino fluence $\mathcal{F}$, which accounts for the flaring period length and is defined as the integral in time and energy of the neutrino energy flux $E_\nu \cdot \frac{d\Phi_{1\mathscr{F}}}{dE_\nu}$:

$$\begin{aligned}\mathcal{F} &= \int_{t_{\min}}^{t_{\max}} \int_{E_{\min}}^{E_{\max}} E_\nu \cdot \frac{d\Phi_{1\mathscr{F}}}{dE_\nu}\, dE_\nu\, dt \\ &= \int_{t_{\min}}^{t_{\max}} \int_{E_{\min}}^{E_{\max}} E_\nu \cdot \Phi_0 \cdot \left(\frac{E_\nu}{E_0}\right)^{-\gamma} dE_\nu\, dt \\ &= \Delta T \cdot \Phi_0 \cdot \int_{E_{\min}}^{E_{\max}} E_\nu \cdot \left(\frac{E_\nu}{E_0}\right)^{-\gamma} dE_\nu\,.\end{aligned} \tag{6.29}$$

In Equation 6.29, the integral in time extends over the duration of the flare $\Delta T = t_{\max} - t_{\min}$ and the flux is assumed to be constant during this period. The parameters $E_{\min}$ and $E_{\max}$ represent the boundaries of the declination-dependent energy range containing 90% of the expected signal events.

7

Results of the searches for point-like and extended neutrino sources

As described in Chapter 1, astrophysical neutrinos play a unique role as cosmic messengers. Since they travel unattenuated and undeflected from the source to the Earth, cosmic neutrinos can lead to the discovery of distant astrophysical objects. Moreover, as only hadronic processes can produce high-energy neutrinos, they are a smoking-gun signature of cosmic-ray acceleration, making their observation critical to identify the sources of high-energy cosmic rays. The observation of high-energy astrophysical neutrinos reported by the IceCube Collaboration in the last few years (see Chapter 1) represents a crucial step forward in the field of neutrino astronomy and strongly motivates independent searches for their origin. In this Chapter, the results of four different searches for astrophysical neutrino sources are presented. The first analysis is an update of the ANTARES standard point-like source search using 11 years of ANTARES data (Section 7.1). In the second search, the different characteristics of the ANTARES and the IceCube telescopes are exploited by combining data from both detectors to perform various searches for point-like and extended sources of neutrinos in the Southern Sky, improving the sensitivity compared to the individual analyses (Section 7.2). In the third search, the ANTARES data are scanned to search for time and space correlations with IceCube high-energy astrophysical neutrino candidates, in order to test for a possible transient origin of the IceCube events (Section 7.3). Finally, the last analysis provides the first estimation of the sensitivity of KM3NeT/ARCA

Phase 1 to point-like sources (Section 7.4).

7.1 Searches for point-like sources of cosmic neutrinos with 11 years of ANTARES data

In this Section, the results of various searches for point-like sources using 11 years of ANTARES data are presented. The analysis includes both track-like and shower-like events recorded in ANTARES between January 29, 2007 and December 31, 2017, for a total livetime of 3125.4 days. The selection criteria are described in Section 7.1.1. The search method is described in Section 7.1.2, while the results are presented in Section 7.1.3. The systematic uncertainties considered in the analysis are described in 7.1.4.

7.1.1 Data sample

The events are selected following the chain of cuts defined in the nine-year ANTARES point-source analysis [134]. The selection cuts were optimised to minimise the neutrino flux needed for a 5σ discovery of a point-like source emitting with a $E_\nu^{-2.0}$ spectrum. A summary of the selection criteria for tracks and showers follows.

Track selection. The selection of events induced by muon neutrinos is optimised using parameters provided by the AAFit track reconstruction algorithm (see Section 4.2.1). The overwhelming down-going background of atmospheric muons is removed by applying a cut on the reconstructed zenith angle ($\cos\theta_{tr} > -0.1$). Cuts are also applied on the estimated angular error ($\beta_{tr} < 1^\circ$) and the parameter that describes the quality of the reconstruction ($\Lambda > -5.2$) in order to increase both the quality and the purity of the neutrino sample. Further cuts are imposed on energy-related variables in order to guarantee the validity of the muon energy estimator employed in the analysis, ρ (defined in Equation 4.7). The energy estimator fails for events for which the muon energy is below the value of the critical energy to produce significant energy losses due to radiative processes (∼600 GeV in water and ∼500 GeV in rock), and for tracks with estimated track length, L_μ, below 380 m, yielding small values of ρ. For this reason, only events with $L_\mu > 380$ m and $\log_{10}(\rho) > 1.6$ are included in the analysis. A total of 8754 neutrino candidates are selected in the track channel, with an expected atmospheric muon contamination of 13%.

Shower selection. Only events not selected as tracks are considered in the shower channel. Showers are reconstructed with the TANTRA algorithm (see Section 4.2.2) and are selected if reconstructed as up-going or coming from close to the horizon ($\cos\theta_{sh} > -0.1$) with constraints on the angular error estimate ($\beta_{sh} < 30^\circ$) and on the interaction vertex, which is required to lie within a fiducial volume slightly larger than the instrumented volume. In particular, a cut on the radial distance of the reconstructed shower position from the vertical axis of the detector, $R_{sh} < 300$ m, and on the vertical distance above the center of the detector, $|Z_{sh}| < 250$ m, are applied. In order to further reduce the remaining background from mis-reconstructed atmospheric muons, additional selection cuts are applied on the TANTRA M-estimator and on the Dusj RDF (both defined in Section 4.2.2): $M_{\text{est}} < 1000$ and $RDF > 0.3$. Furthermore, a cut on an additional likelihood function, developed to discriminate between neutrinos that produce showers and the background of atmospheric muons, is applied. This likelihood only makes use of hits that coincide with another hit on the same storey within 20 ns. Its probability density function is based on the time residual t_{res} of the hits, the number N of on-time hits (-20 ns $< t_{\text{res}} < 60$ ns) and the distance d of the hits to the reconstructed shower position. The resulting likelihood is defined as

$$\mathscr{L}_\mu = \sum_{\text{Coinc.hits}} \log\{P_{\text{sig}}/P_{\text{bkg}}\}\,, \tag{7.1}$$

with $P_{\text{sig}} = P(N, d, t_{\text{res}}|\nu)$ and $P_{\text{bkg}} = P(N, d, t_{\text{res}}|\mu)$.

Only events with $\mathscr{L}_\mu > 50$ are selected. Overall, the selection yields a total of 195 neutrino candidates in the shower channel, with an estimated fraction of 43% of atmospheric muon contamination.

7.1.2 Search method

An extended maximum likelihood approach is employed to identify clusters of cosmic neutrinos from point-like sources over the background of randomly distributed atmospheric background. The used likelihood is defined as

$$\log\mathcal{L}(n_s, \alpha, \delta) = \sum_{\mathcal{J}\in\{tr,sh\}} \sum_{i\in\mathcal{J}} \log\left[n_s^{\mathcal{J}}\mathcal{S}_i^{\mathcal{J}}(n_s, \alpha, \delta) + \mathcal{N}^{\mathcal{J}}\mathcal{B}_i^{\mathcal{J}}\right] - n_s\,, \tag{7.2}$$

where n_s is the unknown total number of signal events, α and δ are the unknown equatorial coordinates of the source, $\mathcal{J}$ denotes the sample (tr for tracks, sh for showers), i indicates the event of the sample $\mathcal{J}$, $n_s^{\mathcal{J}}$ is the number of signal events fitted in the $\mathcal{J}$ sample, $\mathcal{N}^{\mathcal{J}}$ is the total number of events in the $\mathcal{J}$ sample, and $\mathcal{S}_i^{\mathcal{J}}$ and $\mathcal{B}_i^{\mathcal{J}}$ are the values of the signal and background PDFs for the event i in the sample $\mathcal{J}$.

The combined information of two parameters – direction and energy – is included in the definition of the PDFs in order to enhance the signal-to-background discrimination. Slightly different definitions of the PDFs are used in the track and in the shower channels. For each track-like event i, the probability of being reconstructed as signal or background is given by:

$$\mathcal{S}_i^{tr} = \mathcal{S}^{\text{space}}(\Delta\Psi_i, \beta_i|\gamma)\mathcal{S}^{\text{energy}}(\rho_i, \beta_i|\delta_i, \gamma)\,, \tag{7.3}$$

$$\mathcal{B}_i^{tr} = \mathcal{B}^{\text{space}}(\delta_i)\mathcal{B}^{\text{energy}}(\rho_i, \beta_i|\delta_i)\,. \tag{7.4}$$

As for the shower-like events, the probabilities are computed as

$$\mathcal{S}_i^{sh} = \mathcal{S}^{\text{space}}(\Delta\Psi_i|\gamma)\mathcal{S}^{\text{energy}}(N_i^{\text{hits}}|\gamma)\,, \tag{7.5}$$

$$\mathcal{B}_i^{sh} = \mathcal{B}^{\text{space}}(\delta_i)\mathcal{B}^{\text{energy}}(N_i^{\text{hits}})\,, \tag{7.6}$$

where:

- $\mathcal{S}^{\text{space}}$, the probability density function of reconstructing an ANTARES event i at a given angular distance $\Delta\Psi_i$ from the true source location, is given by the Point Spread Function. In the case of the track channel, the information of the event angular error estimate β_i is also included.
- $\mathcal{B}^{\text{space}}$ yields the probability density of reconstructing a background event at a certain declination δ_i.
- $\mathcal{S}^{\text{energy}}$ and $\mathcal{B}^{\text{energy}}$ give the probability density for a signal or background event to be reconstructed with a certain value of the energy related parameter (ρ for tracks, and the number of hits used by the reconstruction algorithm N^{hits} for showers). In the track channel, the information of the event angular error estimate β_i is also considered and the dependence of the energy estimator on the declination δ_i of the event is taken into account by generating both PDFs in steps of 0.2 in $\sin\delta$.

The number of signal events n_s is fitted in the likelihood maximization. Moreover, the position in the sky of the source is either kept fixed or allowed to be fitted within specific limits depending on the type of search (see Section 7.1.3).

7.1.3 Results

Four different searches for steady astrophysical neutrino sources are performed: a scan over the whole ANTARES visible sky, a survey of 111 astrophysical candidates, an investigation of 75 IceCube tracks, and a dedicated search at the location of the blazar TXS 0506+056. The results of these analyses are published in [61] and [135].

Full-Sky Search

In the full-sky search, an excess of signal events located anywhere in the ANTARES visible sky is searched for, without making any assumption about the source position. To this purpose, the TS-value (see Equation 6.13) is evaluated in steps of $1^\circ \times 1^\circ$ over the whole scanned region, with the location of the fitted cluster being left free to vary within these boundaries. The most significant cluster of this search, i.e. the cluster with lowest pre-trial p-value, is found at a right ascension of $\alpha = 343.7^\circ$ and a declination of $\delta = 23.6^\circ$ with a pre-trial p-value of 1.5×10^{-6}. The post-trial significance of the cluster is $23\,\%$, which corresponds to 1.2σ in the two-sided sigma convention. The same convention will be used hereafter for all the results. The distribution of ANTARES events around the best-fit location of the cluster is shown in Figure 7.1. It contains 18 (3) tracks within $5^\circ(1^\circ)$ and 1 shower event within 5°. Figure 7.2 shows the position of the cluster and the pre-trial p-values for all the directions in the ANTARES visible sky.

Candidate List Searches

Two candidate-list searches are performed: a search over 111 astrophysical objects and a search over 75 IceCube tracks.

Search over astrophysical objects. The list of the 111 analysed candidates contains the sources investigated in the nine-year ANTARES point-source analysis [134], updated with five new sources reported in the TeVCat catalog [136] and detected after January 2016. The list of the analysed candidates, together with the obtained results at each location, is reported in Table 7.1. The most signal-like

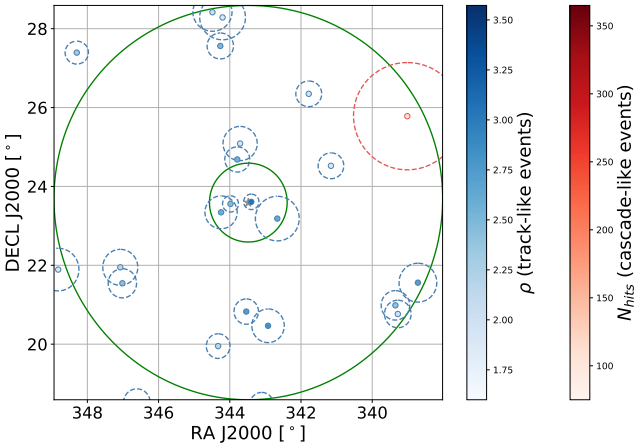

Figure 7.1: Distribution of events in the (α, δ) (RA, Dec) coordinates for the most significant cluster found in the full-sky search using 11 years of ANTARES data. The inner (outer) green line depicts the one (five) degree distance from the position of the best-fit location, indicated as a grey star. The red points denote shower-like events, whereas the blue points indicate track-like events. The dashed circles around the events indicate the angular error estimate. Different tones of red and blue correspond to the values assumed by the energy estimators: the number of hits (shower-like events) and the ρ parameter (track-like events) as shown in the legend.

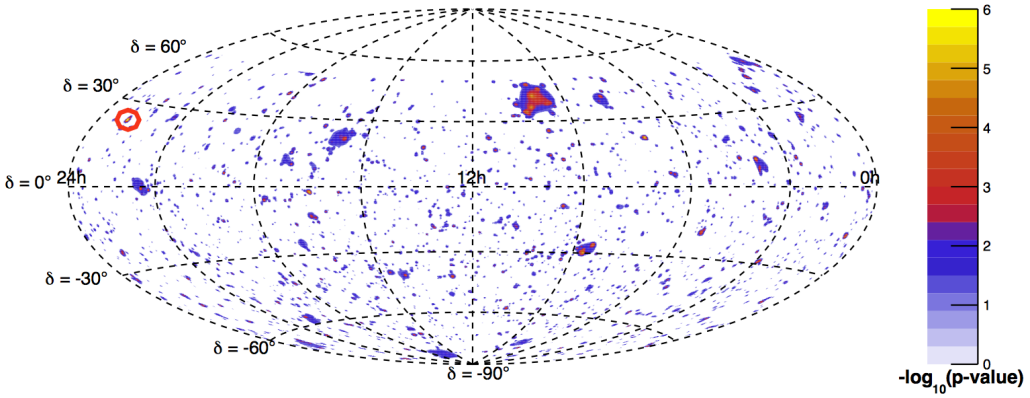

Figure 7.2: Sky map in equatorial coordinates of pre-trial p-values for a point-like source of the ANTARES visible sky. The red contour indicates the location of the most significant cluster of the full-sky search.

cluster is found at the location of HESS J0632+057, at equatorial coordinates $(\alpha, \delta) = (98.24°, 5.81°)$, with a pre-trial p-value of 0.15%, corresponding to a post-trial significance of 1.4σ. The cluster contains 11(1) tracks within $5°(1°)$ and 2 shower events within $5°$ around the source candidate, as shown in Figure 7.3. Figure 7.4-top shows the 90% CL limits on the one-flavour neutrino

flux normalisation for this search (assuming an $E_\nu^{-2.0}$ spectrum) as a function of the declination.

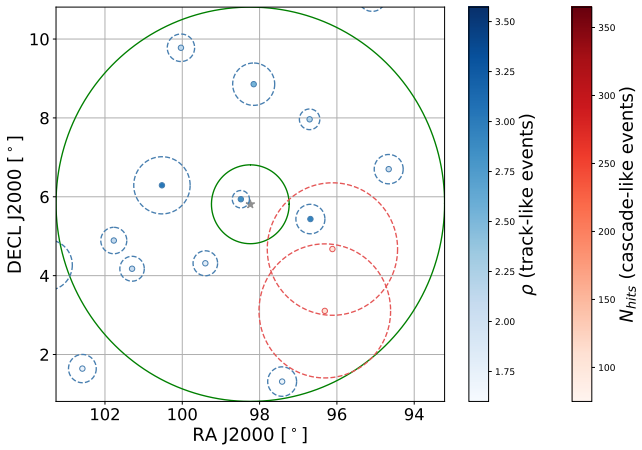

Figure 7.3: Distribution of events in the (α, δ) (RA, Dec) coordinates for the most significant cluster found in the candidate list search over astrophysical objects (HESSJ0632+057). Refer to caption of Figure 7.1 for details on the reported quantities.

Search over IceCube tracks. A total of 75 IceCube neutrino candidates classified as tracks are analysed in a separate candidate list search. In this case, given the non-negligible angular uncertainty of the IceCube candidates, the position in the sky of the fitted source is left free to vary around the position of the IceCube event within a cone with opening angle twice as large as its estimated angular error. The list of investigated candidates includes the 20 events from the HESE sample [46, 47, 48] and the 34 events from the Muon sample [50, 51] investigated in the ANTARES time-dependent search presented in Section 7.3. In addition, a total of 21 IceCube alerts (12 HESE [137] and 9 EHE [138]), distributed within the Astrophysical Multimessenger Observatory Network (AMON) framework [139, 140], are included. The list of investigated candidates is presented in Table 7.2. The value of the estimated angular error corresponds to the median angular error reported by the IceCube Collaboration in the case of the HESE and the AMON tracks. For events from the Muon sample, an estimation of the median angular uncertainty is derived from the angular errors on the equatorial coordinates provided by the IceCube Collaboration. This is done assuming that the median angular errors on the declination, δ, and the right ascension, α, follow independent Gaussian distributions with standard deviation given by the angular errors. The standard deviation of the two-dimensional Gaussian distribution, function of δ and α, is then employed as median angular uncertainty.

Table 7.1: List of analysed astrophysical objects. Reported are the source's name, equatorial coordinates, best-fit number of signal events, pre-trial p-value and 90% CL upper limits on the flux normalisation factor for a $E_\nu^{-2.0}$ spectrum, $\Phi^{90\%}_{E_\nu^{-2.0}}$ (in units of 10^{-8} GeV^{-1}cm^{-2}s^{-1}). Dashes (-) in the fitted number of source events and pre-trial p-value indicate sources with null observations.

Name	$\delta[^\circ]$	$\alpha[^\circ]$	$\hat{n}_s$	p-value	$\Phi^{90\%}_{E_\nu^{-2.0}}$	Name	$\delta[^\circ]$	$\alpha[^\circ]$	$\hat{n}_s$	p-value	$\Phi^{90\%}_{E_\nu^{-2.0}}$
LHA120-N-157B	-69.16	84.43	–	–	0.53	2HWCJ1309-054	-5.49	197.31	–	–	0.83
HESSJ1356-645	-64.50	209.00	0.2	0.67	0.75	3C279	-5.79	194.05	0.8	0.10	1.35
PSRB1259-63	-63.83	195.70	–	–	0.53	2HWCJ1852+013*	1.38	283.01	–	–	0.84
HESSJ1303-631	-63.20	195.75	–	–	0.55	W44	1.38	284.04	–	–	0.84
RCW86	-62.48	220.68	–	–	0.53	PKS0736+017	1.62	114.83	–	–	0.94
HESSJ1507-622	-62.34	226.72	–	–	0.53	RGBJ0152+017	1.79	28.17	–	–	0.84
HESSJ1458-608	-60.88	224.54	1.1	0.13	0.90	2HWCJ1902+048*	4.86	285.51	–	–	0.85
ESO139-G12	-59.94	264.41	–	–	0.59	SS433	4.98	287.96	–	–	0.85
MSH15-52	-59.16	228.53	–	–	0.54	HESSJ0632+057	5.81	98.24	2.7	0.0015	2.61
HESSJ1503-582	-58.74	226.46	–	–	0.54	MGROJ1908+06	6.27	286.99	–	–	0.85
HESSJ1023-575	-57.76	155.83	1.3	0.12	0.93	2HWCJ1829+070	7.03	277.34	–	–	0.85
CirX-1	-57.17	230.17	–	–	0.57	B1030+074	7.19	158.39	–	–	0.85
SNRG327.1-01.1	-55.08	238.65	–	–	0.58	2HWCJ1907+084*	8.50	286.79	–	–	0.87
HESSJ1614-518	-51.82	243.58	0.8	0.18	0.82	OT081	9.65	267.89	–	–	1.19
HESSJ1616-508	-50.97	243.97	0.6	0.18	0.81	HESSJ1912+101	10.15	288.21	–	–	0.86
PKS2005-489	-48.82	302.37	0.2	0.76	0.74	PKS1502+106	10.52	226.10	–	–	0.86
GX339-4	-48.79	255.70	–	–	0.55	RBS0723	11.56	131.80	–	–	0.86
HESSJ1632-478	-47.82	248.04	1.0	0.15	0.86	2HWCJ1914+117	11.72	288.68	–	–	0.86
RXJ0852.0-4622	-46.37	133.00	–	–	0.54	2HWCJ1921+131	13.13	290.30	–	–	0.86
HESSJ1641-463	-46.30	250.26	1.3	0.099	0.94	W51C	14.19	290.75	–	–	0.86
VelaX	-45.60	128.75	–	–	0.54	2HWCJ0700+143	14.32	105.12	–	–	1.24
PKS0537-441	-44.08	84.71	0.4	0.20	0.80	VERJ0648+152	15.27	102.20	–	–	1.23
CentaurusA	-43.02	201.36	–	–	0.56	2HWCJ0819+157	15.79	124.98	–	–	0.87
PKS1424-418	-42.10	216.98	1.0	0.13	0.88	3C454.3	16.15	343.50	–	–	0.88
1ES2322-409	-40.66	351.20	–	–	0.58	PKS0235+164	16.61	39.66	1.9	0.062	1.75
RXJ1713.7-3946	-39.75	258.25	–	–	0.60	Geminga	17.77	98.47	0.8	0.14	1.49
PKS1440-389	-39.14	220.99	2.8	0.0060	1.61	2HWCJ1928+177	17.78	292.15	–	–	0.90
PKS0426-380	-37.93	67.17	–	–	0.61	RGBJ2243+203	20.35	340.98	–	–	0.94
PKS1454-354	-35.67	224.36	1.2	0.097	1.13	VERJ0521+211	21.21	80.44	1.0	0.13	1.53
PKS0625-35	-35.49	96.78	–	–	0.64	4C+21.35	21.38	186.23	–	–	0.95
TXS1714-336	-33.70	259.40	0.8	0.10	1.11	Crab	22.01	83.63	–	–	1.29
SwiftJ1656.3-3302	-33.04	254.07	–	–	0.86	IC443	22.50	94.21	–	–	0.96
PKS0548-322	-32.27	87.67	–	–	0.69	S20109+22	22.74	18.02	–	–	0.97
H2356-309	-30.63	359.78	–	–	0.71	B1422+231	22.93	216.16	–	–	0.97
PKS2155-304	-30.22	329.72	–	–	0.70	PKS1424+240	23.79	216.75	–	–	0.98
HESSJ1741-302	-30.20	265.25	0.6	0.14	1.10	2HWCJ1938+238	23.81	294.74	–	–	0.98
PKS1622-297	-29.90	246.50	–	–	0.70	2HWCJ1949+244	24.46	297.42	–	–	1.16
Galactic Centre	-29.01	266.42	1.2	0.10	1.20	MS1221.8+2452	24.61	186.10	–	–	0.99
Terzan5	-24.90	266.95	–	–	0.93	PKS1441+25	25.03	220.99	–	–	1.00
1ES1101-232	-23.49	165.91	–	–	0.76	1ES0647+250	25.05	102.69	0.2	0.46	1.40
PKS0454-234	-23.43	74.27	–	–	0.75	S31227+25	25.30	187.56	–	–	1.00
W28	-23.34	270.43	0.8	0.096	1.27	WComae	28.23	185.38	–	–	1.04
PKS1830-211	-21.07	278.42	–	–	0.76	2HWCJ1955+285	28.59	298.83	–	–	1.04
SNRG015.4+00.1	-15.47	274.52	–	–	0.92	TON0599	29.24	179.88	–	–	1.05
LS5039	-14.83	276.56	–	–	1.04	2HWCJ1953+294	29.48	298.26	–	–	1.05
QSO1730-130	-13.10	263.30	–	–	0.80	1ES1215+303	30.10	184.45	–	–	1.06
HESSJ1826-130	-13.01	276.51	–	–	0.87	1ES1218+304	30.19	185.36	–	–	1.06
HESSJ1813-126	-12.68	273.34	–	–	0.80	HESSJ1746-308	30.84	266.57	–	–	1.07
1ES0347-121	-11.99	57.35	–	–	0.83	2HWCJ1040+308	30.87	160.22	–	–	1.19
PKS0727-11	-11.70	112.58	1.2	0.076	1.43	2HWCJ2006+341	34.18	301.55	–	–	1.10
HESSJ1828-099	-9.99	277.24	1.6	0.077	1.45	S30218+35	35.94	35.27	0.8	0.099	1.92
HESSJ1831-098	-9.90	277.85	–	–	0.81	MGROJ2019+37	36.83	304.64	0.5	0.15	1.73
HESSJ1834-087	-8.76	278.69	–	–	0.81	Milagro Diffuse	38.00	305.00	0.4	0.15	1.73
PKS1406-076	-7.90	212.20	–	–	0.82	Markarian421	38.19	166.08	–	–	1.22
QSO2022-077	-7.60	306.40	1.4	0.047	1.57	B32247+381	38.43	342.53	–	–	1.22
HESSJ1837-069	-6.95	279.41	–	–	0.93						

In this sample, a conservative minimum value of 1° for the angular uncertainty is assumed. The results in Table 7.2 show that the IceCube track candidate with the largest excess is the Muon event with ID 3. The fitted cluster is located at $(\hat{\alpha}, \hat{\delta}) = (343.7^\circ, 23.6^\circ)$, which is at a distance of 0.2° from the original Muon track at $(\alpha, \delta) = (343.55^\circ, 23.78^\circ)$, and coincident with the most significant cluster

found in the full-sky search (see Section 7.1.3). The trial-corrected significance of the source is 1.5% (2.4σ). Figure 7.4-bottom shows the 90% CL sensitivities and limits on the one-flavour neutrino flux normalisation from the investigated IceCube candidates as a function of the declination.

Table 7.2: List of analysed IceCube track events. Reported are the candidate's sample and ID, estimated angular error, and the results of the analysis (best-fit equatorial coordinates, best-fit number of signal events, pre-trial p-value and 90% CL upper limits on the one-flavour neutrino flux normalisation for an $E_\nu^{-2.0}$ spectrum, $\Phi^{90\%}_{E_\nu^{-2.0}}$ in units of 10^{-8} GeV^{-1}cm^{-2}s^{-1}). Dashes (-) in the fitted number of source events and pre-trial p-value indicate cases with null observations.

Sample	ID	β[°]	$\hat{\delta}$[°]	$\hat{\alpha}$[°]	$\hat{n}_s$	p-value	$\Phi^{90\%}_{E_\nu^{-2.0}}$	Sample	ID	β[°]	$\hat{\delta}$[°]	$\hat{\alpha}$[°]	$\hat{n}_s$	p-value	$\Phi^{90\%}_{E_\nu^{-2.0}}$
HESE	3	1.4	-29.9	130.1	6.6	0.000012	2.55		20	1.0	28.0	167.0	–	–	1.13
	5	1.2	1.5	112.7	2.8	0.032	1.15		21	1.0	14.5	91.2	1.0	0.029	1.49
	8	1.3	-22.0	184.0	2.2	0.020	1.06		22	1.0	-4.4	224.6	1.3	0.079	1.02
	13	1.2	41.7	67.5	–	–	1.37		23	1.0	9.2	32.5	0.5	0.16	1.00
	18	1.3	-23.4	346.5	1.8	0.0020	1.81		24	1.0	32.3	295.5	1.8	0.016	1.87
	23	1.9	-14.4	209.8	1.8	0.019	1.17		25	1.1	15.8	350.0	1.5	0.097	1.17
	28	1.3	-71.8	162.9	1.4	0.041	0.77		26	1.0	1.6	104.5	2.6	0.0030	2.12
	37	1.2	20.1	169.5	–	–	1.19		27	1.0	12.9	109.0	–	–	1.01
	43	1.2	-21.7	208.6	–	–	1.00		28	1.0	5.8	99.0	2.2	0.0098	1.74
	44	1.2	-1.4	336.3	1.0	0.037	1.03		29	1.0	12.2	91.0	–	–	1.01
	45	1.2	-85.2	241.4	1.9	0.011	0.87		30	1.0	25.6	324.0	1.0	0.13	1.11
	53	1.2	-35.9	240.5	2.9	0.0081	1.16		31	1.0	5.5	327.7	1.1	0.13	0.98
	58	1.3	-34.8	101.9	1.8	0.0052	1.42		32	1.0	29.0	136.0	0.8	0.098	1.09
	61	1.2	-18.6	56.5	1.3	0.062	0.96		33	1.5	18.4	200.5	1.2	0.0030	2.22
	62	1.3	11.4	188.2	0.8	0.083	1.16		34	1.0	11.1	76.2	–	–	1.01
	63	1.2	4.4	158.4	1.6	0.058	1.03		35	1.0	16.6	152.5	2.1	0.0047	2.09
	71	1.2	-18.9	81.2	4.4	0.00022	2.41	AMON HESE	766165_132518	1.3	-38.8	64.5	1.2	0.014	1.14
	76	1.2	0.0	238.5	0.6	0.12	1.12		66688965_132229	1.3	-15.9	266.6	1.5	0.060	0.99
	78	1.2	5.9	1.5	–	–	1.03		36142391_132143	1.3	-55.7	129.6	1.1	0.014	0.93
	82	1.2	7.9	243.0	1.7	0.046	1.12		9759013_132077	1.3	-33.5	305.1	1.3	0.012	1.16
Muon	1	1.0	2.4	28.0	–	–	0.95		68269692_131999	1.3	-23.4	2.0	1.0	0.039	0.98
	2	1.0	12.9	296.3	0.9	0.084	1.06		66412090_131680	1.3	-69.8	180.1	1.9	0.066	0.79
	3	1.1	23.8	343.5	5.0	0.0000015	3.87		56068624_130126	1.3	-17.5	162.5	2.2	0.0043	1.80
	5	1.0	20.0	309.0	–	–	1.09		32674593_129474	1.3	-27.9	223.0	1.7	0.029	0.99
	6	4.4	14.0	248.0	2.0	0.0025	1.65		65274589_129281	1.3	-26.3	307.9	2.0	0.010	1.35
	7	1.0	14.4	267.5	0.4	0.21	1.01		38561326_128672	1.1	11.3	39.5	2.1	0.010	2.78
	8	1.0	10.1	329.5	1.1	0.062	1.01		58537957_128340	1.5	-29.9	199.5	2.8	0.0037	1.52
	9	1.0	1.0	90.4	1.0	0.045	1.07		6888376_128290	1.3	-0.4	213.5	3.2	0.015	1.47
	10	1.0	4.0	285.1	0.9	0.055	1.04	AMON EHE	42419327_132508	1.0	6.4	118.5	–	–	1.05
	11	1.0	1.0	310.0	–	–	0.94		53411354_131653	1.0	-8.6	271.5	1.1	0.048	1.01
	12	1.0	21.6	234.7	2.3	0.00040	2.89		34507973_131475	1.0	-1.0	148.0	0.7	0.15	1.03
	13	1.0	35.1	273.0	0.7	0.11	1.22		17569642_130214	1.0	7.3	340.5	0.8	0.093	0.96
	14	2.1	4.6	317.0	2.8	0.0098	1.40		50579430_130033	1.0	5.8	77.5	1.1	0.018	1.51
	15	1.0	0.9	224.5	1.1	0.10	1.02		80305071_129307	1.0	-14.5	98.0	1.1	0.014	1.48
	16	1.0	18.5	37.5	1.4	0.10	1.07		80127519_128906	1.0	14.1	46.1	0.7	0.17	1.01
	17	1.0	33.0	200.4	–	–	1.14		26552458_128311	1.0	-2.0	123.7	2.0	0.0094	1.66
	18	1.0	1.2	328.2	1.3	0.088	1.02		6888376_128290	1.0	-0.2	213.4	3.2	0.016	1.44
	19	1.0	-1.4	204.5	1.3	0.018	1.42								

TXS 0506+056

A dedicated search for steady emission of neutrinos from the direction of the blazar TXS 0506+056, the first plausible cosmic source of high-energy neutrinos (see Section 1.4), is performed. A value of $\hat{n}_s = 1.03$ signal events is obtained from the maximisation at the position of the cluster, with a p-value of 3.4% (2.1σ), for an unbroken power-law spectrum $E_\nu^{-2.0}$. One track-like event mostly influences the fit (see Figure 7.5). It occurred on December 12, 2013 (outside the neutrino flare observed by IceCube) and is located within 1σ from the source position.

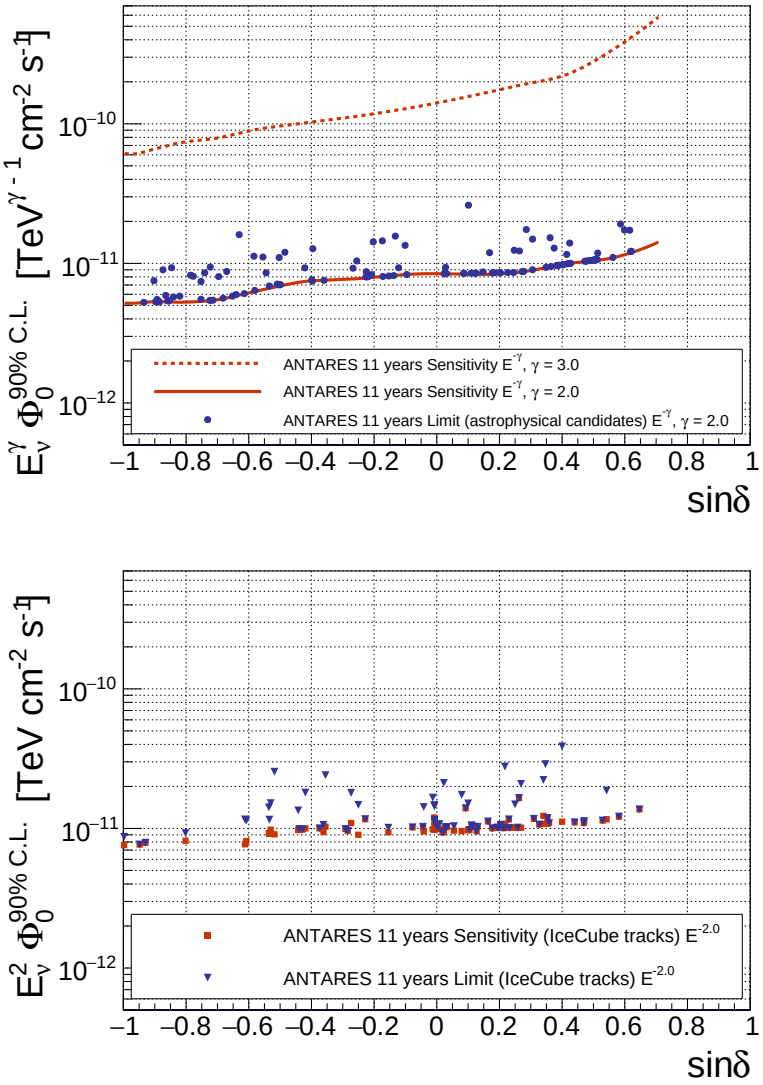

Figure 7.4: Top: $90\,\%$ CL upper limits on the signal flux from the investigated astrophysical candidates (blue dots) as a function of the source declination for an $E_\nu^{-2.0}$ spectrum. The red lines show the median sensitivity of this analysis for an $E_\nu^{-\gamma}$ spectrum, with $\gamma = 2.0$ (solid line) and $\gamma = 3.0$ (dashed line). Bottom: 90% CL upper limits (blue triangles) and sensitivities (red squares) for the investigated IceCube tracks as a function of the source declination for a $E_\nu^{-2.0}$ spectrum.

The value of the energy estimator ρ for this event is such that only 9% of the neutrino candidates inducing a track have a larger value. From these null results, 90% CL upper limits on the flux normalisation factor at the energy of 100 TeV, $\Phi^{90\%}_{100\ \mathrm{TeV}}$, assuming a steady neutrino source emitting with an unbroken power-law spectrum $E_\nu^{-2.0}(E_\nu^{-2.3})[E_\nu^{-2.5}]$, are set to $1.6(1.4)[1.0] \times 10^{-18}$ GeV^{-1} cm^{-2} s^{-1}.

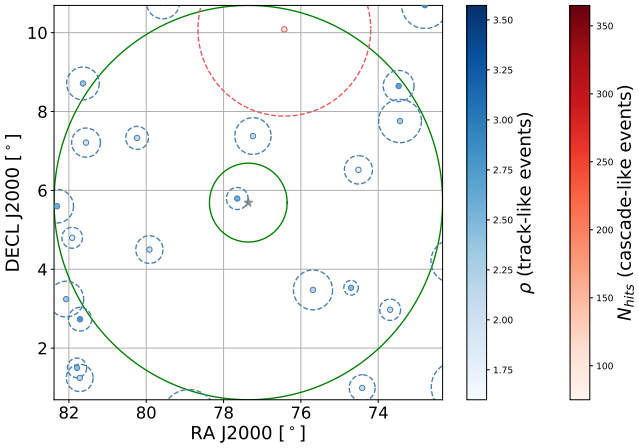

Figure 7.5: Distribution of events in the (α, δ) (RA, Dec) coordinates for the cluster at the location of TXS 0506+056. Refer to caption of Figure 7.1 for details on the reported quantities.

7.1.4 Systematic uncertainties

The effects of systematic uncertainties on the absolute pointing accuracy, angular resolution, acceptance and the background declination-dependent distribution of events have been considered in this analysis and are explained here.

Absolute Pointing Accuracy Uncertainty. A previous study [94] established an uncertainty on the horizontal (ϕ) and vertical (θ) directions of 0.13° and 0.06°, respectively. In order to account for this effect, random offsets, generated according to two Gaussian distributions with the aforementioned uncertainties as standard deviations, have been added to the ϕ and θ variables of the simulated events.

Angular Resolution Uncertainty. The accuracy of the detected hit times and of the recorded charges may affect the angular resolution of the reconstruction algorithm for tracks and showers, respectively. A smearing of the measured times and charges was performed in simulations leading to a degradation on the angular resolution of 15% in the track channel [131] and of 12% in the shower channel [141], both considered in this analysis.

Acceptance Uncertainty. A 15% uncertainty on the acceptance was estimated by performing simulations with a reduction of the efficiency of the optical modules by 15% [131], and has been considered for the calculation of the reported fluxes (see Equation 6.20).

Background Uncertainty. The declination-dependent distribution of the ANTARES

events selected in the 11-year point-like source search is shown in Figure 6.2, together with the two different spline functions, $P(\delta)$ and $O(\delta)$ (the purple and orange lines), used to parametrize the distribution. In order to account for possible systematic uncertainties on the background, a declination-dependent distribution defined as $\mathscr{B}(\delta) = P(\delta) + r \cdot (O(\delta) - P(\delta))$, with r being a random number drawn for each pseudo-experiment from a uniform distribution between -1 and 1, is used for the generation of the background events.

It is found that the $90\,\%$ C.L. sensitivity and the 5σ discovery potential would improve by less than $5\,\%$ if these uncertainties were not considered.

7.2 ANTARES and IceCube Combined Search for Neutrino Point-like and Extended Sources in the Southern Sky

In this Section a search for point-like and extended sources of cosmic neutrinos using the combined data collected by the ANTARES and IceCube neutrinos telescopes is presented. The two telescopes complement each other thanks to their different characteristics, in particular the larger instrumented volume of IceCube and the privileged view of the Southern Sky with a reduced muon background for neutrino energies below 100 TeV of ANTARES. Exploiting these different characteristics by combining data from both telescopes allows for a significant gain in sensitivity to neutrino sources in part of the Southern Sky. The data sample employed in the search is presented in Section 7.2.1. The analysis method and the expected performances are discussed in Section 7.2.2, while the searches and corresponding results are presented in Section 7.2.3. The results of this analysis are published in [142].

7.2.1 Data sample

The data sample employed in this search consists of all the track-like and shower-like events from the Southern Sky used in the nine-year ANTARES point-source analysis [134], combined with the through-going track-like events, i.e. tracks induced by muons traversing the detector, included in the seven-year IceCube point-source search [143]. The ANTARES data were collected between early 2007 and the end of 2015, while the IceCube data were taken from 2008 to 2015,

with the detector operating either in partial (samples IC40, IC59, IC79) or in full (samples IC86-2011, IC86-2012-2015) configuration.

The ANTARES events are selected by applying the cuts described in Section 7.1.1. The selection yields a total of 5807 tracks and 102 showers in the Southern Sky. The selection of IceCube through-going tracks in the Southern Sky is based on multivariate selection techniques (boosted decision trees, BDTs) to discriminate signal from the large background due to down-going atmospheric muons [143]. The BDT makes use of parameters connected to the event quality, track topology, deposited energy along the track, and light-arrival time of photons at the digital optical modules. The final event selection is also optimised to yield the best sensitivity and discovery potential for an $E_\nu^{-2.0}$ spectrum. This procedure selects only very high-energy events ($E_\nu \gtrsim 100$ TeV), yielding a total number of 325 969 events in the five samples. A summary of the data sets in terms of livetime and number of selected events in each sample is given in Table 7.3.

Table 7.3: Overview over the seven data samples of ANTARES and IceCube employed in the analysis. Only Southern-sky events (numbers of events reported in the last column) are selected for the present analysis.

ANTARES sample	Livetime [days]	Number of events
Tracks	2415	5807
Showers	2415	102
IceCube sample	**Livetime [days]**	**Number of events**
IC40	376	22779
IC59	348	64257
IC79	316	44771
IC86-2011	333	74931
IC86-2012-2015	1058	119231

Each sample has a different efficiency for detecting events from potential sources due to the different layouts, locations of the telescopes and selection techniques in the Southern Sky. The relative contribution of each sample $\mathcal{J}$, $C^{\mathcal{J}}(\delta, \frac{d\Phi_{1,\mathscr{F}}}{dE_\nu})$, depends on the source spectrum $\frac{d\Phi_{1,\mathscr{F}}}{dE_\nu}$ and declination δ, and is defined as the ratio of the expected mean number of signal events (defined in Equation 6.26) for each sample to that for all samples, $C^{\mathcal{J}} = \hat{\mu}_s^{\mathcal{J}} / \sum_{i=1}^{7} \hat{\mu}_s^i$.

The relative contribution of each sample as a function of the source declination for an unbroken $E_\nu^{-\gamma}$ spectrum for two values of the spectral index, $\gamma = 2.0$ and $\gamma = 2.5$, is shown in Figure 7.6. While for an $E_\nu^{-2.0}$ spectrum all samples contribute significantly to most of the Southern Sky, for a softer spectrum, the contribution

of high-energy neutrinos is lower, and therefore, the relative contribution of the ANTARES sample increases.

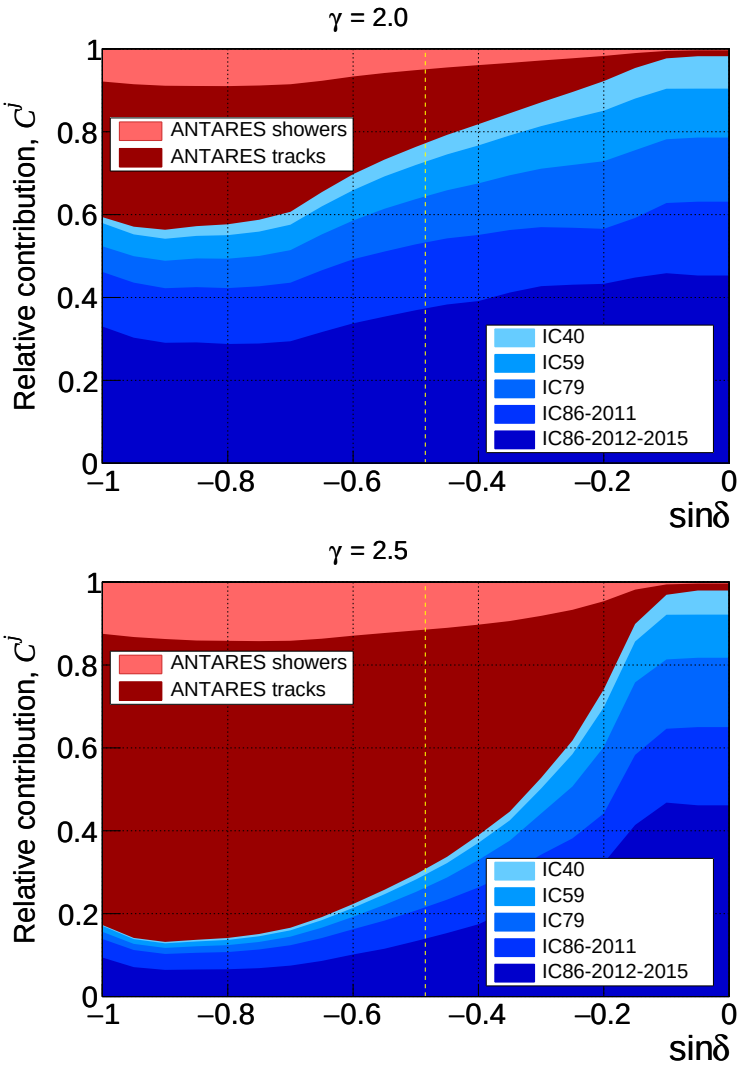

Figure 7.6: Relative contribution of each sample as a function of the source declination for an unbroken $E_\nu^{-\gamma}$ spectrum, with $\gamma = 2.0$ (top) and $\gamma = 2.5$ (bottom). The contribution of the ANTARES (IceCube) samples is represented by different shades of red (blue). The vertical dashed line marks the declination of the Galactic Centre.

7.2.2 Search method

The likelihood function used to identify clusters of cosmic neutrinos from point-like and extended sources over the randomly distributed atmospheric background is defined as

$$\mathcal{L}(n_s, \gamma, \alpha, \delta) = \prod_{\mathcal{J}=1}^{\mathcal{N}_{\rm samp}=7} \prod_{i=1}^{\mathcal{N}^{\mathcal{J}}} \left[\frac{n_s^{\mathcal{J}}}{\mathcal{N}^{\mathcal{J}}} \mathcal{S}_i^{\mathcal{J}}(\gamma, \alpha, \delta) + \left(1 - \frac{n_s^{\mathcal{J}}}{\mathcal{N}^{j}}\right) \mathcal{B}_i^{\mathcal{J}} \right], \tag{7.7}$$

where n_s and γ are respectively the unknown total number of signal events and signal spectral index, α and δ are the unknown equatorial coordinates of the source, $\mathcal{S}_i^{\mathcal{J}}$ and $\mathcal{B}_i^{\mathcal{J}}$ are the values of the signal and background PDFs for the event i in the sample $\mathcal{J}$, $\mathcal{N}_{\rm samp}$ is the total number of samples, $\mathcal{N}^{\mathcal{J}}$ is the total number of data events in sample $\mathcal{J}$, while $n_s^{\mathcal{J}}$ is the unknown number of signal events in sample $\mathcal{J}$, related to n_s through the relative contribution of the given sample, $n_s^{\mathcal{J}} = n_s \cdot C^{\mathcal{J}}(\delta, \frac{d\Phi_{1,\not{\mathcal{F}}}}{dE_\nu})$.

The same space and energy PDFs described in Section 7.1.2 are employed for the ANTARES samples. Similar definitions of the PDFs are used for the IceCube samples and correspond to those employed in the the seven-year IceCube point-source search [143]. The main difference between the ANTARES and the IceCube PDFs lies on the choice of the signal space PDF, $\mathcal{S}^{\rm space}$. For the IceCube samples, $\mathcal{S}^{\rm space}$ is given by a 2-dimensional Gaussian, $\mathcal{S}_{\rm IC}^{\rm space} = \exp(-\Delta\Psi_i^2/2\sigma_i^2)/(2\pi\sigma_i^2)$, with $\Delta\Psi_i$ being the angular distance of the event from the source, and σ_i being the angular error estimate of the event. When searching for spatially extended sources, the value of σ_i is replaced with $\sigma_{{\rm eff},i} = \sqrt{\sigma_i^2 + \sigma_{\rm s}^2}$, where $\sigma_{\rm s}$ is the extension of the source assuming a Gaussian profile. As for the ANTARES samples, the Point Spread Function (PSF) is employed as signal space PDF. In case of testing for extended sources, the PSF is built assuming that the original direction of the events is distributed according to a Gaussian profile around the source location with standard deviation given by the assumed source extension $\sigma_{\rm s}$.

In the likelihood maximisation, the number of signal events n_s and the signal spectral index γ are free parameters. The spectral index can range between 1.0 and 4.0, while the lower limit of n_s is set to 10^{-3}. Moreover, the position of the source is either kept fixed or fitted within specific limits depending on the type of search (see Section 7.2.3).

The potential of the combined search to discover a neutrino source is shown in Figure 7.7 in terms of 5σ discovery flux for an $E_\nu^{-\gamma}$ neutrino spectrum, with γ equal to 2.0 (upper panel) and 2.5 (lower panel), as a function of the declination. The discovery fluxes from the individual IceCube and ANTARES analyses are also shown.

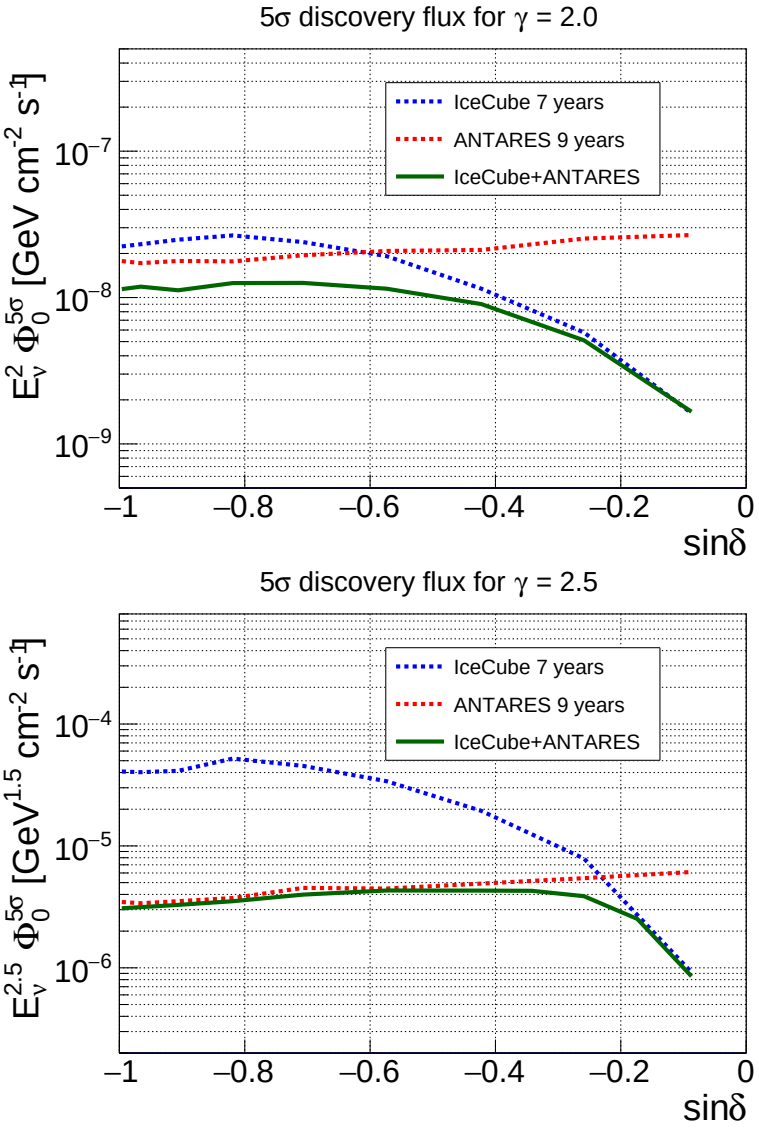

Figure 7.7: Point-source 5σ discovery fluxes for an unbroken $E_\nu^{-\gamma}$ neutrino spectrum, with $\gamma = 2.0$ (top) and $\gamma = 2.5$ (bottom). The green line indicates the results for the combined search. Blue and red curves show the results for the individual IceCube and ANTARES analyses, respectively.

7.2.3 Results

Five types of searches for point-like and extended sources are performed. In the first two strategies, a scan of the full Southern Sky and of a restricted region around the Galactic Centre (GC) are carried out. In the third approach, the directions of a pre-defined list of known sources which are potential neutrino emitters are investigated. Finally, two dedicated searches at the location of two promising neutrino source candidates, the super-massive black hole (SMBH) Sagittarius A*, and the shell-type supernova remnant (SNR) RX J1713.7-3946

are carried out.

Southern-sky search and Galactic Centre region search

In these searches, the most significant clustering with respect to the expected background is searched for at any position in a given region of the sky. The scanned region is divided into a grid with boxes of $1^\circ \times 1^\circ$ in right ascension and declination. The unbinned likelihood maximisation is performed in each box, with the source position being an additional parameter, free to vary inside the $1^\circ \times 1^\circ$ boundaries. For each box, the best-fit values of the number of signal events, $\hat{n}_s$, spectral index, $\hat{\gamma}$, and source equatorial coordinates, $\hat{\delta}$ and $\hat{\alpha}$, are found. The inspected region is scanned both for point-like ($\sigma_s = 0.0^\circ$) and extended sources ($\sigma_s = 0.5^\circ$, 1.0°, 2.0°).

In the first search, the scanned region is defined by the whole Southern Sky. The large number of probed directions in this case reduces the significance of weak sources due to a high trial factor. Motivated by the high concentration of candidate sources and gas around the GC and the recent discovery of an accelerator of PeV protons in the GC by the HESS Collaboration [28], a dedicated search is performed to investigate an a priori defined region around the GC. The examined region (depicted in Figure 7.8) is defined by an ellipse centred in the origin of the galactic coordinate system $(\alpha, \delta) = (266.40^\circ, -28.94^\circ)$, with a semi-minor axis of 15° in galactic latitude and a semi-major axis of 20° in galactic longitude.

Tables 7.4 and 7.5 report the results of the two searches. For each investigated region and source-extension hypothesis, the best-fit values of the parameters and the p-value of the most significant cluster are presented. The most significant result of the Southern-sky search is observed at equatorial coordinates $(\hat{\alpha}, \hat{\delta}) = (213.2^\circ, -40.8^\circ)$ for a point-like source hypothesis, with best-fit $\hat{n}_s = 5.7$ and $\hat{\gamma} = 2.5$. For this cluster, a pre-trial p-value of 1.3×10^{-5} is obtained. The corresponding post-trial significance (corrected for looking at multiple directions) is 18% (1.3σ). The map of pre-trial p-values for all the investigated directions for a point-like source hypothesis is shown in Figure 7.9. The position of the most significant cluster is also indicated.

The largest excess above background obtained in the search restricted to the Galactic Centre region is found for an extended source hypothesis ($\sigma_s = 2.0^\circ$) at equatorial coordinates $(\hat{\alpha}, \hat{\delta}) = (274.1^\circ, -40.1^\circ)$. The values of the best-fit $\hat{n}_s$

and $\hat{\gamma}$ are 20.3 and 3.0, respectively. The significance of the hotspot already corrected for looking at multiple directions (post-trial significance) is 3% (2.2σ). The pre-trial p-values for the investigated directions in the Galactic Centre region for an extended source hypothesis with $\sigma_s = 2.0°$ is shown in Figure 7.8, while Figure 7.10 presents the declination-dependent 90% CL upper limits on the one-flavour neutrino flux normalisation of this search for different source extensions.

Table 7.4: List of the most significant clusters found when performing the Southern-sky search for different source-extension hypotheses. Reported are the source extension σ_s, the best-fit parameters (number of signal events, $\hat{n}_s$, spectral index, $\hat{\gamma}$, declination, $\hat{\delta}$, right ascension, $\hat{\alpha}$), and the pre-trial and post-trial p-values.

$\sigma_s[°]$	$\hat{n}_s$	$\hat{\gamma}$	$\hat{\delta}[°]$	$\hat{\alpha}[°]$	pre-trial p-value	post-trial p-value
0.0	5.7	2.5	-40.8	213.2	1.3×10^{-5}	0.18
0.5	10.5	3.9	-22.5	18.5	3.4×10^{-5}	0.31
1.0	11.6	3.8	-21.9	18.4	8.9×10^{-5}	0.44
2.0	20.3	3.0	-40.1	274.1	2.2×10^{-4}	0.47

Table 7.5: List of the most significant clusters found when performing the search in the Galactic Centre region for different source-extension hypotheses. Reported are the source extension σ_s, the best-fit parameters (number of signal events, $\hat{n}_s$, spectral index, $\hat{\gamma}$, declination, $\hat{\delta}$, right ascension, $\hat{\alpha}$), and the pre-trial and post-trial p-values.

$\sigma_s[°]$	$\hat{n}_s$	$\hat{\gamma}$	$\hat{\delta}[°]$	$\hat{\alpha}[°]$	pre-trial p-value	post-trial p-value
0.0	6.8	2.8	-42.3	273.0	7.3×10^{-4}	0.40
0.5	8.4	2.8	-42.0	273.1	5.2×10^{-4}	0.19
1.0	12.1	2.9	-41.8	274.1	6.9×10^{-4}	0.15
2.0	20.3	3.0	-40.1	274.1	2.2×10^{-4}	0.03

Candidate list search

A total of 57 neutrino source candidates are investigated in the candidate list search in order to look for a possible point-like source emission of cosmic neutrinos. The candidates are sources of high-energy γ-rays belonging to different classes and selected from the TeVCat catalog [136]. The analysed candidates correspond to all the sources in the Southern Sky considered in the candidate list search performed using nine years of ANTARES data [134] and the Southern-sky candidates considered in the seven year IceCube candidate list search [143]. As the direction of the selected sources is known, only the number of signal events

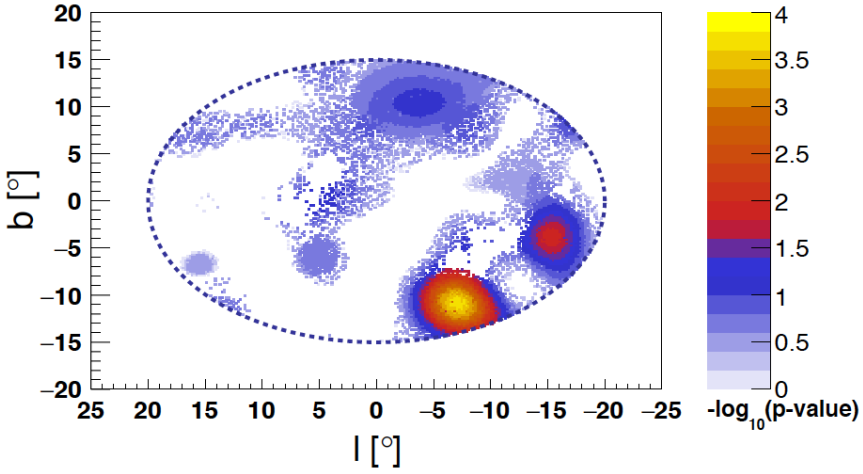

Figure 7.8: Sky map in galactic coordinates of the pre-trial p-values obtained in the Galactic Centre search for the extended source hypothesis with $\sigma_s = 2.0°$. The dashed line depicts the boundary of the search area.

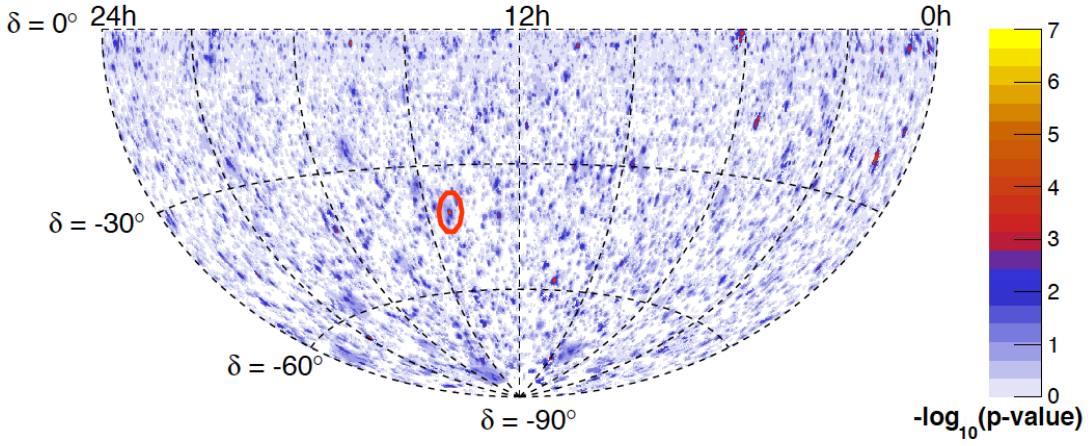

Figure 7.9: Sky map in equatorial coordinates of the pre-trial p-values obtained in the Southern-sky search for the point-like source hypothesis. The red contour indicates the location of the most significant cluster.

and the spectral index are left as free parameters in the likelihood maximisation. Table 7.6 presents the list of the astronomical candidates together with their equatorial coordinates, fitted number of signal events, fitted spectral index, pre-trial p-value, and 90% CL upper limits on the one-flavour neutrino flux normalisation for an $E_\nu^{-2.0}$ and an $E_\nu^{-2.5}$ spectrum. The 90% CL upper limits as a function of the source declination together with the sensitivity are shown in Figure 7.11.

The candidate HESSJ1023-575, a TeV γ-ray source coincident with the young

Table 7.6: List of astrophysical objects analysed in the candidate list search. Reported are the source's name, equatorial coordinates, best-fit values of the free parameters, pre-trial p-value and 90% CL upper limits on the flux normalisation factor for an $E_\nu^{-2.0}$ spectrum, $\Phi^{90\%}_{E_\nu^{-2.0}}$ (in units of 10^{-9} GeV^{-1}cm^{-2}s^{-1}), and for an $E_\nu^{-2.5}$ spectrum, $\Phi^{90\%}_{E_\nu^{-2.5}}$ (in units of 10^{-6} GeV^{-1}cm^{-2}s^{-1}). Dashes (-) in the fitted number of source events, spectral index and pre-trial p-value indicate sources with null observations ($\hat{n}_s = 0.001$).

Name	δ[°]	α[°]	$\hat{n}_s$	$\hat{\gamma}$	p-value	$\Phi^{90\%}_{E_\nu^{-2.0}}$	$\Phi^{90\%}_{E_\nu^{-2.5}}$
LHA120-N-157B	-69.16	84.43	-	-	-	3.6	0.9
HESSJ1356-645	-64.50	209.00	1.2	3.1	0.18	6.2	1.4
PSRB1259-63	-63.83	195.70	1.3	4.0	0.19	6.2	1.5
HESSJ1303-631	-63.20	195.74	-	-	-	3.7	0.9
RCW86	-62.48	220.68	1.0	1.6	0.20	6.3	1.5
HESSJ1507-622	-62.34	226.72	-	-	-	3.7	1.0
HESSJ1458-608	-60.88	224.54	3.7	3.6	0.036	9.3	2.0
ESO139-G12	-59.94	264.41	-	-	-	3.7	1.0
MSH15-52	-59.16	228.53	-	-	-	3.7	1.0
HESSJ1503-582	-58.74	226.46	-	-	-	3.7	1.0
HESSJ1023-575	-57.76	155.83	6.4	3.5	0.0079	11.2	2.5
CirX-1	-57.17	230.17	-	-	-	3.8	1.0
SNRG327.1-01.1	-55.08	238.65	-	-	-	3.8	1.0
HESSJ1614-518	-51.82	243.58	1.6	4.0	0.21	6.1	1.6
HESSJ1616-508	-50.97	243.97	2.0	2.0	0.18	6.5	1.6
PKS2005-489	-48.82	302.37	0.4	2.9	0.18	6.4	1.6
GX339-4	-48.79	255.70	-	-	-	3.7	1.1
HESSJ1632-478	-47.82	248.04	-	-	-	3.7	1.1
RXJ0852.0-4622	-46.37	133.00	-	-	-	3.7	1.1
HESSJ1641-463	-46.30	250.26	-	-	-	3.7	1.1
VelaX	-45.60	128.75	-	-	-	3.6	1.1
PKS0537-441	-44.08	84.71	1.6	2.2	0.098	7.2	1.9
CentaurusA	-43.02	201.36	-	-	-	3.6	1.1
PKS1424-418	-42.10	216.98	0.6	2.3	0.24	5.5	1.6
RXJ1713.7-3946	-39.75	258.25	-	-	-	3.5	1.2
PKS1440-389	-39.14	220.99	3.0	2.4	0.0085	10.8	3.0
PKS0426-380	-37.93	67.17	-	-	-	3.5	1.2
PKS1454-354	-35.67	224.36	3.9	2.1	0.089	7.3	2.1
PKS0625-35	-35.49	96.78	-	-	-	3.4	1.2
TXS1714-336	-33.70	259.40	1.2	2.3	0.17	5.9	1.9
SwiftJ1656.3-3302	-33.04	254.07	2.8	2.1	0.15	6.1	1.9
PKS0548-322	-32.27	87.67	-	-	-	3.2	1.2
H2356-309	-30.63	359.78	-	-	-	3.0	1.2
PKS2155-304	-30.22	329.72	-	-	-	3.0	1.2
HESSJ1741-302	-30.20	265.25	1.0	2.9	0.12	6.0	2.0
PKS1622-297	-29.90	246.50	4.4	1.9	0.048	7.4	2.4
Sagittarius A*	-29.01	266.42	2.9	2.1	0.06	7.2	2.4
Terzan5	-24.90	266.95	-	-	-	2.5	1.2
1ES1101-232	-23.49	165.91	-	-	-	2.4	1.2
PKS0454-234	-23.43	74.27	-	-	-	2.4	1.2
W28	-23.34	270.43	1.7	2.5	0.094	4.9	2.0
PKS1830-211	-21.07	278.42	-	-	-	2.2	1.2
NRG015.4+00.1	-15.47	274.52	-	-	-	1.6	1.0
LS5039	-14.83	276.56	-	-	-	1.5	1.0
QSO1730-130	-13.10	263.30	-	-	-	1.3	0.9
HESSJ1826-130	-13.01	276.51	-	-	-	1.3	0.8
HESSJ1813-126	-12.68	273.34	-	-	-	1.3	0.8
1ES0347-121	-11.99	57.35	-	-	-	1.2	0.8
PKS0727-11	-11.70	112.58	2.5	2.7	0.13	2.1	1.2
HESSJ1828-099	-9.99	277.24	2.4	2.9	0.079	2.0	1.2
HESSJ1831-098	-9.90	277.85	-	-	-	0.9	0.6
HESSJ1834-087	-8.76	278.69	-	-	-	0.8	0.5
PKS1406-076	-7.90	212.20	6.8	2.7	0.11	1.5	0.7
QSO2022-077	-7.60	306.40	-	-	-	0.7	0.4
HESSJ1837-069	-6.95	279.41	2.5	3.4	0.24	1.0	0.5
2HWCJ1309-054	-5.49	197.31	9.1	3.2	0.051	0.9	0.3
3C279	-5.79	194.05	2.5	2.2	0.28	0.6	0.3

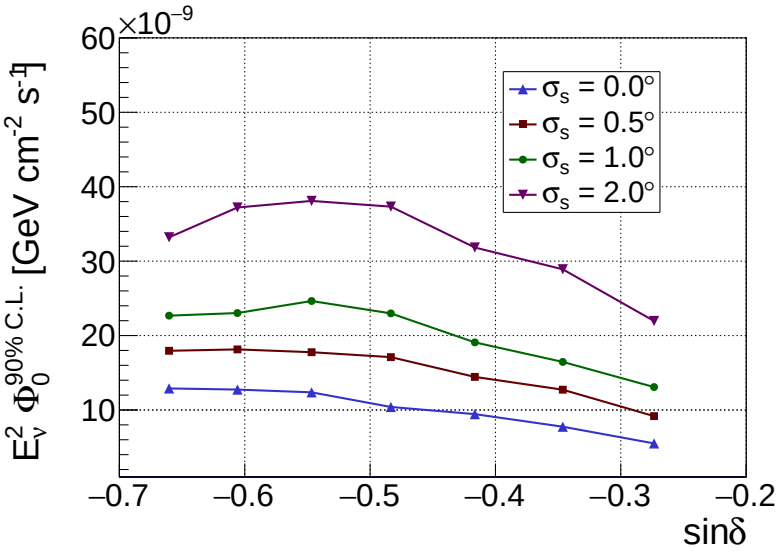

Figure 7.10: 90% CL upper limits on the one-flavour neutrino flux normalisation of the Galactic Centre region search assuming an $E_\nu^{-2.0}$ spectrum for different source extensions σ_s.

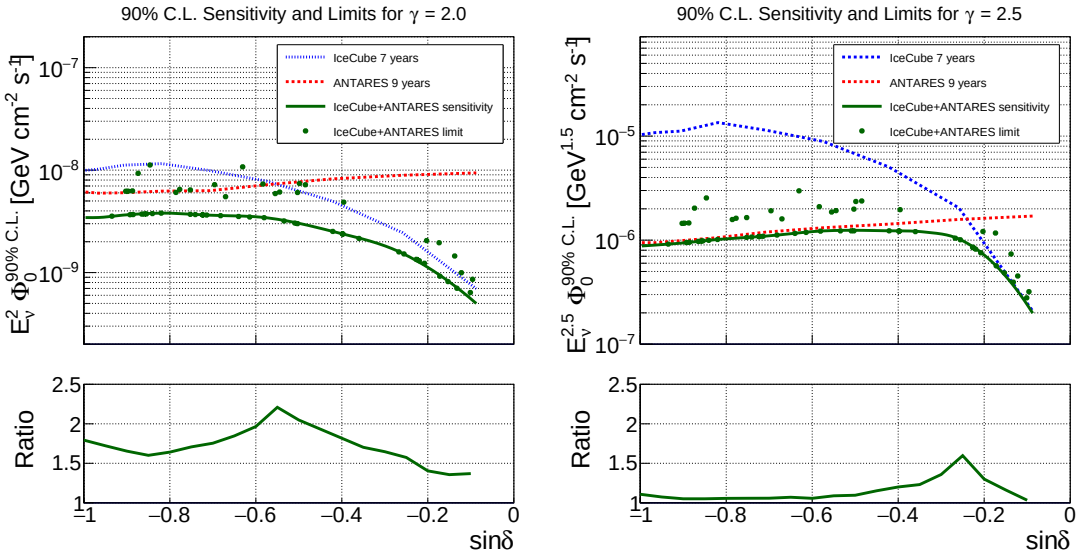

Figure 7.11: Upper limits at 90% CL on the one-flavour neutrino flux normalisation from the analysed candidates (green dots). An unbroken $E_\nu^{-\gamma}$ neutrino spectrum is assumed, with $\gamma = 2.0$ (left) and $\gamma = 2.5$ (right). The green line indicates the sensitivity of the combined analysis. The dashed curves indicate the sensitivities for the IceCube (blue) and ANTARES (red) individual analyses. Below each plot, the ratio between the best individual sensitivity and the combined sensitivity as a function of the source declination is shown.

stellar cluster Westerlund 2 [144], is the most significant source of the list, with a pre-trial p-value of 0.79%, corresponding to a trial-corrected significance of 42% (0.8σ). A total of 6.4 signal events and a spectral index of 3.5 are fitted

for the cluster at the position of HESSJ1023-575. The second and third most significant sources are PKS1440-389 and HESSJ1458-608 with a p-value of 0.85% and 3.6%, respectively.

Sagittarius A*

Since the surroundings of super massive black holes are highly plausible acceleration sites of very-high-energy CRs ($E \gtrsim 1$ EeV), and therefore, possible sources of cosmic neutrinos (see Chapter 1), Sagittarius A*, the SMBH located at the centre of our Galaxy, $(\alpha, \delta) = (266.42°, -29.01°)$, is a candidate source of particular interest. Given the high density of candidate objects around the Galactic Centre, the detection of an extended source is more likely than the detection of a point-like source. For these reasons, a search for astrophysical neutrinos from Sagittarius A* and nearby objects is carried out by testing the point-like ($\sigma_s = 0.0°$) and extended source ($\sigma_s = 0.5°$, $1.0°$, $2.0°$) hypotheses. Table 7.7 presents the result of the search at the investigated location in terms of best-fit parameters for the various tested source extensions together with the observed p-value. The largest excess above the background is found for a point-like source hypothesis, with best-fit values $\hat{n}_s = 2.9$ and $\hat{\gamma} = 2.1$, and a significance of 6% (1.9σ). Figure 7.12 shows the 90% CL upper limits as a function of the source extension together with the sensitivity and the discovery flux. The performances of the extended-source analysis are compared to the point-source hypothesis. In the former case the same value of the extension used to simulate the source enters the likelihood calculation, while in the latter, no extension is used in the likelihood PDFs, irrespective of the simulated spatial extension of the injected signal. The results show that, when the proper source width is used in the likelihood, a considerable improvement is achieved, especially for larger extensions.

Table 7.7: Values of the best-fit parameters (number of signal events, $\hat{n}_s$, and spectral index, $\hat{\gamma}$) and p-value for the search at the location of Sagittarius A* for different hypotheses of source extension σ_s. Dashes (-) in the fitted number of source events, spectral index and p-value indicate cases of null observations ($\hat{n}_s = 0.001$).

$\sigma_s[°]$	$\hat{n}_s$	$\hat{\gamma}$	p-value
0.0	2.9	2.1	0.06
0.5	0.6	2.0	0.26
1.0	-	-	-
2.0	0.3	3.8	0.40

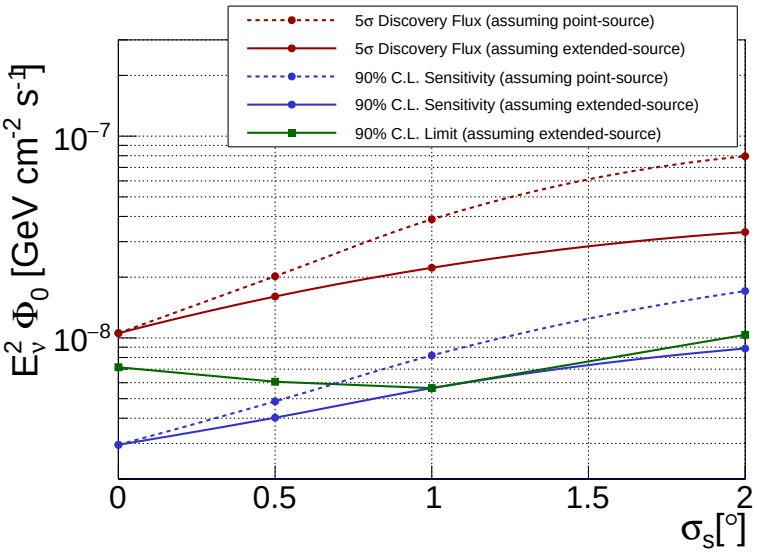

Figure 7.12: Discovery flux (solid red), sensitivity (solid blue) and 90% CL upper limits (solid green) for the search at the location of Sagittarius A* assuming an $E_\nu^{-2.0}$ spectrum as a function of the angular extension σ_s. The results for the point-like source hypothesis are shown as dashed lines.

RX J1713.7-3946

The shell-type supernova remnant RX J1713.7–3946, at equatorial coordinates $(\alpha, \delta) = (258.25°, -39.75°)$, is the brightest object of this kind in the TeV γ-ray sky and represents a particularly interesting target to the search for cosmic neutrinos (see Chapter 1). A dedicated search for astrophysical neutrinos, using specific energy spectra, from the direction of RX J1713.7–3946 is performed. Two models for the neutrino emission are tested: the model proposed by Kappes et al. [19], in the following indicated as RX J1713.7-3946 (1), and the one recently introduced for KM3NeT neutrino source search estimations [145] and based on the methods described by Vissani et al. [27, 146, 147], hereafter referred to as RX J1713.7-3946 (2). Both models describe a neutrino spectrum of the form of

$$\frac{d\Phi_{1\mathscr{F}}}{dE_\nu} = \Phi_0 \left(\frac{E_\nu}{1\,\mathrm{TeV}}\right)^{-\Gamma} \exp\left(-(E_\nu/E_{\mathrm{cut}})^\beta\right), \tag{7.8}$$

where E_ν is the neutrino energy and the values of the neutrino spectrum parameters Φ_0, Γ, E_{cut}, and β are listed in Table 7.8. A Gaussian extension of $\sigma_{\mathrm{s}} = 0.6°$ is assumed for the source as reported by the γ-ray analysis performed by the H.E.S.S. Collaboration [148].

No significant evidence of cosmic neutrinos from the direction of the SNR is

observed for either of the considered spectra. Table 7.8 presents the fitted number of signal events and the p-value observed at the source position for each spectrum hypothesis, together with the 90% CL sensitivity and upper limit, both expressed as ratio with the theoretical source flux.

Table 7.8: List of considered neutrino emission models for the search at the location of RX J1713.7–3946 and respective results. For each model, the values of the neutrino spectrum parameters, Φ_0 (in units of $10^{-11}\mathrm{TeV}^{-1}\mathrm{cm}^{-2}\mathrm{s}^{-1}$), Γ, E_{cut} (in units of TeV) and β, entering Equation 7.8 are provided. The last four columns show the results in terms of best-fit number of signal events, $\hat{n}_{\mathrm{s}}$, p-value, ratio of the sensitivity to the assumed source flux, $\Phi_{\mathrm{sens}}^{90\%\mathrm{CL}}/\Phi_0$, and ratio of the upper limit to the assumed source flux, $\Phi_{\mathrm{UL}}^{90\%\mathrm{CL}}/\Phi_0$.

Spectrum	Φ_0	Γ	E_{cut}	β	$\hat{n}_{\mathrm{s}}$	p-value	$\Phi_{\mathrm{sens}}^{90\%\mathrm{CL}}/\Phi_0$	$\Phi_{\mathrm{UL}}^{90\%\mathrm{CL}}/\Phi_0$
RX J1713.7-3946 (1)	1.55	1.72	1.35	0.5	0.3	0.40	10.7	13.2
RX J1713.7-3946 (2)	0.89	2.06	8.04	1	0.3	0.41	9.7	11.7

7.3 ANTARES neutrino search for time and space correlations with IceCube high-energy neutrino events

As reported in Chapter 1, a high-energy neutrino detected by IceCube was found to be positionally coincident with the direction of a known blazar, TXS 0506+056, in a state of enhanced activity observed in γ-rays and at other wavelengths of the electromagnetic spectrum. Moreover, an a posteriori time-variability study of the neutrino emission revealed a flare that occurred in 2014/2015. Despite this compelling evidence for the first identification of a neutrino source, the origin of most of the observed flux of astrophysical neutrinos detected by IceCube remains uncertain. Two spatially compatible events from the HESE sample were observed with a time difference of less than one day, with a p-value of 1.6% [149], which could be interpreted as the signature of another flaring source. All these results reinforce the motivation of a time correlation study between ANTARES and IceCube events. Such a correlation would support the hypothesis of the IceCube events being originated from flaring episodes.

In the analysis presented in this Section, a possible transient origin of 54 IceCube high-energy astrophysical neutrino candidates, selected from the HESE and the Muon samples (see Section 1.4), is searched for using neutrino events detected with the ANTARES telescope. The analysis includes both track-like and shower-like events recorded in ANTARES between 01/12/2008 and 31/12/2016 for a total

livetime of 2346 days, which matches the whole considered IceCube observation time (6 years and 8 years for the HESE and Muon samples, respectively). The ANTARES events are selected by applying the cuts described in Section 7.1.1. The selection yields a total of 6894 tracks and 160 showers. The IceCube neutrino candidates investigated in this analysis are described in Section 7.3.1. In Section 7.3.2 the search method is explained and in Section 7.3.3 the results of the search are reported. The results of this analysis are published in [150].

7.3.1 IceCube neutrino candidates

A total of 54 candidate cosmic neutrino events are selected from the IceCube HESE and Muon samples and treated as potential transient neutrino sources. Only events classified as muon tracks, lying within the ANTARES field-of-view and provided with an angular error, are included in the list. In case of events that are present in both samples, only the one with the smallest angular uncertainty is considered. The equatorial coordinates, observation time, and median angular error of the selected HESE candidates with ID 1 to 37 are taken from [46], ID 38 to 54 from [47] and ID 55 to 82 from [48]; Muon events with ID 1 to 29 are taken from [50] and ID 30 to 36 from [51]. All information is reported in Tables 7.9 and 7.10. The angular uncertainties correspond to the median angular errors reported by the IceCube Collaboration in the case of the HESE sample, while they are calculated as explained in Section 7.1.3 for the Muon sample.

7.3.2 Search method

In contrast to time-integrated searches, the information of the neutrino arrival times is exploited to enhance the discovery potential. Indeed, when dealing with transient emissions, the background of atmospheric neutrinos can be significantly reduced by limiting the search to a small time window around the source flare. In this analysis, an extended maximum likelihood approach is employed to investigate the directions of the 54 IceCube candidates searching for spatial and temporal clustering of events detected with ANTARES above the expected background.

The extended likelihood is defined as:

$$\begin{aligned}&\log \mathcal{L}(n_s, \gamma, \sigma_t, \alpha, \delta) \\ &= \sum_{\mathcal{J}\in\{tr,sh\}} \sum_{i\in\mathcal{J}} \log\left[n_s^{\mathcal{J}} \mathcal{S}_i^{\mathcal{J}}(\gamma, \sigma_t, \alpha, \delta) + \mathcal{N}^{\mathcal{J}} \mathcal{B}_i^{\mathcal{J}}\right] - n_s\,,\end{aligned} \tag{7.9}$$

where n_s, γ, σ_t, α and δ are the unknown parameters: the total number of signal events, the source spectral index, the flare duration, and the source equatorial coordinates. $\mathcal{S}_i^{\mathcal{J}}$ and $\mathcal{B}_i^{\mathcal{J}}$ are the values of the signal and background PDFs for the event i in the sample $\mathcal{J}$ (tr for tracks, sh for showers), while $n_s^{\mathcal{J}}$ and $\mathcal{N}^{\mathcal{J}}$ are respectively the number of unknown signal events and the total number of data events in the $\mathcal{J}$ sample.

The signal and background PDFs are given by the product of the directional and the energy terms described in Section 7.1.2, with the addition of a time-dependent term for the signal, $\mathcal{S}^{\text{time}}$, and for the background, $\mathcal{B}^{\text{time}}$, with the following definition:

- $\mathcal{S}^{\text{time}}$ is the signal time-dependent PDF. In this analysis, a generic Gaussian time profile for the signal emission is assumed, $\mathcal{S}^{\text{time}}(t_i) = \exp(-(\text{t}_\text{i} - \text{t}_\text{IC})^2)/2\sigma_\text{t}^2)/(\sqrt{2\pi}\sigma_\text{t})$, with t_i being the detection time of the ANTARES event i, t_{IC} the observation time of the considered IceCube candidate, and σ_t a proxy of the flare duration, fitted in the likelihood maximisation.
- $\mathcal{B}^{\text{time}}$ describes the probability to observe a background event at a given time t_i, and it is derived from the observed data. In order to reduce statistical fluctuations, this PDF is computed applying looser selection criteria than those of the final sample. Different selection cuts are not expected to modify the shape of this PDF.

At the position of each IceCube event, the likelihood of Equation 7.9 is maximised leaving as free parameters the number of signal events $n_s = n_s^{tr} + n_s^{sh}$, the signal spectral index γ and the flare duration σ_t, providing the best-fit values $\hat{n}_s$, $\hat{\gamma}$, $\hat{\sigma}_t$ for each investigated source. Moreover, the position in the sky of the fitted source is left free to vary around the position of the IceCube event within a cone with opening angle twice as large as its angular uncertainty. Only values of $n_s \geq 10^{-3}$ are allowed in the maximisation. The value of the spectral index ranges between 1.5 and 3.5, while values between 0.1 and 120 days are allowed for the flare duration. The lowest precision of the observation time of the IceCube

candidates provided by the IceCube Collaboration sets the lower bound to 0.1 days, while the choice of 120 days as upper bound is imposed by the fact that the time distance between the last recorded IceCube candidate (HESE ID 82) and the last ANTARES available fully-calibrated data is ∼240 days, i.e. twice the Gaussian standard deviation σ_t. Thus, more than 95% of the signal events from a Gaussian flare with $\sigma_t = 120$ days and centered at the observation time of HESE ID 82 could be detected within the considered ANTARES data taking period.

In order to estimate the performance of the search, the 5σ discovery potential is calculated for different durations of the simulated flare. Figure 7.13 shows the 5σ discovery potential in terms of mean number of signal events for the direction of the IceCube event HESE ID 3, for an $E_\nu^{-\gamma}$ neutrino spectrum, with γ equal to 2.0 or 2.5. In the case of signal emission lasting a few hours, the number of events needed for a 5σ discovery is reduced by a factor ∼3 (depending on the assumed source spectrum) with respect to a time integrated analysis. Similar levels of improvement in the discovery potential are expected for all the IceCube candidates.

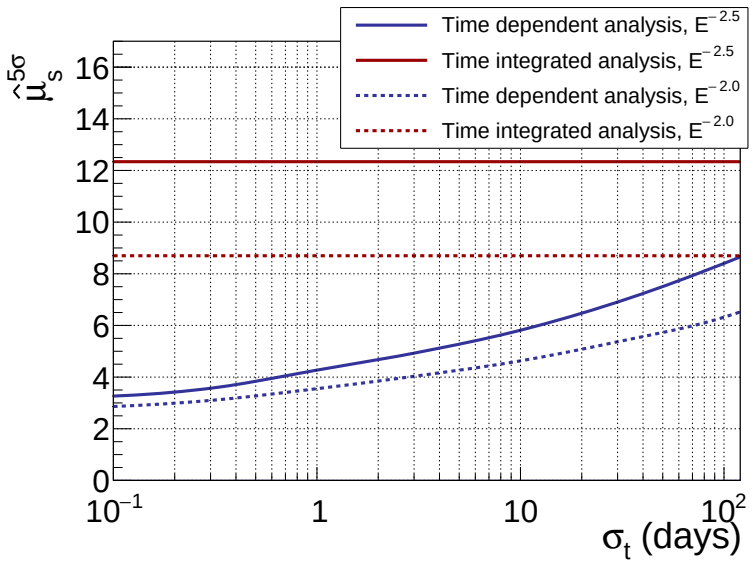

Figure 7.13: Mean number of signal events needed for a 5σ discovery in 50% of PEs for the ID 3 event of the IceCube HESE sample as a function of the flare duration σ_t. The result is shown for two assumptions of the energy spectrum: $E_\nu^{-2.5}$ (solid blue) and $E_\nu^{-2.0}$ (dotted blue). For comparison, the discovery potential of the time integrated analysis is also reported (red lines).

7.3.3 Results

No significant excess over the expected background is observed for any of the investigated IceCube candidate location. Figure 7.14 shows the positions of the ANTARES tracks and showers together with the directions of the 54 IceCube candidates.

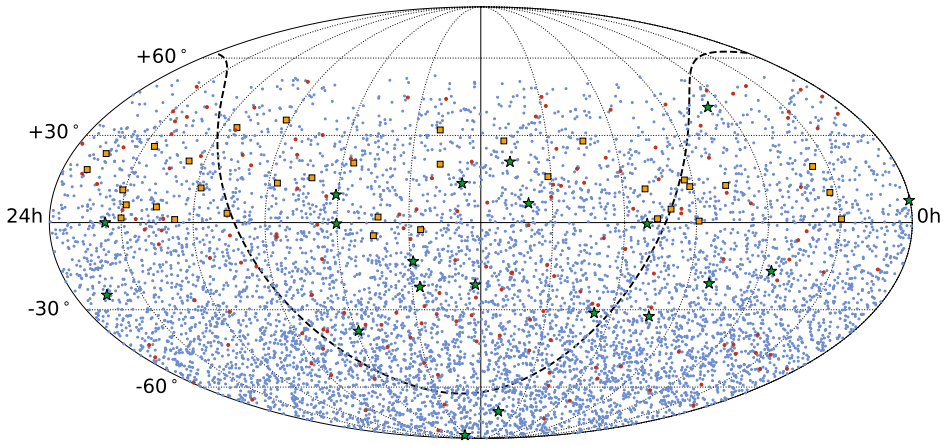

Figure 7.14: Sky map in equatorial coordinates of the 6894 track-like (blue circles) and the 160 shower-like (magenta circles) ANTARES events passing the selection cuts. Green stars and orange squares show the location of the 20 and 34 neutrino candidates from the HESE and Muon IceCube samples, respectively. The black, dashed line indicates the Galactic equator.

The most significant cluster, i.e. the cluster with the lowest pre-trial p-value, is found at the location of the IceCube track with ID 15 from the Muon sample, with a number of fitted signal events $\hat{n}_s = 1.6$, a best-fit flare duration $\hat{\sigma}_t = 120$ days and a best-fit spectral index $\hat{\gamma} = 3.5$. The pre-trial p-value of the cluster is 3.7%, corresponding to a significance of 2.1 σ. The second and third most significant sources correspond to HESE ID 71 and Muon ID 26, with pre-trial p-values of 3.8% and 4.6%, respectively. Since multiple candidates are analysed, trial factors must be taken into account, yielding a post-trial p-value of 90% for the most significant cluster. As no significant excess is observed, upper limits on the one-flavour neutrino fluence at 90% CL are derived. The limits are calculated using Equation 6.29 in which the best-fit flare duration $\hat{\sigma}_t$ is taken as ΔT.

The results, in terms of best-fit number of signal events $\hat{n}_s$, spectral index $\hat{\gamma}$, flare duration $\hat{\sigma}_t$ and upper limits on the one-flavour neutrino fluence, are reported in Tables 7.9 and 7.10. For those sources for which a null number of signal events is obtained as best fit, limits are calculated assuming $\Delta T = 120$ days, chosen arbitrarily, as the value of the fitted flare duration is meaningless for clusters fully compatible with being background-like. The one-flavour neutrino fluence upper limits and sensitivities calculated for the same flares are shown as a function of the source declination for the two spectral assumptions in Figure 7.15.

A discussion on the implications of the null observation in a time window of 0.1 day follows. The search does not reveal any ANTARES track-like (shower-like) event in correlation with any IceCube candidate within a time window of 0.1 day and a maximal angular distance of 10° (30°). Under the hypothesis that each IceCube candidate is produced by a different point-like transient source with a flare duration ≤ 0.1 day, this non-detection is used to derive a constraint on the spectral index of such a source. Assuming that no neutrino candidate is observed, the 90% CL upper limit on the mean number of ANTARES events in time correlation with an IceCube HESE/Muon candidate is $\hat{\mu}_s^{90\%\mathrm{CL}} = 2.3$, using a counting method and assuming Poisson statistics. The corresponding upper limit on the neutrino fluence normalisation for different spectral indices γ can be obtained as

$$\mathcal{F}_\gamma^{90\%\mathrm{CL}} = \frac{\hat{\mu}_s^{90\%\mathrm{CL}}}{\int A_{\mathrm{eff}}^{\mathrm{ANT}}(E_\nu) \cdot E_\nu^{-\gamma} dE_\nu}\,, \tag{7.10}$$

where $A_{\mathrm{eff}}^{\mathrm{ANT}}$ is the ANTARES effective area. The 90% CL upper limit on the number of signal events expected to be observed by IceCube from a neutrino fluence $\mathcal{F}_\gamma^{90\%\mathrm{CL}} E_\nu^{-\gamma}$ is then calculated as

$$N_{\nu,\mathrm{IC}}^{90\%\mathrm{CL}} = \int \mathcal{F}_\gamma^{90\%\mathrm{CL}} \cdot A_{\mathrm{eff}}^{\mathrm{IC}}(E_\nu) \cdot E_\nu^{-\gamma} dE_\nu\,, \tag{7.11}$$

with $A_{\mathrm{eff}}^{\mathrm{IC}}$ being either the HESE or Muon IceCube effective area [151].

The 90% CL upper limits, $N_{\nu,\mathrm{IC}}^{90\%\mathrm{CL}}$, as a function of the spectral index γ are shown in Figure 7.16 for the most energetic IceCube event of each sample, Muon ID 27 and . A transient origin with flare duration ≤ 0.1 day can be excluded at 90% CL for those spectral indices for which $N_{\nu,\mathrm{IC}}^{90\%\mathrm{CL}}$ is smaller than 1, because IceCube *has seen* one event from these directions. The events Muon ID 27 and HESE ID 45 are therefore consistent with the mentioned transient origin only for neutrino spectra harder than $E_\nu^{-2.4}$ and $E_\nu^{-2.3}$, respectively. These limits are

Table 7.9: List of analysed IceCube neutrino events from the HESE sample [46, 47, 48]. For each candidate, the equatorial coordinates – declination (δ) and right ascension (α) – , date of observation, and angular error estimate (β_{IC}) are reported. The following four columns show the result of the search in terms of best-fit values for the likelihood function parameters (number of signal events $\hat{n}_s$, spectral index $\hat{\gamma}$, flare duration $\hat{\sigma}_t$) and 90 % CL upper limits on the one-flavour neutrino fluence for the two assumed energy spectral indices. Dashes (-) in the fitted likelihood parameters indicate sources with a null number of fitted signal events. The values of E_{min} and E_{max} used to calculate the fluence upper limits are listed in the last column.

HESE ID	δ[°]	α[°]	observation time [MJD]	β_{IC}[°]	$\hat{n}_s$	$\hat{\gamma}$	$\hat{\sigma}_t$[days]	fluence limit [GeV cm^{-2}] $\gamma = 2.5/2.0$	$\log(\frac{E_{\mathrm{min}}}{\mathrm{GeV}})$ - $\log(\frac{E_{\mathrm{max}}}{\mathrm{GeV}})$ $\gamma = 2.5/2.0$
3	-31.2	127.9	55451.1	1.4	1.0	2.7	2.9	26.94 / 12.69	2.5 - 5.3 / 3.4 - 6.5
5	-0.4	110.6	55512.6	1.2	1.0	2.5	120	46.75 / 18.86	2.6 - 5.5 / 3.5 - 6.5
8	-21.2	182.4	55608.8	1.3	1.3	2.4	120	55.84 / 20.68	2.5 - 5.3 / 3.5 - 6.5
13	40.3	67.9	55756.1	1.2	0.9	2.9	120	41.94 / 20.75	3.1 - 5.8 / 3.9 - 7.0
18	-24.8	345.6	55923.5	1.3	-	-	-	28.04 / 12.10	2.5 - 5.3 / 3.4 - 6.5
23	-13.2	208.7	55949.6	1.9	0.8	2.2	120	33.07 / 13.91	2.6 - 5.3 / 3.5 - 6.5
28	-71.5	164.8	56048.6	1.3	2.3	3.4	120	20.37 / 7.87	2.5 - 5.2 / 3.4 - 6.0
37	20.7	167.3	56390.2	1.2	-	-	-	30.33 / 14.27	2.9 - 5.7 / 3.6 - 6.7
43	-22.0	206.6	56628.6	1.3	0.8	2.4	26.0	24.24 / 10.50	2.5 - 5.3 / 3.5 - 6.5
44	0.0	336.7	56671.9	1.2	0.9	1.9	120	47.36 / 18.99	2.6 - 5.5 / 3.5 - 6.5
45	-86.2	219.0	56679.2	1.2	1.4	3.3	64.3	20.98 / 8.46	2.5 - 5.2 / 3.4 - 5.8
53	-37.7	239.0	56767.1	1.2	1.3	2.5	120	27.56 / 11.61	2.5 - 5.3 / 3.5 - 6.5
58	-32.4	102.1	56859.8	1.3	1.0	3.1	18.4	30.78 / 14.29	2.5 - 5.3 / 3.4 - 6.5
61	-16.5	55.6	56970.2	1.2	-	-	-	24.00 / 11.50	2.6 - 5.3 / 3.5 - 6.5
62	13.3	187.9	56987.8	1.3	-	-	-	28.67 / 13.14	2.8 - 5.5 / 3.6 - 6.5
63	6.5	160.0	57000.1	1.2	0.8	3.4	120	27.69 / 13.02	2.8 - 5.5 / 3.5 - 6.5
71	-20.8	80.7	57140.5	1.2	0.9	1.8	120	61.21 / 23.95	2.5 - 5.3 / 3.5 - 6.5
76	-0.4	240.2	57276.6	1.2	-	-	-	27.80 / 11.76	2.6 - 5.5 / 3.5 - 6.5
78	7.5	0.4	57363.4	1.2	-	-	-	27.07 / 12.42	2.8 - 5.5 / 3.5 - 6.5
82	9.4	240.9	57505.2	1.2	-	-	-	27.52 / 12.73	2.8 - 5.5 / 3.5 - 6.5

Table 7.10: List of analysed IceCube neutrino events from the Muon sample [50, 51]. See caption of Table 7.9 for the meaning of the columns.

Muon ID	δ[°]	α[°]	observation time [MJD]	β_{IC}[°]	$\hat{n}_s$	$\hat{\gamma}$	$\hat{\sigma}_t$[days]	fluence limit [GeV cm^{-2}] $\gamma = 2.5/2.0$	$\log(\frac{E_{\mathrm{min}}}{\mathrm{GeV}})$ - $\log(\frac{E_{\mathrm{max}}}{\mathrm{GeV}})$ $\gamma = 2.5/2.0$
1	1.2	29.5	55056.7	1.0	-	-	-	27.57 / 12.20	2.6 - 5.5 / 3.5 - 6.5
2	11.7	298.2	55141.1	1.0	1.0	2.2	120	64.99 / 25.88	2.8 - 5.5 / 3.6 - 6.5
3	23.6	344.9	55355.5	1.1	2.2	3.0	120	61.56 / 27.35	3.0 - 5.7 / 3.8 - 6.8
5	21.0	307.0	55387.5	1.0	-	-	-	30.60 / 14.86	2.9 - 5.7 / 3.6 - 6.7
6	15.2	252.0	55421.5	4.4	1.1	1.9	120	50.08 / 19.88	2.9 - 5.5 / 3.6 - 6.5
7	13.4	266.3	55464.9	1.0	0.9	2.9	120	33.56 / 15.29	2.8 - 5.5 / 3.6 - 6.5
8	11.1	331.1	55478.4	1.0	1.0	2.2	120	43.31 / 18.59	2.8 - 5.5 / 3.5 - 6.5
9	0.5	89.0	55497.3	1.0	0.2	3.4	120	29.00 / 12.65	2.6 - 5.5 / 3.5 - 6.5
10	3.1	285.9	55513.6	1.0	1.2	3.5	26.0	43.95 / 18.77	2.8 - 5.5 / 3.5 - 6.5
11	1.0	307.7	55589.6	1.0	-	-	-	27.68 / 12.32	2.6 - 5.5 / 3.5 - 6.5
12	20.3	235.1	55702.8	1.0	-	-	-	32.08 / 14.76	2.9 - 5.5 / 3.6 - 6.7
13	35.5	272.2	55722.4	1.0	-	-	-	34.86 / 18.34	3.0 - 5.8 / 3.9 - 6.8
14	5.3	315.7	55764.2	2.1	1.0	2.5	6.8	35.20 / 15.21	2.8 - 5.5 / 3.5 - 6.5
15	1.9	222.9	55896.9	1.0	1.6	3.5	120	75.21 / 28.65	2.6 - 5.5 / 3.5 - 6.5
16	19.1	36.6	55911.3	1.0	-	-	-	31.22 / 13.91	2.9 - 5.5 / 3.6 - 6.7
17	32.0	198.7	56063.0	1.0	1.1	3.5	120	45.07 / 22.82	3.0 - 5.8 / 3.8 - 6.8
18	1.6	330.1	56146.2	1.0	0.3	1.6	120	27.70 / 12.07	2.6 - 5.5 / 3.5 - 6.5
19	-2.4	205.1	56211.8	1.0	1.2	3.4	98.8	48.10 / 18.82	2.6 - 5.5 / 3.5 - 6.5
20	28.0	169.6	56226.6	1.0	-	-	-	29.79 / 15.61	3.0 - 5.7 / 3.8 - 6.8
21	14.5	93.4	56470.1	1.0	-	-	-	30.02 / 13.42	2.8 - 5.5 / 3.6 - 6.5
22	-4.4	224.9	56521.8	1.0	1.1	3.5	120	47.21 / 20.02	2.6 - 5.5 / 3.5 - 6.5
23	10.2	32.9	56579.9	1.0	1.3	3.4	120	53.95 / 22.93	2.8 - 5.5 / 3.5 - 6.5
24	32.8	293.3	56666.5	1.0	1.8	3.3	19.6	41.02 / 20.85	3.0 - 5.8 / 3.8 - 6.8
25	18.1	349.4	56800.0	1.1	-	-	-	29.30 / 13.62	2.9 - 5.5 / 3.6 - 6.7
26	1.3	106.3	56817.6	1.0	1.0	1.6	120	62.82 / 24.26	2.6 - 5.5 / 3.5 - 6.5
27	11.4	110.6	56819.2	1.0	-	-	-	28.96 / 12.90	2.8 - 5.5 / 3.5 - 6.5
28	4.6	100.5	57049.5	1.0	-	-	-	27.09 / 12.46	2.8 - 5.5 / 3.5 - 6.5
29	12.2	91.6	57157.9	1.0	-	-	-	28.39 / 12.89	2.8 - 5.5 / 3.6 - 6.5
30	26.1	325.5	57217.9	1.0	1.3	3.2	114.2	53.40 / 24.14	3.0 - 5.7 / 3.8 - 6.8
31	6.0	328.4	57246.8	1.0	-	-	-	25.83 / 12.40	2.8 - 5.5 / 3.5 - 6.5
32	28.0	134.0	57269.8	1.0	0.6	3.4	118.9	36.77 / 18.97	3.0 - 5.7 / 3.8 - 6.8
33	19.9	197.6	57312.7	1.5	-	-	-	30.75 / 13.80	2.9 - 5.5 / 3.6 - 6.7
34	12.6	76.3	57340.9	1.0	-	-	-	28.93 / 13.29	2.8 - 5.5 / 3.6 - 6.5
35	15.6	151.3	57478.6	1.0	2.5	3.5	120	60.38 / 24.58	2.9 - 5.5 / 3.6 - 6.5

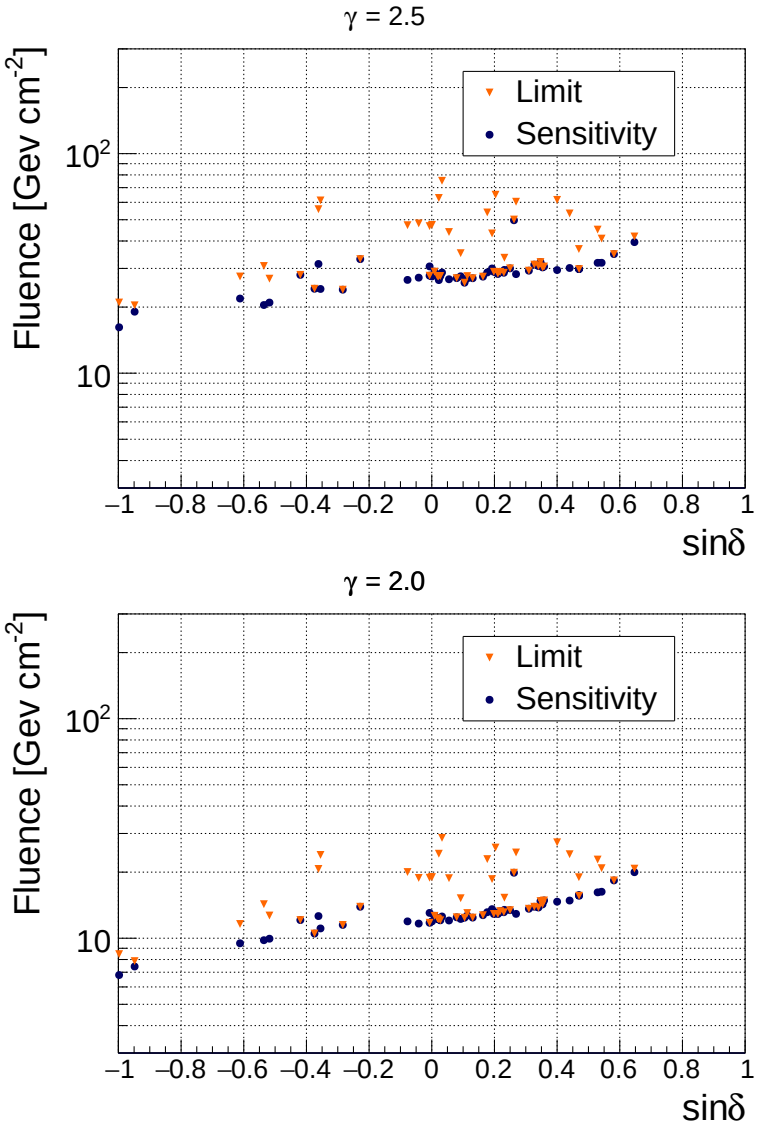

Figure 7.15: Upper limits at $90\,\%$ CL on the one-flavour neutrino fluence (orange triangles) and sensitivities (blue dots) as a function of the investigated candidate declination for two tested signal energy spectra: $E_\nu^{-2.5}$ (top) and $E_\nu^{-2.0}$ (bottom). Upper limits and sensitivities are calculated for the time windows reported in Tables 7.9 and 7.10. A time window of $120\,\mathrm{days}$ is used for those sources with a null number of fitted signal events.

compatible with the IceCube best-fit spectral indices 2.1 ± 0.2 and 2.2 ± 0.2 [44] for the 2014-15 neutrino flare from the direction of TXS 0506+056 fitted with the Gaussian-shaped and with the box-shaped time profiles introduced in Section 1.4, respectively. However, the limits set by this analysis are valid only for a flare duration ≤ 0.1 day while the 2014-15 neutrino is much longer.

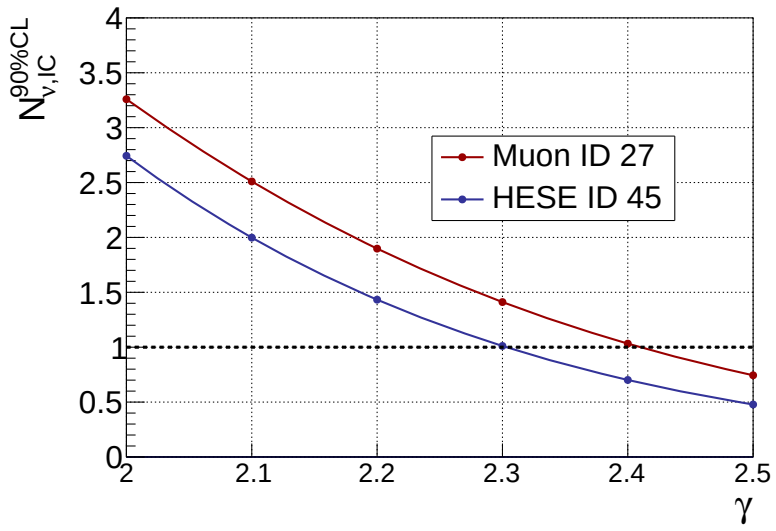

Figure 7.16: 90% CL upper limits on the expected number of IceCube events originated from a transient $E_\nu^{-\gamma}$ point-like source emitting in a time window ≤ 0.1 days as a function of the spectral index γ for the most energetic IceCube event of the Muon sample, Muon ID 27 [50], and of the HESE sample, HESE ID 45 [47]. The dotted line indicates the number of events detected by IceCube. Cases under this dotted line are therefore excluded as a result of this analysis.

7.4 Estimation of the future sensitivity of KM3NeT/ARCA Phase 1 to point-like sources

This Section presents the expected performances of KM3NeT/ARCA Phase 1 for point-like sources. The employed Monte Carlo sample is described in Section 7.4.1, while the analysis method and the results are reported in Section 7.4.2.

7.4.1 Monte Carlo sample

The estimation of the future performance of KM3NeT/ARCA Phase 1 is obtained by means of PEs. In these, Monte Carlo simulations of cosmic neutrinos and of atmospheric neutrinos and muons are used to simulate the signal and the background events, respectively. All the events are tracks reconstructed with the JGandalf algorithm (see Section 4.2.3). In each PE, the number of simulated background events is given by the number of background events expected to be detected in the chosen livetime. Only upgoing events ($\cos\theta > -0.1$) are employed in the analysis. Additional cuts are applied on two quality parameters provided by the reconstruction algorithm: $\Lambda_{\text{red}} < -0.9$ and $\log_{10}(\beta_0) < -0.6$.

Λ_{red} is the reduced likelihood, defined as $\Lambda_{\text{red}} = \frac{\Lambda}{N_{\text{hits}}}$, i.e. as the value of the likelihood provided by the reconstruction algorithm divided by the number of hits used in the reconstruction, while β_0 is defined as $\beta_0 = \sqrt{T_x^2 + T_y^2}$, with T_x and T_y being the estimated uncertainties on the x and y direction cosines, respectively. The distributions of the quality parameters Λ_{red} and β_0 for simulated atmospheric muons, atmospheric neutrinos and cosmic neutrinos are shown in Figure 7.17. The selection criteria are optimised to minimise the 5σ discovery potential for an $E_\nu^{-2.0}$ spectrum.

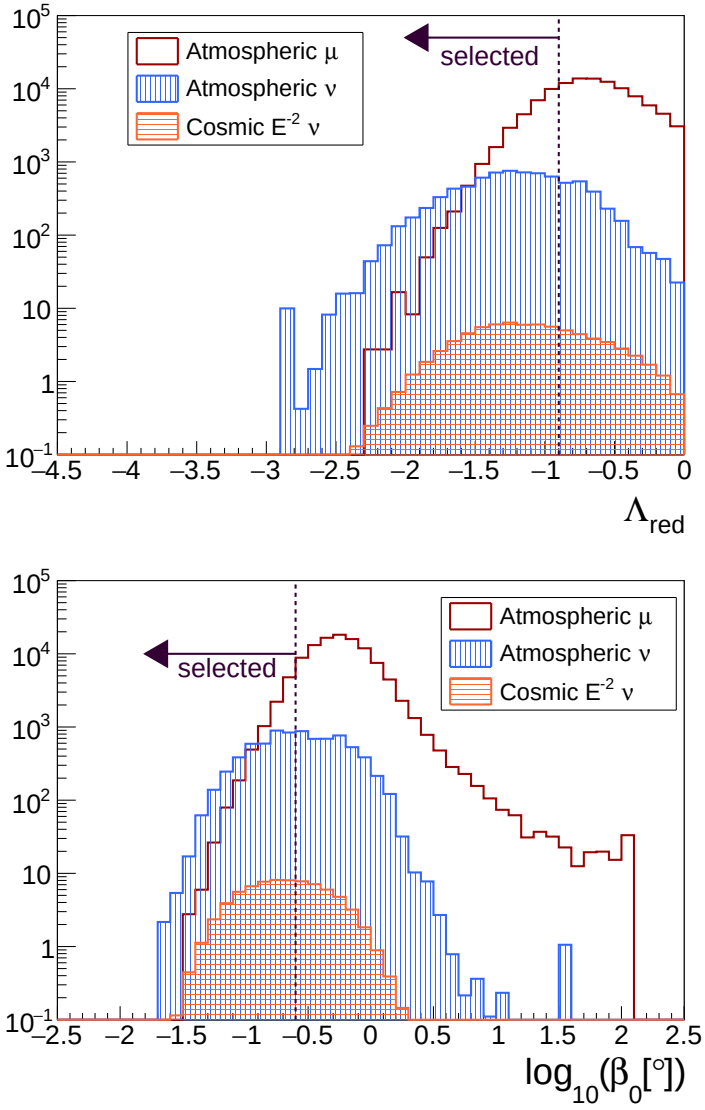

Figure 7.17: Distribution of the quality parameters Λ_{red} (top) and β_0 (bottom) for simulated up-going ($cos\theta > -0.1$) atmospheric muons, atmospheric neutrinos and cosmic neutrinos following an E_ν^{-2} spectrum. In both figures, the dashed vertical line indicates the cut value.

The one-year acceptance of KM3NeT/ARCA Phase 1 for an $E_\nu^{-2.0}$ spectrum is presented in Figure 7.18-top, while Figure 7.18-bottom shows the cumulative distribution of the angular resolution of KM3NeT/ARCA Phase 1 tracks for an $E_\nu^{-2.0}$ spectrum.

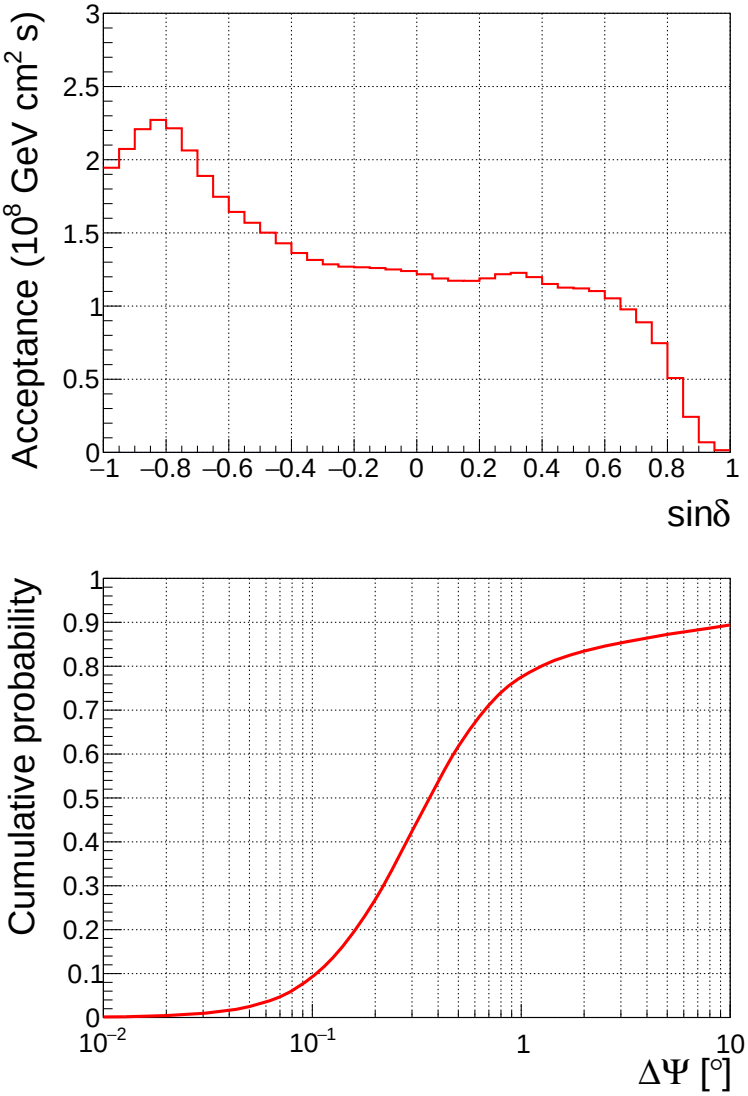

Figure 7.18: Top: Acceptance as a function of the source declination for an $E_\nu^{-2.0}$ spectrum with a flux normalisation $\Phi_0 = 10^{-8}\mathrm{GeV}^{-1}\ \mathrm{cm}^{-2}\ \mathrm{s}^{-1}$ for the selected track-like events detected by KM3NeT/ARCA Phase 1 after one year of operation. Bottom: Cumulative angular resolution distribution for an $E_\nu^{-2.0}$ spectrum for the KM3NeT/ARCA Phase 1 track sample.

7.4.2 Search method and expected performances

The analysis method relies on an unbinned likelihood defined as

$$\mathcal{L}(n_s) = \prod_{i=1}^{\mathcal{N}} \left[\frac{n_s}{\mathcal{N}} \mathcal{S}_i + \left(1 - \frac{n_s}{\mathcal{N}}\right) \mathcal{B}_i \right], \tag{7.12}$$

where n_s, the only free parameter in the likelihood maximisation, is the unknown number of signal events, $\mathcal{S}_i$ and $\mathcal{B}_i$ are the values of the signal and background PDFs for the event i, and $\mathcal{N}$ is the total number of signal and background events in the simulated sample. The combined information of the direction and the energy of the events is included in the definition of the PDFs. For each simulated event i, the probability of being reconstructed as signal or background is given by:

$$\mathcal{S}_i = \mathcal{S}^{\text{space}}(\Delta\Psi_i)\mathcal{S}^{\text{energy}}(N_i^{\text{hits}}), \tag{7.13}$$

$$\mathcal{B}_i = \mathcal{B}^{\text{space}}(\delta_i)\mathcal{B}^{\text{energy}}(N_i^{\text{hits}}), \tag{7.14}$$

where:

- $\mathcal{S}^{\text{space}}$, the probability density function of reconstructing a simulated event i at a given angular distance $\Delta\Psi_i$ from the source location, is given by the Point Spread Function.
- $\mathcal{B}^{\text{space}}$ yields the probability density of reconstructing a background event at a certain declination δ_i. The distribution of the declination of the background events is shown in Figure 7.19.
- $\mathcal{S}^{\text{energy}}$ and $\mathcal{B}^{\text{energy}}$ give the probability density for a signal or background event to be reconstructed with a certain value of N^{hits}, the number of hits used by the reconstruction algorithm.

The expected performance of KM3NeT/ARCA Phase 1 in terms of 5σ discovery flux and sensitivity after one year and two years of operation is presented in Figure 7.20. For comparison, the 11-year ANTARES curves are also shown. KM3N3T/ARCA Phase 1 will surpass ANTARES present limits in only two years of operation.

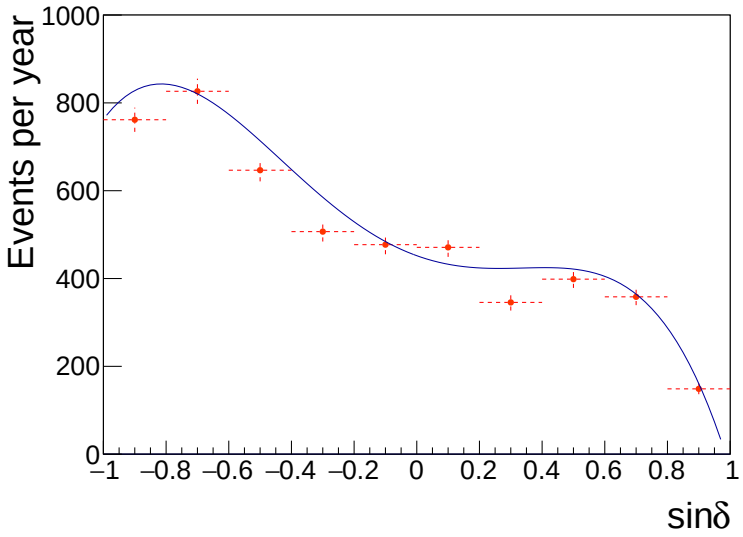

Figure 7.19: Number of selected track-like events per year as a function of the declination in KM3NeT/ARCA Phase 1. The solid line represents a parameterisation used in the simulation.

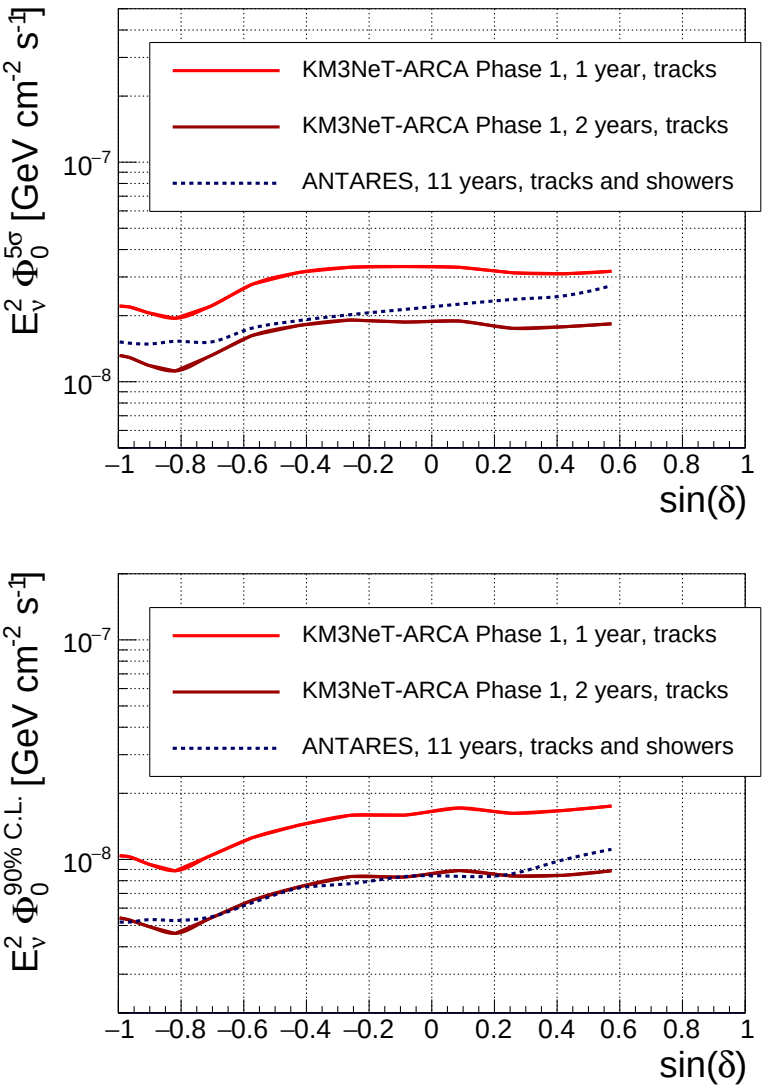

Figure 7.20: Estimation of the 5σ dicovery flux (top) and sensitivity (bottom) of KM3NeT/ARCA Phase 1 after one and after two years of operation (red and dark red solid lines respectively). The curves from the 11-year ANTARES point-like source analysis (dotted lines) are also shown.

Conclusions

High-energy neutrino astronomy is a relatively young discipline. It derived from the opportunity of extending conventional astronomy beyond the usual electromagnetic messengers in order to attempt to answer the outstanding question in astroparticle physics about the origin of high-energy cosmic rays.

The only currently operating kilometer-sized neutrino telescope, IceCube, has recently reported the first significant observations of a high-energy astrophysical neutrino flux and the first evidence for neutrino emission from an individual cosmic source, opening a new era for high-energy neutrino astronomy.

ANTARES, being the current largest underwater neutrino telescope, located in the Northern Hemisphere, provided with an excellent visibility of the Galactic Plane, and with a very good angular resolution both in the track channel and in the shower channel, is a well suited tool for the study of point-like signals of cosmic neutrinos. Thanks to these features, ANTARES has been able to place relevant constraints on the origin of the astrophysical neutrino flux reported by IceCube, in particular on any possible Galactic contribution.

The high quality of the ANTARES data and the competitiveness of the results obtained have been possible thanks to considerable efforts in the development and maintenance of the telescope, including the time calibration of the detector, which is a crucial factor for the angular resolution of the instrument.

The experience acquired with ANTARES will play an important role in the developement of the future, much larger array, KM3NeT. Deployed in two sites in the Mediterranean sea, it will explore the Southern Sky with unprecedented sensitivity and angular resolution. It is expected to detect the neutrino flux reported by IceCube within a few months of operation and it will be able to make definite statements about a neutrino flux from several Galactic candidates.

The time calibration of the ANTARES detector and the search for cosmic neutrino sources using the ANTARES, KM3NeT, and IceCube detectors have been the two main topics addressed in this Thesis. The main conclusions obtained from

both works are summarized below.

Time calibration

In order to achieve an angular resolution better than 0.3° in ANTARES for track-like events with energies above 10 TeV, an accuracy of $\sim$1 ns in the relative time calibration among PMTs is needed. The time calibration of the ANTARES detector has been performed for two years (2017 and 2018) of the data taking period using a recently developed method. The novel procedure allows to obtain an increase in the number of well-reconstructed events with respect to the previously employed calibration method and consists of three steps. First, the time offsets among lines (inter-line calibration) are calculated using the atmospheric-muon calibration method. Second, the time offsets among ARSs in the same storey (intra-storey calibration) are derived using the ^{40}K calibration method. Third, the atmospheric-muon calibration method is employed to obtain the time offsets among storeys (inter-storey calibration), using as input the output of the previous two steps.

Searches for cosmic neutrino sources

The results of three different analyses of the data recorded by high-energy neutrino telescopes have been presented: an update of the ANTARES standard point-like source search using 11 years of ANTARES data, a combined search for point-like and extended sources of astrophysical neutrinos in the Southern Sky using the joined data of ANTARES and IceCube, and a search for time and space correlations between ANTARES data and IceCube high-energy astrophysical neutrino candidates. Moreover, the first estimation of the sensitivity to point-like sources of the first construction phase of the future detector dedicated to high-energy astronomy, KM3NeT/ARCA, has been presented. All the analyses rely on a maximum likelihood approach, employed to identify clusters of cosmic neutrinos from individual sources over the background of randomly distributed atmospheric neutrinos. The results of these analyses are summarised here.

Searches for point-like sources of cosmic neutrinos with 11 years of ANTARES data

Various searches for steady point-like sources using both track-like and shower-like events detected by the ANTARES telescope during 11 years of data taking

were performed. The searches include a scan over the whole ANTARES visible sky (full-sky search), an investigation of 111 astrophysical source candidates and 75 IceCube tracks, and a dedicated analysis of the direction of the TXS 0506+056 blazar. No significant evidence of cosmic neutrino sources was found and 90% CL upper limits on the one-flavour flux normalisation were set.

The most significant cluster of the full-sky search was found at equatorial coordinates $(\alpha, \delta) = (343.7°, 23.6°)$, with a pre-trial p-value of 1.5×10^{-6}, corresponding to a post-trial significance of $23\,\%$ (1.2σ).

Out of the 111 investigated directions of known astrophysical objects, the most signal-like cluster was found at the location of HESSJ0632+057, at equatorial coordinates $(\alpha, \delta) = (98.24°, 5.81°)$, with a pre-trial p-value of 0.15% (1.4σ post-trial significance).

A total of 75 IceCube neutrino candidates classified as tracks selected from the HESE and the Muon samples and from the IceCube HESE and EHE alerts were analysed in a separate candidate list search in order to account for their non-negligible angular uncertainty. In this case, the position in the sky of the fitted source was left as an additional free parameter in the likelihood maximization. The Muon event with ID 3 is the IceCube track candidate with the largest excess. The fitted cluster is located at $(\hat{\alpha}, \hat{\delta}) = (343.7°, 23.6°)$, which is at a distance of 0.2° from the original Muon track at $(\alpha, \delta) = (343.55°, 23.78°)$, and coincident with the most significant cluster found in the full-sky search. The trial-corrected significance of the source is 1.5% (2.4σ).

A dedicated search for steady emission of neutrinos from the direction of the first plausible cosmic source of high-energy neutrinos, the blazar TXS 0506+056, was performed. A value of $\hat{n}_s = 1.03$ signal events was obtained from the maximisation at the position of the cluster, with a p-value of 3.4% (2.1σ).

ANTARES and IceCube Combined Search for Neutrino Point-like and Extended Sources in the Southern Sky

In this analysis, the complementarity of the ANTARES and the IceCube telescopes was exploited by combining the data of both detectors to search for cosmic neutrino sources in the Southern Sky, improving the sensitivity compared to the individual analyses.

Five different searches for point-like and extended sources of neutrinos were performed using ANTARES track-like and shower-like events from the Southern Sky recorded in nine years, combined with seven years of IceCube through-going

track-like events. Neither significant point-like nor extended neutrino emission over the background expectation was found and 90% CL upper limits on the one-flavour flux normalisation were set.

The first two analyses consisted of a scan of the full Southern Sky and of a restricted region around the Galactic Centre. Both the inspected regions were scanned for point-like sources and extended source assuming a Gaussian emission profile of various widths ($\sigma_s = 0.5°$, $1.0°$, $2.0°$). The largest excess over the whole Southern Sky was found at equatorial coordinates $(\hat{\alpha}, \hat{\delta}) = (213.2°, -40.8°)$, for a point-like source hypothesis, with a post-trial significance of 18% (1.3σ). When limiting the search to the Galactic Centre region, the most significant cluster was found for a source extension of $2.0°$, at equatorial coordinates $(\hat{\alpha}, \hat{\delta}) = (274.1°, -40.1°)$, with a post-trial significance of 3% (2.2σ).

In the third approach, the directions of a pre-defined list of 57 known sources were investigated. The most significant source candidate is HESS J1023-575 with a post-trial significance of 42% (0.8σ). Upper limits on the neutrino flux from 57 astrophysical candidate sources were derived.

Finally, dedicated searches at the location of two promising neutrino source candidates, the super-massive black hole Sagittarius A*, and the shell-type supernova remnant RX J1713.7-3946 were carried out. Sagittarius A* was tested as a point-like source and as an extended source. The largest excess over the background was observed at an angular extension of $0.0°$ with a significance of 6% (1.9σ). Finally, the location of the SNR RX J1713.7-3946 was investigated assuming two proposed neutrino emission models and a source extension of $0.6°$. As no significant evidence of cosmic neutrinos was observed, upper limits were derived.

The results of this combined analysis proved the strong potential of the ANTARES and IceCube joint search for neutrino sources in the Southern Sky. The combination of the two detectors, which differ in size and location, allows for an improvement of up to a factor $\sim$2 in the sensitivity in different regions of the Southern Sky, depending on the energy spectrum of the source. While for a soft spectral index, the contribution of high-energy neutrinos is suppressed and ANTARES dominates in most of the Southern Sky, for a harder spectral index all the samples provide a significant contribution and the complementarity of the two detectors is more effective. For an $E_\nu^{-2.0}$ spectrum a considerable gain in the sensitivity to point-like sources is achieved in all the Southern Sky and, in a larger scale, in the region close to the Galactic Centre.

ANTARES neutrino search for time and space correlations with IceCube high-energy neutrino events

In this analysis, the data recorded by the ANTARES telescope were scanned to search for time and space correlations with 54 IceCube HESE and Muon astrophysical neutrino candidates, in order to test for a possible transient origin of the IceCube events. In contrast to time-integrated searches, the information of the neutrino arrival times was exploited to enhance the discovery potential. A Gaussian profile was assumed for the time emission with the standard deviation being a free likelihood parameter allowed to vary between 0.1 and 120 days. No significant excess over the expected background was observed for any of the investigated IceCube candidate location and upper limits on the one-flavour neutrino fluence were derived.

The most significant cluster was found at the location of the IceCube track with ID 15 from the Muon sample, with a best-fit flare duration of 120 days and a pre-trial p-value of 3.7% (2.1 σ significance), corresponding to a post-trial p-value of 90%. The non-detection of any ANTARES event within 0.1 day from the IceCube neutrino observation times was used to constrain the spectral index of a possible flaring source responsible for the most energetic IceCube event of both the HESE and the Muon samples to be harder than -2.3 and -2.4, respectively.

Estimation of the future sensitivity of KM3NeT/ARCA Phase 1 to point-like sources

The estimation of the future performance of KM3NeT/ARCA Phase 1 was obtained using Monte Carlo simulations of cosmic neutrinos and of atmospheric neutrinos and muons reconstructed as track-like events. The results showed that the 24 lines of KM3NeT/ARCA Phase 1 will surpass the current performance of ANTARES, corresponding to 11 years of data taking, after only two years of operation, opening new exciting perspectives in neutrino astronomy.

Resumen

En el presente manuscrito se expone el trabajo realizado para la búsqueda de fuentes de neutrinos de alta energía con los telescopios ANTARES, KM3NeT y IceCube y para la calibración temporal de ANTARES.

Astronomía con neutrinos

La astronomía con neutrinos de alta energía es una disciplina relativamente joven. Nació de la necesidad de extender la astronomía convencional más allá de los mensajeros electromagnéticos habituales para intentar responder la cuestión pendiente del origen de los rayos cósmicos de alta energía. Los neutrinos, al ser partículas neutras y que interactúan solo débilmente, son mensajeros cósmicos muy útiles: pueden escapar de entornos densos y pueden viajar largas distancias sin ser desviados por los campos magnéticos cósmicos, lo que permite apuntar con precisión a sus sitios de producción. Debido a estas características únicas, los neutrinos con energías del GeV-PeV pueden proporcionar las pistas que faltan para revelar el origen de los rayos cósmicos, que permanece en gran parte sin resolver más de un siglo después de su descubrimiento.

Se espera que los neutrinos astrofísicos se produzcan junto con los rayos γ en la interacción de los rayos cósmicos acelerados de alta energía con la materia ambiental o los campos de fotones en las proximidades de sus sitios de aceleración. Sin embargo, aunque también mecanismos leptónicos pueden producir los rayos γ, los neutrinos son la prueba irrefutable de procesos hadrónicos y, por lo tanto, constituyen una evidencia única de la aceleración de los rayos cósmicos.

Si bien la muy pequeña probabilidad de interacción de los neutrinos los convierte en mensajeros astronómicos de valor único, también hace que su detección sea extremadamente difícil. Dado que los neutrinos solo se ven afectados por la interacción débil, la detección debe basarse en partículas secundarias producidas en las interacciones de los neutrinos. Los telescopios de neutrinos de alta energía,

cuyo principio de detección fue sugerido por primera vez por M. A. Markov en 1960, están diseñados para detectar los leptones cargados producidos cuando un neutrino interactúa con el material alrededor o dentro del detector. El detector, un conjunto tridimensional de tubos fotomultiplicadores dentro de un medio transparente como el agua o el hielo, recoge la radiación Cherenkov inducida por el pasaje de las partículas cargadas relativistas dentro o cerca del volumen instrumentado. La información grabada por los fotomultiplicadores, llamada *hit*, consiste en el tiempo y la carga integrada de la señal registrada. La información proporcionada por el número de fotones Cherenkov detectados, su ubicación y sus tiempos de llegada se utiliza para inferir la dirección de llegada del neutrino original y una estimación de su energía. Dichos detectores se instalan a grandes profundidades y se optimizan para detectar la luz de las partículas que vienen de abajo producidas por los neutrinos que han atravesado la Tierra para limitar el fondo de los muones atmosféricos.

En los telescopios de neutrinos se pueden identificar dos topologías de eventos principales: trazas y cascadas. Las interacciones de corriente cargada de neutrinos y antineutrinos muónicos producen un muon relativista que puede viajar grandes distancias a través del medio. La luz Cherenkov se emite a lo largo del camino del muon dejando una marca similar a una traza en el detector. Los eventos de tipo cascada son inducidos por interacciones de corriente neutra y por interacciones de corriente cargada de neutrinos y antineutrinos electrónicos y tau. Se caracterizan por una emisión de luz casi esféricamente simétrica. La longitud mayor de las trazas permite una mejor reconstrucción de la dirección de la partícula y, por lo tanto, una mejor resolución angular media, haciendo que las trazas sean más adecuadas que las cascadas para buscar fuentes puntuales. Por otro lado, se logra una mejor reconstrucción de la energía de las partículas con las cascadas, ya que la topología permite una medición calorimétrica.

Telescopios de neutrinos de alta energía actualmente en funcionamiento, como ANTARES y IceCube, y la futura red de telescopios de neutrinos ahora en construcción, KM3NeT, se basan en el principio de detección que se acaba de describir.

ANTARES es un telescopio de neutrinos ubicado en 40 km de Toulon, Francia, a $42°48'$ N, $6°10'$ E, anclado a unos 2500 m debajo de la superficie del mar Mediterráneo. La construcción del detector se completó a mediados de 2008, dos años después del despliegue de la primera línea, lo que lo convierte en el primer telescopio de neutrinos submarino en funcionamiento. La luz Cherenkov

es detectada por un conjunto de 885 fotomultiplicadores que miran 45° hacia abajo para optimizar la detección de luz inducida por partículas que viajan hacia arriba. Los fotomultiplicadores están distribuidos a lo largo de 12 líneas flexibles, de una longitud de 450 m y a una distancia entre ellas de 60-70 m, ancladas al fondo del mar por medio de un peso muerto y mantenidas verticales con una boya en su parte superior. Cada línea incluye 25 pisos (*storeys*) separados por una distancia de 14.5 m y conectados por cables mecánicos electro-ópticos. Un piso es una estructura de titanio que aloja tres módulos ópticos (OMs), que son esferas de vidrio resistentes a la presión que albergan el fotomultiplicador. Al estar en el hemisferio norte y a latitudes intermedias, el telescopio ANTARES cuenta con una vista privilegiada del Centro Galáctico y el Plano Galáctico, donde se esperan muchos candidatos de fuentes de neutrinos.

KM3NeT es la futura red de telescopios de neutrinos bajo el agua que se está actualmente desplegando en el mar Mediterráneo. Comprenderá dos detectores de neutrinos con granularidad diferente de módulos ópticos para apuntar a diferentes energías de neutrinos: KM3NeT/ARCA, un detector más grande con una configuración más dispersa con el objetivo de detectar fuentes de neutrinos cósmicos de alta energía, y KM3NeT/ORCA, un detector más pequeño y más denso dedicado al estudio de la jerarquía de masas de neutrinos. El proceso de construcción consistirá en una implementación de múltiples etapas con un volumen creciente de aproximadamente 0.1 km^3 en la primera fase de construcción a un volumen de varios km^3 en la fase final. ARCA se está desplegando a 100 km de Porto Palo di Capo Passero, Sicilia, Italia, mientras ORCA se ubicará a 10 km al oeste de la posición de ANTARES. Cada detector se basa en un diseño modular hecho de bloques de 115 líneas de 18 módulos ópticos digitales (DOMs), cada uno con 31 fotomultiplicadores. La primera etapa de construcción, la Fase 1, comprende 24 líneas de ARCA y 6 de ORCA, que corresponden en total a aproximadamente 0.2 bloques, mientras la segunda etapa de construcción comprenderá un total de tres bloques: dos de ARCA y uno de ORCA. Hasta la fecha, una línea de ARCA y cuatro de ORCA se han desplegando y están tomando datos con éxito. Como ARCA y ORCA apuntan a diferentes energías de neutrinos, la distancia entre líneas y entre DOMs se ha optimizado en consecuencia. En ARCA, las líneas tienen una longitud de unos 700 m y están separadas 95 m en promedio, con DOMs separados por 36 m en dirección vertical, comenzando a unos 80 m del fondo del mar. El volumen instrumentado total es de aproximadamente 1 km^3. En ORCA, las líneas tienen una altura de 200 m,

están separadas horizontalmente por unos 20 m, con DOMs separados 9 m en dirección vertical, comenzando a unos 40 m del fondo del mar. Esto representa un volumen total aproximadamente 125 veces menor que el de ARCA.

IceCube es un detector de neutrinos ubicado en el Polo Sur geográfico, en la estación permanente de Amudsen-Scott, entre 1450 y 2450 m debajo de la superficie del hielo antártico. Su construcción se completó en diciembre de 2010 después de seis años de despliegue durante el cual las configuraciones parciales del detector ya estaban tomando datos. Se compone de más de 5000 fotomultiplicadores repartidos entre 86 líneas verticales. Con un volumen instrumentado de un kilómetro cúbico, IceCube es actualmente el detector de neutrinos más grande del mundo.

Recientemente, IceCube comunicó la primera observación significativa de un flujo difuso de neutrinos de alta energía de origen extraterrestre junto con la primera asociación convincente de neutrinos astrofísicos con una fuente cósmica individual, el blazar TXS 0506+056. Estos descubrimientos recientes revelan el potencial de la astronomía de neutrinos para explorar el Universo de alta energía y refuerzan el interés de estudios adicionales.

La calibración de tiempo del detector ANTARES y la búsqueda de fuentes de neutrinos cósmicos utilizando los detectores ANTARES, KM3NeT y IceCube han sido los dos temas principales abordados en esta Tesis. Los métodos utilizados y las principales conclusiones obtenidas en ambos trabajos se resumen a continuación.

Calibración temporal

La reconstrucción de los eventos de ANTARES se basa en la medición de los tiempos de llegada de los fotones Cherenkov en los fotomultiplicadores. La precisión en la determinación de los tiempos de llegada está estrechamente relacionada con la mejor resolución angular alcanzable, que a su vez es el factor clave para la identificación de fuentes puntuales de neutrinos cósmicos.

En ANTARES, se emplean diversos procedimientos y sistemas para la calibración del tiempo relativo entre los elementos del detector (OM/piso/línea). La calibración relativa consiste en determinar el desplazamiento temporal (*time offset*) entre los tiempos registrados por los elementos. Antes del despliegue de las líneas, se realiza una calibración en tierra, con un procedimiento que consiste en iluminar simultáneamente grupos de OMs mediante un láser. Una vez en el mar, la

calibración se realiza utilizando un sistema basado en eco, en el que se miden los tiempos de retorno de las señales infrarrojas enviadas desde la costa, para sincronizar todas las tarjetas electrónicas. Otros métodos de calibración in situ, basados en LEDs, láseres, muones atmosféricos y desintegraciones de ^{40}K, se utilizan para sincronizar el tiempo de viaje de la señal entre la electrónica y el fotocátodo del fotomultiplicador.

Además de la calibración del tiempo relativo, es necesaria una calibración del tiempo absoluto, es decir, la sincronización entre el tiempo del detector y el Tiempo Universal Coordinado (UTC). El tiempo absoluto es relevante para determinar posibles correlaciones de los eventos de ANTARES con fuentes astrofísicas. La calibración del tiempo absoluto se realiza mediante un sistema de cronometraje GPS.

La calibración absoluta es menos exigente que la relativa. De hecho, una precisión del orden de milisegundos en el tiempo absoluto es suficiente para correlacionar las direcciones reconstruidas de los neutrinos con los eventos astrofísicos transitorios, mientras que se necesita una precisión de $\sim$1 ns en la calibración de tiempo relativa entre fotomultiplicadores para lograr una resolución angular mejor que 0.3° en ANTARES para eventos de tipo trazas con energías superiores a 10 TeV.

Uno de los objetivos del trabajo realizado dentro de esta Tesis ha sido la calibración del tiempo relativo entre los elementos de ANTARES para los últimos dos años (2017 y 2018) del período de toma de datos. Se ha utilizado un método desarrollado recientemente que permite obtener un aumento en el número de eventos bien reconstruidos con respecto al método de calibración empleado anteriormente y combina dos procedimientos de calibración: la calibración con ^{40}K y la calibración con muones atmosféricos, descritas a continuación.

Calibración con ^{40}K. La desintegración radiactiva del ^{40}K presente en el agua de mar se utiliza para estimar los time offsets entre OMs del mismo piso. Si la desintegración β del ^{40}K ocurre a pocos metros de un piso, la luz Cherenkov inducida por el electrón emitido en la desintegración puede iluminar dos OMs del piso en coincidencia. La distribución de las diferencias de tiempo entre señales medidos en coincidencia, es decir, detectados dentro de 50 ns en dos OMs del mismo piso, se caracteriza por un pico gaussiano debido a los fotones producidos en la misma desintegración de ^{40}K, sobre un fondo plano debido a eventos de ^{40}K no correlacionados. Aunque el método ^{40}K solo puede emplearse para la calibración de OMs, presenta dos ventajas principales: no depende de ningún modelo y permite una toma de datos continua.

Calibración con muones atmosféricos. La tasa de muones atmosféricos detectados en ANTARES varía entre 1 y 10 Hz. La calibración con muones atmosféricos consiste en reconstruir la traza de los muones utilizando todos los hits grabados, excepto los detectados por el elemento (OM/piso/línea) que se está calibrando. La diferencia de tiempo entre los hits esperados, obtenidos con la reconstrucción, y los reales se usa para calcular los time offsets entre los elementos a calibrar. La principal ventaja de este método es que se puede utilizar para calibrar todos los elementos del detector, y que no es necesario interrumpir la toma de datos. Por otro lado, requiere una gran estadística (al menos una semana de datos), por lo que es necesario utilizar otro método (con LED y láser) para la recalibración inmediata del detector en caso de sintonización de alto voltaje o conexión de una línea.

El método de calibración desarrollado recientemente combina los dos procedimientos y se divide en tres pasos:

- calibración entre líneas con muones atmosféricos: los time offsets entre líneas se calculan utilizando el método de calibración de muones atmosféricos;
- calibración entre OMs con ^{40}K: los time offsets entre OMs en el mismo piso se obtienen usando el método de calibración con ^{40}K;
- calibración entre storeys con muones atmosféricos: los time offsets entre storeys se obtienen mediante el método de calibración de muones atmosféricos, utilizando como valores iniciales los obtenidos en los dos pasos anteriores.

Los valores de los time offsets se calculan en pasos de un mes. Sin embargo, dado que justo después de una sintonización de alto voltaje o la conexión de una línea, se necesitan nuevas calibraciones, la duración de algunos de los períodos de calibración puede variar de acuerdo con los requisitos actuales. En cada período de calibración, se selecciona una cantidad de datos para que la suma de sus duraciones corresponda a aproximadamente una semana, utilizando los mismos criterios de calidad para la selección de los eventos que en los análisis de física.

Métodos de búsqueda de fuentes de neutrinos astrofísicos puntuales y extendidas

Los datos registrados por un telescopio de neutrinos de alta energía consisten en un conjunto de eventos distribuidos en el cielo, cada uno con una dirección,

energía y tiempo reconstruidos. El reto en astronomía de neutrinos es la identificación de excesos de eventos de fuentes individuales por encima de las fluctuaciones aleatorias del fondo. Para detectar estos eventos de señal, se aplica un método estadístico que se basa en una función de verosimilitud (*likelihood*). La función de verosimilitud describe los datos en términos de funciones de densidad de probabilidad y hace uso de características distintivas que ayudan a separar la señal del fondo.

Se espera que los eventos de señal de una fuente puntual o extendida se acumulen alrededor de la dirección de la fuente con una distribución espacial que depende de la resolución angular del detector. Además, el espectro energético de los neutrinos astrofísicos alcanza energías significativamente más altas que el de los neutrinos atmosféricos. Esto hace que las distribuciones angulares y de energía de los eventos sean características poderosas para distinguir la señal del fondo.

Por esta razón, en las búsquedas de fuentes puntuales y extendidas de neutrinos cósmicos con emisión constante (búsquedas integradas en el tiempo), las funciones de densidad de probabilidad de señal y de fondo se obtienen como producto de un término de espacio y uno de energía. En el caso de búsquedas de fuentes puntuales que emiten un flujo de neutrinos no constante (búsquedas dependientes del tiempo), la información del tiempo de llegada de los neutrinos se convierte en una característica distintiva adicional. Por lo tanto, se incluye un término dependiente del tiempo en la definición de las funciones de densidad de probabilidad de señal y de fondo.

Para probar la presencia de una fuente cósmica de neutrinos en cualquier dirección en el cielo, se calculan los valores de la función de verosimilitud $\mathcal{L}(Datos|H_0)$ y $\mathcal{L}(Datos|H_S)$, para los datos en la dada dirección, para dos hipótesis:

- H_0: los datos consisten únicamente en el fondo;
- H_S: los datos contienen también eventos de neutrinos astrofísicos provenientes de una fuente con algunas características dadas. Los rasgos característicos de la fuente (parámetros del modelo), como el espectro de energía, la extensión espacial, la duración de la emisión de neutrinos, incluidos en la definición de H_S, pueden ser valores fijos en caso de que se asuma un modelo de fuente particular, o pueden ser parámetros libres.

Al maximizar $\mathcal{L}(Datos|H_S)$ con respecto a los parámetros libres, se encuentra la mejor estimación de estos. Mientras el número de eventos de señal detectados

siempre es un parámetro libre en la maximización de la función de verosimilitud, los parámetros específicos del modelo que se dejan libres varían de un análisis a otro.

La significancia estadística de un conjunto de eventos se obtiene calculando el test estadístico, definido como el cociente entre la función de verosimilitud maximizada y la misma función de verosimilitud para el caso de solo fondo, y comparándolo con la distribución de los valores del test estadístico esperado en la hipótesis del solo fondo. Estas distribuciones se calculan mediante la realización de pseudo-experimentos, en los que se simulan muestras similares a la que se debe analizar. La fracción de pseudo-experimentos en los que se ha obtenido un test estadístico mayor que el observado da la significancia del conjunto de eventos . Además, en caso de que se pruebe más de una dirección en el cielo, se aplica una corrección (*trial factor*) a la significancia estadística final, debida a los intentos repetidos.

Para la generación de los eventos de fondo en los pseudo-experimentos, se utiliza la información de declinación, energía y tiempo de los eventos de la muestra de datos reales. La ascensión recta se genera aleatoriamente asumiendo que se distribuye uniformemente. Los eventos de señal se generan de acuerdo con el modelo elegido utilizando funciones de densidad de probabilidad obtenidas mediante simulaciones Monte Carlo.

Con la finalidad de no introducir ningún sesgo, solo se puede acceder al valor real de las coordenadas de los eventos una vez la muestra esté definida con los criterios de selección del análisis (política de *unblinding*). Para cada búsqueda, la muestra final de datos se obtiene realizando varios cortes en parámetros que ayudan a la reducción del número de muones y neutrinos de origen atmosférico. La muestra final se corresponde con la que minimiza el flujo de una fuente necesario para un descubrimiento con una significancia de 5σ en el 50% de los casos.

Resultados de las de búsquedas de fuentes de neutrinos astrofísicos

La búsqueda de fuentes individuales de neutrinos cósmicos es el objetivo principal del trabajo realizado durante esta Tesis. Se han realizado tres análisis diferentes de los datos registrados por los telescopios de neutrinos de alta energía. El primer

análisis es una actualización de la búsqueda de fuentes puntuales estándar de ANTARES utilizando 11 años de datos. El segundo análisis es una búsqueda de fuentes puntuales y extendidas de neutrinos astrofísicos en el cielo Sur (declinaciones negativas) utilizando los datos combinados de ANTARES y IceCube. En el tercer análisis, se ha realizado una búsqueda de correlaciones de tiempo y espacio entre los datos de ANTARES y los candidatos de neutrinos astrofísicos de alta energía detectados por IceCube. Además, un resultado adicional de esta Tesis ha sido la primera estimación de la sensibilidad a las fuentes puntuales de la Fase 1 de KM3NeT/ARCA.

Todos los análisis se basan en el método de máxima verosimilitud, empleado para identificar conjuntos de neutrinos cósmicos de fuentes individuales sobre el fondo atmosférico distribuido aleatoriamente. Los resultados obtenidos se resumen a continuación.

Búsquedas de fuentes puntuales de neutrinos cósmicos con 11 años de datos de ANTARES

Se han realizado varias búsquedas integradas en el tiempo de fuentes puntuales utilizando tanto eventos de tipo traza como eventos de tipo cascada detectados por el telescopio ANTARES durante 11 años de toma de datos. Las búsquedas incluyen una exploración de todo el cielo visible de ANTARES (búsqueda de cielo completo), una investigación de 111 candidatos astrofísicos de fuentes de neutrinos y 75 eventos de tipo traza detectados por IceCube, y un análisis de la dirección del blazar TXS 0506+056. No se ha encontrado evidencia significativa de fuentes cósmicas de neutrinos y se han establecido límites superiores al 90% CL en el flujo de neutrinos.

El conjunto más significativo de la búsqueda de cielo completo se ha encontrado en las coordenadas ecuatoriales $(\alpha, \delta) = (343.7°, 23.6°)$, con una significancia estadística de $23\,\%$ (1.2σ).

De las 111 direcciones de objetos astrofísicos conocidos investigadas, el conjunto más parecido a ser producido por la señal se ha encontrado en la ubicación de la fuente HESSJ0632+057, en las coordenadas ecuatoriales $(\alpha, \delta) = (98.24°, 5.81°)$, con una significancia estadística del 0.15% (1.4σ).

Un total de 75 candidatos de neutrinos detectados por IceCube clasificados como trazas seleccionados desde las muestras HESE y Muon y desde las alertas HESE y EHE se han analizado en una búsqueda separada para tener en cuenta su incertidumbre angular, que no es despreciable. En este caso, la posición en el

cielo de la fuente se dejó como un parámetro adicional en la maximización de la función de verosimilitud. El evento Muon con ID 3 es el candidato de IceCube con el mayor exceso. El conjunto ajustado se encuentra en las coordenadas ecuatoriales $(\alpha, \delta) = (343.7°, 23.6°)$, que está a una distancia de 0.2° de la dirección original del evento $(\alpha, \delta) = (343.55°, 23.78°)$, y coincidente con el conjunto más significativo encontrado en la búsqueda de cielo completo. La significancia estadística es del 1.5% (2.4σ).

Se ha realizado una búsqueda de emisión constante de neutrinos desde la primera fuente cósmica plausible de neutrinos de alta energía, el blazar TXS 0506+056. Se ha obtenido un valor de 1.03 eventos de señal para el mejor ajuste a partir de la maximización en la posición del conjunto, con una significancia estadística del 3.4% (2.1σ).

Búsqueda combinada de fuentes neutrinas puntuales y extendidas en el cielo Sur con los datos de ANTARES y IceCube

En este análisis, se ha explotado la complementariedad de los telescopios ANTARES y IceCube combinando los datos de ambos detectores para buscar fuentes de neutrinos cósmicos en el cielo Sur, mejorando la sensibilidad en comparación con los análisis individuales.

Se han realizado cinco búsquedas diferentes de fuentes puntuales y extendidas de neutrinos utilizando eventos de tipo traza y cascada detectados por ANTARES en nueve años, combinados con siete años de eventos de tipo trazas de IceCube. No se encontraron emisiones significativas de neutrinos ni puntuales ni extendidas y se establecieron límites superiores al 90% CL en el flujo de neutrinos.

Los primeros dos análisis consistieron en la exploración del completo cielo Sur y de una región restringida alrededor del Centro Galáctico. Ambas regiones fueron inspeccionadas buscando fuentes puntuales y fuentes extendidas suponiendo un perfil de emisión gaussiano de varias anchuras (desviación estándar $\sigma_s = 0.5°$, $1.0°$, $2.0°$). El exceso más grande en todo el cielo Sur se encontró en coordenadas ecuatoriales $(\alpha, \delta) = (213.2°, -40.8°)$, para la hipótesis de fuente puntual, con una significancia estadística del 18% (1.3σ). Al limitar la búsqueda a la región del Centro Galáctico, se encontró el exceso más significativo para una extensión de la fuente de $2.0°$, en coordenadas ecuatoriales $(\alpha, \delta) = (274.1°, -40.1°)$, con una significancia estadística del 3% (2.2σ).

En el tercer análisis, se investigaron las direcciónes de una lista predefinida de 57 fuentes de rayos γ conocidas. La fuente candidata más significativa es

HESSJ1023-575 con una significancia estadística del 42% (0.8σ).

Se llevaron a cabo dos búsquedas en la ubicación de dos candidatos prometedores de fuentes de neutrinos, el agujero negro supermasivo Sagittarius A*, y el remanente de supernova *shell-type* RXJ 1713.7-3946. Sagittarius A* se probó como una fuente puntual y como una fuente extendida. El exceso más grande sobre el fondo se observó para una extensión angular de 0.0° con una significancia estadística del 6% (1.9σ). La ubicación de RXJ 1713.7-3946 se investigó asumiendo dos modelos de emisión de neutrinos propuestos y una extensión de fuente de 0.6°. Como no se observó evidencia significativa de neutrinos cósmicos, se derivaron límites superiores.

Los resultados de este análisis combinado han demostrado el gran potencial de la búsqueda conjunta de ANTARES y IceCube de fuentes de neutrinos en el cielo Sur. La combinación de los dos detectores, que difieren en tamaño y ubicación, permite una mejora de hasta un factor $\sim$2 en la sensibilidad en diferentes regiones del cielo Sur, dependiendo del espectro de energía de la fuente.

Búsqueda de correlaciones de tiempo y espacio entre datos de ANTARES y eventos de neutrinos de alta energía de IceCube

En este análisis, los datos registrados por el telescopio ANTARES se escanearon para buscar correlaciones de temporales y espaciales con 54 candidatos de neutrinos astrofísicos de las muestras HESE y Muon de IceCube, para probar un posible origen transitorio de los eventos de IceCube. A diferencia de las búsquedas integradas en el tiempo, la información de los tiempos de llegada de neutrinos fue explotada para mejorar el potencial de descubrimiento. Se asumió un perfil gaussiano para la emisión en el tiempo, dejando la desviación estándar como parámetro de la función de verosimilitud, libre de variar entre 0.1 y 120 días. No se observó ningún exceso significativo sobre el fondo esperado para ninguna de las ubicaciones investigadas y se han derivado límites superiores en la fluencia.

El conjunto más significativo se encontró en la ubicación de la traza de IceCube con ID 15 de la muestra Muon, con una duración de emisión de 120 días y una significancia estadística del 90%. El hecho de que no se han detectado eventos de ANTARES dentro de 0.1 días a partir de los tiempos de observación de los neutrinos de IceCube se ha utilizado para limitar el índice espectral de una posible fuente responsable del evento de IceCube más enérgico de la muestra HESE y de la muestra Muon a un valor respectivamente mas pequeño de -2.3 y -2.4.

Estimación de la sensibilidad futura de la Fase 1 de KM3NeT/ARCA a fuentes puntuales

La estimación de la sensibilidad futura de la Fase 1 de KM3NeT/ARCA se ha obtenido utilizando simulaciones Monte Carlo de neutrinos cósmicos y de neutrinos y muones atmosféricos reconstruidos como eventos de trazas. Los resultados muestran que las 24 líneas de KM3NeT/ARCA mejorarán los resultados actual de ANTARES, correspondientes a 11 años de funcionamiento, después de solo dos años de toma de datos.

Bibliography

[1] M. Spurio, *Particles and Astrophysics: A Multi-Messenger Approach*. Springer, 2015.

[2] **Particle Data Group** Collaboration, C. Patrignani *et al.*, "Review of Particle Physics," *Chin. Phys.* **C40** no. 10, (2016) 100001.

[3] V. L. Ginzburg and V. S. Ptuskin, "On the origin of cosmic rays: Some problems in high-energy astrophysics," *Rev. Mod. Phys.* **48** (1976) 161. [Erratum Rev. Mod. Phys. 48, 675 (1976)].

[4] E. Fermi, "On the Origin of the Cosmic Radiation," *Phys. Rev.* **75** (1949) 1169.

[5] E. Fermi, "Galactic Magnetic Fields and the Origin of Cosmic Radiation," *Astrophys. J.* **119** (1954) 1.

[6] V. L. Ginzburg, Y. M. Khazan, and V. S. Ptuskin, "Origin of cosmic rays: Galactic models with halo," *Astrophysics and Space Science* **68** no. 2, (1980) 295.

[7] T. K. Gaisser, R. Engel, and E. Resconi, *Cosmic Rays and Particle Physics*. Cambridge University Press, 2016.

[8] V. Ptuskin, "Propagation of galactic cosmic rays," *Astropart. Phys.* **39-40** (2012) 44–51.

[9] J. R. Hoerandel, "Models of the knee in the energy spectrum of cosmic rays," *Astropart. Phys.* **21** (2004) 241–265.

[10] J. R. Horandel, "Overview on direct and indirect measurements of cosmic rays - Some thoughts on Galactic cosmic rays and the knee," *Int. J. Mod. Phys.* **A20** (2005) 6753–6764.

[11] J. R. Horandel, N. N. Kalmykov, and A. V. Timokhin, "Propagation of super high-energy cosmic rays in the Galaxy," *Astropart. Phys.* **27** (2007) 119–126.

[12] J. Blumer, R. Engel, and J. R. Horandel, "Cosmic Rays from the Knee to the Highest Energies," *Prog. Part. Nucl. Phys.* **63** (2009) 293–338.

[13] T. Wibig and A. W. Wolfendale, "At what particle energy do extragalactic cosmic rays start to predominate?," *J. Phys.* **G31** (2005) 255–264.

[14] A. M. Hillas, "The Origin of Ultrahigh-Energy Cosmic Rays," *Ann. Rev. Astron. Astrophys.* **22** (1984) 425–444.

[15] K. Greisen, "End to the cosmic ray spectrum?," *Phys. Rev. Lett.* **16** (1966) 748–750.

[16] G. T. Zatsepin and V. A. Kuzmin, "Upper limit of the spectrum of cosmic rays," *JETP Lett.* **4** (1966) 78–80.

[17] H. Athar, M. Jezabek, and O. Yasuda, "Effects of neutrino mixing on high-energy cosmic neutrino flux," *Phys. Rev.* **D62** (2000) 103007.

[18] L. Nellen, K. Mannheim, and P. L. Biermann, "Neutrino production through hadronic cascades in AGN accretion disks," *Phys. Rev.* **D47** (1993) 5270–5274.

[19] A. Kappes, J. Hinton, C. Stegmann, and F. A. Aharonian, "Potential Neutrino Signals from Galactic Gamma-Ray Sources," *Astrophys. J.* **656** (2007) 870–896. [Erratum: Astrophys. J.661,1348(2007)].

[20] T. K. Gaisser, F. Halzen, and T. Stanev, "Particle astrophysics with high-energy neutrinos," *Phys. Rept.* **258** (1995) 173. [Erratum: Phys. Rept.271,355(1996)].

[21] F. Halzen and D. Hooper, "High-energy neutrino astronomy: The Cosmic ray connection," *Rept. Prog. Phys.* **65** (2002) 1025.

[22] J. K. Becker, "High-energy neutrinos in the context of multimessenger physics," *Phys. Rept.* **458** (2008) 173.

[23] S. R. Kelner and F. A. Aharonian, "Energy spectra of gamma-rays, electrons and neutrinos produced at interactions of relativistic protons with low energy radiation," *Phys. Rev.* **D78** (2008) 034013.

[24] K. Murase, "On the Origin of High-Energy Cosmic Neutrinos," *AIP Conf. Proc.* **1666** (2015) 040006.

[25] M. Ahlers and F. Halzen, "High-energy cosmic neutrino puzzle: a review," *Rept. Prog. Phys.* **78** no. 12, (2015) 126901.

[26] G. Morlino, E. Amato, and P. Blasi, "Gamma ray emission from SNR RX J1713.7-3946 and the origin of galactic cosmic rays," *Mon. Not. Roy. Astron. Soc.* **392** (2009) 240–250.

[27] F. Vissani, "Neutrinos from galactic sources of cosmic rays with known γ-ray spectra," *Astropart. Phys.* **26** (2006) 310–313.

[28] **H.E.S.S.** Collaboration, A. Abramowski *et al.*, "Acceleration of petaelectronvolt protons in the Galactic Centre," *Nature* **531** (2016) 476.

[29] T. Piran, "Gamma-ray bursts and the fireball model," *Phys. Rept.* **314** (1999) 575–667.

[30] **MAGIC** Collaboration, V. A. Acciari *et al.*, "Teraelectronvolt emission from the γ-ray burst GRB 190114C," *Nature* **575** no. 7783, (2019) 455–458.

[31] **H.E.S.S.** Collaboration, H. Abdalla *et al.*, "A very-high-energy component deep in the γ-ray burst afterglow," *Nature* **575** no. 7783, (2019) 464–467.

[32] **H.E.S.S.** Collaboration, "GRB190829A: Detection of VHE gamma-ray emission with H.E.S.S.,". http://www.astronomerstelegram.org/?read=13052.

[33] S. E. Woosley and J. S. Bloom, "The Supernova Gamma-Ray Burst Connection," *Ann. Rev. Astron. Astrophys.* **44** (2006) 507–556.

[34] **LIGO Scientific, Virgo** Collaboration, B. P. Abbott *et al.*, "GW170817: Observation of Gravitational Waves from a Binary Neutron Star Inspiral," *Phys. Rev. Lett.* **119** no. 16, (2017) 161101.

[35] **ANTARES** Collaboration, S. Adrian-Martinez *et al.*, "Search for muon neutrinos from gamma-ray bursts with the ANTARES neutrino telescope using 2008 to 2011 data," *Astron. Astrophys.* **559** (2013) A9.

[36] **ANTARES** Collaboration, A. Albert *et al.*, "Search for high-energy neutrinos from bright GRBs with ANTARES," *Mon. Not. Roy. Astron. Soc.* **469** (2017) 906.

[37] **IceCube** Collaboration, M. G. Aartsen *et al.*, "An All-Sky Search for Three Flavors of Neutrinos from Gamma-Ray Bursts with the IceCube Neutrino Observatory," *Astrophys. J.* **824** no. 2, (2016) 115.

[38] **IceCube** Collaboration, M. G. Aartsen *et al.*, "Extending the search for muon neutrinos coincident with gamma-ray bursts in IceCube data," *Astrophys. J.* **843** no. 2, (2017) 112.

[39] **IceCube** Collaboration, P. Coppin and N. van Eijndhoven, "IceCube search for high-energy neutrinos produced in the precursor stages of gamma-ray bursts," 2019. arXiv:1908.06653 [astro-ph.HE].

[40] B. Zhang, *The Physics of Gamma-Ray Bursts*. Cambridge University Press, 2018.

[41] P. Kumar and B. Zhang, "The physics of gamma-ray bursts & relativistic jets," *Phys. Rept.* **561** (2014) 1–109.

[42] C. M. Urry and P. Padovani, "Unified schemes for radio-loud active galactic nuclei," *Publ. Astron. Soc. Pac.* **107** (1995) 803.

[43] M. Boettcher, A. Reimer, K. Sweeney, and A. Prakash, "Leptonic and Hadronic Modeling of Fermi-Detected Blazars," *Astrophys. J.* **768** (2013) 54.

[44] **IceCube** Collaboration, M. G. Aartsen *et al.*, "Neutrino emission from the direction of the blazar TXS 0506+056 prior to the IceCube-170922A alert," *Science* **361** no. 6398, (2018) 147–151.

[45] **IceCube, Fermi-LAT, MAGIC, AGILE, ASAS-SN, HAWC, H.E.S.S., INTEGRAL, Kanata, Kiso, Kapteyn, Liverpool Telescope, Subaru, Swift NuSTAR, VERITAS, VLA/17B-403** Collaboration, M. G. Aartsen *et al.*, "Multimessenger observations of a flaring blazar coincident with high-energy neutrino IceCube-170922A," *Science* **361** no. 6398, (2018) eaat1378.

[46] **IceCube** Collaboration, M. G. Aartsen *et al.*, "Observation of High-Energy Astrophysical Neutrinos in Three Years of IceCube Data," *Phys. Rev. Lett.* **113** (2014) 101101.

[47] **IceCube** Collaboration, C. Kopper, W. Giang, and N. Kurahashi, "Observation of Astrophysical Neutrinos in Four Years of IceCube Data," *PoS* **ICRC2015** (2016) 1081.

[48] **IceCube** Collaboration, C. Kopper, "Observation of Astrophysical Neutrinos in Six Years of IceCube Data," *PoS* **ICRC2017** (2018) 981.

[49] **IceCube** Collaboration, A. Schneider, "Characterization of the Astrophysical Diffuse Neutrino Flux with IceCube High-Energy Starting Events," arXiv:1907.11266 [astro-ph.HE].

[50] **IceCube** Collaboration, M. G. Aartsen *et al.*, "Observation and Characterization of a Cosmic Muon Neutrino Flux from the Northern Hemisphere using six years of IceCube data," *Astrophys. J.* **833** no. 1, (2016) 3.

[51] **IceCube** Collaboration, C. Haack and C. Wiebusch, "A measurement of the diffuse astrophysical muon neutrino flux using eight years of IceCube data," *PoS* **ICRC2017** (2017) 1005.

[52] **IceCube** Collaboration, J. Stettner, "Measurement of the Diffuse Astrophysical Muon-Neutrino Spectrum with Ten Years of IceCube Data," arXiv:1908.09551 [astro-ph.HE].

[53] **IceCube** Collaboration, H. M. Niederhausen and Y. Xu, "High Energy Astrophysical Neutrino Flux Measurement Using Neutrino-induced Cascades Observed in 4 Years of IceCube Data," *PoS* **ICRC2017** (2018) 968.

[54] A. Palladino, M. Spurio, and F. Vissani, "On the IceCube spectral anomaly," *JCAP* **1612** no. 12, (2016) 045.

[55] **ANTARES** Collaboration, A. Albert *et al.*, "New constraints on all flavor Galactic diffuse neutrino emission with the ANTARES telescope," *Phys. Rev.* **D96** no. 6, (2017) 062001.

[56] **ANTARES, IceCube** Collaboration, A. Albert *et al.*, "Joint Constraints on Galactic Diffuse Neutrino Emission from the ANTARES and IceCube Neutrino Telescopes," *Astrophys. J.* **868** no. 2, (2018) L20.

[57] Y. Sui and P. S. Bhupal Dev, "A Combined Astrophysical and Dark Matter Interpretation of the IceCube HESE and Throughgoing Muon Events," *JCAP* **1807** no. 07, (2018) 020.

[58] C. Mascaretti and F. Vissani, "On the relevance of prompt neutrinos for the interpretation of the IceCube signals," *JCAP* **1908** no. 08, (2019) 004.

[59] **IceCube** Collaboration, "GCN/AMON NOTICE 50579430_130033," (2017) . https://gcn.gsfc.nasa.gov/notices_amon/50579430_130033.amon.

[60] **IceCube** Collaboration, "GCN circular 21916," (2017) . https://gcn.gsfc.nasa.gov/gcn3/21916.gcn3.

[61] **ANTARES** Collaboration, A. Albert *et al.*, "The Search for Neutrinos from TXS 0506+056 with the ANTARES Telescope," *Astrophys. J.* **863** no. 2, (2018) L30.

[62] **IceCube** Collaboration, M. G. Aartsen *et al.*, "The contribution of Fermi-2LAC blazars to the diffuse TeV-PeV neutrino flux," *Astrophys. J.* **835** no. 1, (2017) 45.

[63] A. Keivani *et al.*, "A Multimessenger Picture of the Flaring Blazar TXS 0506+056: implications for High-Energy Neutrino Emission and Cosmic Ray Acceleration," *Astrophys. J.* **864** no. 1, (2018) 84.

[64] M. Cerruti, A. Zech, C. Boisson, G. Emery, S. Inoue, and J. P. Lenain, "Leptohadronic single-zone models for the electromagnetic and neutrino emission of TXS 0506+056," *Mon. Not. Roy. Astron. Soc.* **483** no. 1, (2019) L12–L16.

[65] W. Winter, S. Gao, X. Rodrigues, A. Fedynitch, A. Palladino, and M. Pohl, "Multi-messenger interpretation of the neutrinos from TXS 0506+056," arXiv:1909.06289 [astro-ph.HE].

[66] X. Rodrigues, S. Gao, A. Fedynitch, A. Palladino, and W. Winter, "Leptohadronic Blazar Models Applied to the 2014–2015 Flare of TXS 0506+056," *Astrophys. J.* **874** no. 2, (2019) L29.

[67] M. A. Markov, "On high energy neutrino physics," in *Proceedings, 10th International Conference on High-Energy Physics (ICHEP 60): Rochester, NY, USA, 25 Aug - 1 Sep 1960*, pp. 578–581. 1960. http://inspirehep.net/record/1341439/files/C60-08-25-p578.pdf.

[68] S. L. Glashow, "Resonant scattering of antineutrinos," *Phys. Rev.* **118** (1960) 316–317.

[69] **CTEQ** Collaboration, H. L. Lai, J. Huston, S. Kuhlmann, J. Morfin, F. I. Olness, J. F. Owens, J. Pumplin, and W. K. Tung, "Global QCD analysis of

parton structure of the nucleon: CTEQ5 parton distributions," *Eur. Phys. J.* **C12** (2000) 375–392.

[70] A. Gazizov and M. P. Kowalski, "ANIS: High energy neutrino generator for neutrino telescopes," *Comput. Phys. Commun.* **172** (2005) 203–213.

[71] A. Sánchez-Losa, *Search for high energy cosmic muon neutrinos from variable gamma-ray sources and time calibration of the optical modules of the ANTARES telescope*. PhD thesis, Universitat de València, Valencia, Spain, 2015. http://roderic.uv.es/handle/10550/47138.

[72] T. Chiarusi and M. Spurio, "High-Energy Astrophysics with Neutrino Telescopes," *Eur. Phys. J.* **C65** (2010) 649–701.

[73] **Particle Data Group** Collaboration, M. Tanabashi *et al.*, "Review of Particle Physics," *Phys. Rev.* **D98** no. 3, (2018) 030001.

[74] P. A. Cerenkov, "Visible radiation produced by electrons moving in a medium with velocities exceeding that of light," *Phys. Rev.* **52** (1937) 378–379.

[75] C. Bogazzi, *Search for cosmic neutrinos with ANTARES*. PhD thesis, Leiden U., 2014. http://inspirehep.net/record/1297320/files/Thesis-2014-Bogazzi.pdf.

[76] A. Roberts, "The Birth of high-energy neutrino astronomy: A Personal history of the DUMAND project," *Rev. Mod. Phys.* **64** (1992) 259–312.

[77] G. V. Domogatsky *et al.*, "Progress report on Lake Baikal neutrino experiment: Site studies and stationary string," in *11th International Conference on Neutrino Physics and Astrophysics (Neutrino 84) Dortmund, Germany, June 11-16, 1984*, pp. 550–555. 1985.

[78] E. Andres *et al.*, "The AMANDA neutrino telescope: Principle of operation and first results," *Astropart. Phys.* **13** (2000) 1–20.

[79] A. D. Avrorin *et al.*, "Status and recent results of the BAIKAL-GVD project," *Phys. Part. Nucl.* **46** no. 2, (2015) 211–221.

[80] **IceCube** Collaboration, A. Achterberg *et al.*, "First Year Performance of The IceCube Neutrino Telescope," *Astropart. Phys.* **26** (2006) 155–173.

[81] **ANTARES** Collaboration, M. Ageron *et al.*, "ANTARES: the first undersea neutrino telescope," *NIMPA* **656** (2011) 11–38.

[82] **NEMO** Collaboration, P. Piattelli, "The Neutrino Mediterranean Observatory project," *Nucl. Phys. Proc. Suppl.* **143** (2005) 359–362.

[83] **NESTOR** Collaboration, G. Aggouras *et al.*, "A measurement of the cosmic-ray muon flux with a module of the NESTOR neutrino telescope," *Astropart. Phys.* **23** (2005) 377–392.

[84] **KM3NeT** Collaboration, S. Adrian-Martinez *et al.*, "Letter of intent for KM3NeT 2.0" *J. Phys.* **G43** no. 8, (2016) 084001.

[85] **ANTARES** Collaboration, J. A. Aguilar *et al.*, "The data acquisition system for the ANTARES Neutrino Telescope," *Nucl. Instrum. Meth.* **A570** (2007) 107–116.

[86] **ANTARES** Collaboration, J. A. Aguilar *et al.*, "Transmission of light in deep sea water at the site of the ANTARES Neutrino Telescope," *Astropart. Phys.* **23** (2005) 131–155.

[87] C. Bigongiari and S. Mangano and J. Ruiz Rivas and others, "Results of the optical properties of sea water in the Antares site with the Optical Beacon system." ANTARES internal note, 2013. ANTARES-PHYS/2013-015.

[88] **ANTARES** Collaboration, P. Amram *et al.*, "Sedimentation and fouling of optical surfaces at the antares site," *Astropart. Phys.* **19** (2003) 253–267.

[89] C. Tamburini, ANTARES Collaboration, *et al.*, "Deep-sea bioluminescence blooms after dense water formation at the ocean surface," *PLOS ONE* **8** no. 7, (07, 2013) 1–10.

[90] J. B. Martí, *Search for cosmic sources in neutrino telescopes and time calibration in the ANTARES neutrino telescope*. PhD thesis, Universitat de València, Valencia, Spain, 2018. http://roderic.uv.es/handle/10550/66597.

[91] M. de Jong, "The antares trigger software." ANTARES internal note, 2005. ANTARES-Soft/2005-005.

[92] E. Wisser, *Neutrinos from the Milky Way*. PhD thesis, University of Leiden, 2015. https://www.nikhef.nl/pub/services/biblio/theses_pdf/thesis_EL_Visser.pdf.

[93] J. Carr, S. Escoffier, and D. Zaborov, "Proposition for an alternative trigger based on the t3 cluster trigger." ANTARES internal note, 2007. ANTARES-Soft/2007-016.

[94] **ANTARES** Collaboration, S. Adrian-Martinez *et al.*, "The Positioning System of the ANTARES Neutrino Telescope," *JINST* **7** (2012) T08002.

[95] **KM3NeT** Collaboration, A. Margiotta, "The KM3NeT deep-sea neutrino telescope," *Nucl. Instrum. Meth.* **A766** (2014) 83–87.

[96] **IceCube** Collaboration, M. G. Aartsen *et al.*, "The IceCube Neutrino Observatory: Instrumentation and Online Systems," *JINST* **12** no. 03, (2017) P03012.

[97] **IceCube** Collaboration, R. Abbasi *et al.*, "IceTop: The surface component of IceCube," *Nucl. Instrum. Meth.* **A700** (2013) 188–220.

[98] M. Ackermann *et al.*, "Optical properties of deep glacial ice at the South Pole," *J. Geophys. Res. Atmos.* **111** no. D13, (2006) D13203.

[99] **IceCube** Collaboration, M. G. Aartsen *et al.*, "Measurement of South Pole ice transparency with the IceCube LED calibration system," *Nucl. Instrum. Meth.* **A711** (2013) 73–89.

[100] **ANTARES** Collaboration, A. Margiotta, "Common simulation tools for large volume neutrino detectors," *Nucl. Instrum. Meth.* **A725** (2013) 98–101.

[101] D. Bailey, *Monte Carlo tools and analysis methods for understanding the ANTARES experiment and predicting its sensitivity to Dark Matter*. PhD thesis, Wolfson College, Oxford, 2002. http://inspirehep.net/record/581319.

[102] J. Pumplin, D. R. Stump, J. Huston, H. L. Lai, P. M. Nadolsky, and W. K. Tung, "New generation of parton distributions with uncertainties from global QCD analysis," *JHEP* **07** (2002) 012.

[103] J. Brunner, "Updated tag list for the new antares event format." ANTARES internal note, 1999. ANTARES-Soft/1993-003.

[104] V. Agrawal, T. K. Gaisser, P. Lipari, and T. Stanev, "Atmospheric neutrino flux above 1-GeV," *Phys. Rev.* **D53** (1996) 1314–1323.

[105] M. Honda, T. Kajita, K. Kasahara, S. Midorikawa, and T. Sanuki, "Calculation of atmospheric neutrino flux using the interaction model calibrated with atmospheric muon data," *Phys. Rev.* **D75** (2007) 043006.

[106] R. Enberg, M. H. Reno, and I. Sarcevic, "Prompt neutrino fluxes from atmospheric charm," *Phys. Rev.* **D78** (2008) 043005.

[107] J. N. Bahcall and E. Waxman, "High-energy astrophysical neutrinos: The Upper bound is robust," *Phys. Rev.* **D64** (2001) 023002.

[108] D. Heck, J. Knapp, J. Capdevielle, G. Schatz, and T. Thouw, "Corsika: A monte carlo code to simulate extensive air showers," in *Forschungszentrum Karlsruhe Report*. 1998. http://inspirehep.net/record/469835/files/FZKA6019.pdf.

[109] G. Carminati, A. Margiotta, and M. Spurio, "Atmospheric MUons from PArametric formulas: A Fast GEnerator for neutrino telescopes (MUPAGE)," *Comput. Phys. Commun.* **179** (2008) 915–923.

[110] P. Antonioli, C. Ghetti, E. V. Korolkova, V. A. Kudryavtsev, and G. Sartorelli, "A Three-dimensional code for muon propagation through the rock: Music," *Astropart. Phys.* **7** (1997) 357–368.

[111] S. Navas and L. Thompson, "Km3 user guide and reference manual." ANTARES internal note, 1999. ANTARES-Soft/1999-011.

[112] CERN, *GEANT program manual*. CERN program library long writeup W5013, 1993.

[113] M. de Jong, "The TriggerEfficiency program." ANTARES internal note, 2009. ANTARES-Soft/2009-001.

[114] R. Bormuth, "Description of the two standard trigger algorithms in the JPP software package (release r2356 to trunk at 27-11-2015)." KM3NeT Internal Note, 2015. KM3NeT_SOFT_2015_001.

[115] A. J. Heijboer, *Track Reconstruction and Point Source Searches with ANTARES*. PhD thesis, NIKHEF, Amsterdam, 2004. http://www.nikhef.nl/pub/services/newbiblio/theses.php.

[116] T. Michael, *Light at the End of the Shower*. PhD thesis, NIKHEF, 2016. http://www.nikhef.nl/pub/services/newbiblio/theses.php.

[117] **ANTARES** Collaboration, A. Albert *et al.*, "An algorithm for the reconstruction of neutrino-induced showers in the ANTARES neutrino telescope," *Astron. J.* **154** no. 6, (2017) 275.

[118] F. Folger, *Search for a diffuse cosmic neutrino flux using shower events in the ANTARES neutrino telescope*. PhD thesis, ECAP, 2014. https://opus4.kobv.de/opus4-fau/frontdoor/index/index/docId/5107.

[119] F. Folger, "The dusj shower reconstruction project." ANTARES internal note, 2013. ANTARES-PHYS-2013-003.

[120] **ANTARES** Collaboration, A. Albert *et al.*, "An algorithm for the reconstruction of high-energy neutrino-induced particle showers and its application to the ANTARES neutrino telescope," *Eur. Phys. J.* **C77** no. 6, (2017) 419.

[121] **KM3NeT** Collaboration, K. Melis, M. de Jong, and A. Heijboer, "KM3NeT/ARCA Event Reconstruction Algorithms," *PoS* **ICRC2017** (2017) 950.

[122] **ANTARES** Collaboration, S. Adrian-Martinez *et al.*, "Measurement of the atmospheric ν_μ energy spectrum from 100 GeV to 200 TeV with the ANTARES telescope," *Eur. Phys. J.* **C73** no. 10, (2013) 2606.

[123] **ANTARES** Collaboration, F. Schüssler, "Energy reconstruction in neutrino telescopes," in *Proceedings, 33rd International Cosmic Ray Conference (ICRC2013): Rio de Janeiro, Brazil, July 2-9, 2013*, p. 0421. http://inspirehep.net/record/1413014.

[124] **ANTARES** Collaboration, J. A. Aguilar *et al.*, "Study of Large Hemispherical Photomultiplier Tubes for the ANTARES Neutrino Telescope ," *Nucl.Instrum.Meth.* **A555** (2005) 132–141.

[125] **ANTARES** Collaboration, J. A. Aguilar *et al.*, "Time Calibration of the ANTARES Neutrino Telescope," *Astropart. Phys.* **34** (2011) 539–549.

[126] **ANTARES** Collaboration, M. Ageron *et al.*, "The ANTARES Optical Beacon System," *Nucl. Instrum. Meth.* **A578** (2007) 498–509.

[127] D. Zaborov, "The k-40 calibration method." ANTARES internal note, 2011. ANTARES-CALI-2011-001.

[128] I. Salvadori, "K40 calibration." ANTARES internal note, 2016. ANTARES-CALI-2016-001.

[129] O. Behnke, K. Kröninger, T. Schörner-Sadenius, and G. Schott, *Data Analysis in High Energy Physics: A Practical Guide to Statistical Methods*. Wiley-VCH, 2013.

[130] R. J. Barlow, "Extended maximum likelihood," *Nucl. Instrum. Meth.* **A297** (1990) 496–506.

[131] **ANTARES** Collaboration, S. Adrian-Martinez *et al.*, "Search for Cosmic Neutrino Point Sources with Four Year Data of the ANTARES Telescope," *Astrophys. J.* **760** (2012) 53.

[132] J. Neyman, "Outline of a Theory of Statistical Estimation Based on the Classical Theory of Probability," *Phil. Trans. Roy. Soc. Lond.* **A236** no. 767, (1937) 333–380.

[133] S. S. Wilks, "The Large-Sample Distribution of the Likelihood Ratio for Testing Composite Hypotheses," *Annals Math. Statist.* **9** no. 1, (1938) 60–62.

[134] **ANTARES** Collaboration, A. Albert *et al.*, "First all-flavor neutrino pointlike source search with the ANTARES neutrino telescope," *Phys. Rev.* **D96** no. 8, (2017) 082001.

[135] **ANTARES** Collaboration, J. Aublin, G. Illuminati, and S. Navas, "Searches for point-like sources of cosmic neutrinos with 11 years of ANTARES data," 2019. arXiv:1908.08248 [astro-ph.HE].

[136] "The TeVcat catalog,". http://tevcat.uchicago.edu.

[137] **IceCube** Collaboration, "AMON ICECUBE_HESE Event Information,". https://gcn.gsfc.nasa.gov/amon_hese_events.html.

[138] **IceCube** Collaboration, "AMON ICECUBE_EHE Event Information,". https://gcn.gsfc.nasa.gov/amon_ehe_events.html.

[139] M. W. E. Smith *et al.*, "The Astrophysical Multimessenger Observatory Network (AMON)," *Astropart. Phys.* **45** (2013) 56–70.

[140] H. A. Ayala Solares *et al.*, "The Astrophysical Multimessenger Observatory Network (AMON): Performance and science program," *Astropart. Phys.* **114** (2020) 68–76.

[141] **ANTARES** Collaboration, J. A. Aguilar *et al.*, "Performance of the front-end electronics of the ANTARES neutrino telescope," *Nucl. Instrum. Meth.* **A622** (2010) 59.

[142] **ANTARES, IceCube** Collaboration, A. Albert *et al.*, "ANTARES and IceCube Combined Search for Neutrino Point-like and Extended Sources in the Southern Sky," arXiv:2001.04412 [astro-ph.HE].

[143] **IceCube** Collaboration, M. G. Aartsen *et al.*, "All-sky Search for Time-integrated Neutrino Emission from Astrophysical Sources with 7 yr of IceCube Data," *Astrophys. J.* **835** no. 2, (2017) 151.

[144] **H.E.S.S.** Collaboration, F. Aharonian, "Detection of extended very-high-energy gamma-ray emission towards the young stellar cluster Westerlund 2," *Astron. Astrophys.* **467** (2007) 1075–1080.

[145] **KM3NeT** Collaboration, A. Trovato *et al.*, "Expectations for detection of neutrinos from point-like sources with KM3NeT/ARCA," *PoS* **ICRC2017** (2017) 999.

[146] F. L. Villante and F. Vissani, "How precisely neutrino emission from supernova remnants can be constrained by gamma ray observations?," *Phys. Rev.* **D78** (2008) 103007.

[147] F. Vissani and F. L. Villante, "Cosmic rays and neutrinos from supernova remnants (or: the time when H.E.S.S. met Ginzburg and Syrovatskii)," *Nucl. Instrum. Meth.* **A588** (2008) 123–129.

[148] **H.E.S.S.** Collaboration, H. Abdalla *et al.*, "H.E.S.S. observations of RX J1713.7-3946 with improved angular and spectral resolution: Evidence for gamma-ray emission extending beyond the X-ray emitting shell," *Astron. Astrophys.* **612** (2018) A6.

[149] Y. Bai, A. J. Barger, V. Barger, R. Lu, A. D. Peterson, and J. Salvado, "Neutrino Lighthouse at Sagittarius A*," *Phys. Rev.* **D90** no. 6, (2014) 063012.

[150] **ANTARES** Collaboration, A. Albert *et al.*, "ANTARES neutrino search for time and space correlations with IceCube high-energy neutrino events," *Astrophys. J.* **879** no. 2, (2019) 108.

[151] **IceCube** Collaboration, M. G. Aartsen *et al.*, "The IceCube Realtime Alert System," *APh* **92** (2017) 30–41.